UNIVERSITY OF CALABRIA

DEPARTMENT OF PHYSICS

DOCTORAL THESIS

Soft matter for active plasmonics and applications

Author:
Giovanna PALERMO

Supervisor:
Prof. Cesare Paolo UMETON

School Director:
Prof. Roberto BARTOLINO

A thesis submitted in fulfilment of the requirements
for the degree of Doctor of Philosophy in

Science and technology of mesophases and molecular materials

Academic year 2014/15

Contents

List of Figures

Abbreviations

AFM	Atomic Force Microscopy
AR	Aspect Ratio
BP	Blue Phase
CLC	Cholesteric Liquid Crystal
CTAB	CetylTrimethylAmmonium Bromide
DNA	Deoxyribo Nucleic Acid
GNPs	Gold Nanoparticles
GNRs	Gold Nanorods
ITO	Indium Tin Oxide
LSPR	Localized Surface Plasmon Resonance
LC	Liquid Crystal
LCD	Liquid Crystal Display
LP	Longitudinal Polarization
MNP	Metallic NanoParticle
NLC	Nematic Liquid Crystal
NIL	Nano Imprinting Lithography
NIR	Near InfraRed
NP	Nanoparticle
NLC	Nematic Liquid Crystal
PAL	Potho Alignement Layer
PE	PolyElectrolyte
POM	Polarized optical Microscope
PSS	Poly(Sodium 4-Styrenesulfonate)
SEM	Scanning Electron Microscopy
TP	Transversal Polarization

To my family

Introduction

Nano-Optics is a subfield of Optics which describes the behavior of light at the nanoscale. The recent experimental exploration of nano-optics profoundly impacts modern society. Thanks to the maturation of various technologies including lasers, nano fabrication, electron beam microscopy, near field optical microscopy, colloidal chemistry and so on, nano-optics has provided a new class of novel photonic structures, including quantum dots, used as nanosources of light, nano diamonds, which permit mapping of local magnetic fields and density of states, high Q-factor resonators, which can serve as ultra sensitive detectors, surface plasmon waveguides, which can allow for ultra compact planar optical circuitry, nano-antennas, which are used to harvest and radiate light efficiently, gold nano particles, which can allow for novel cancer treatment techniques, and many more. Traditional optical elements, such as lenses or mirror present a limit, related to the localization of the field set by the Abbe diffraction limit, which could *a priori* prevent using optics at the nanometer scale. One way to confine light at the nanoscale is to couple the radiation with materials characterized by high dielectric permittivity. Among these materials, a particular interest has been devoted to metallic nanostructures; in this case, the interaction of electromagnetic wave with conduction electrons of the metal leads for a specific wavelength to a coherent collective electron oscillation, known as Localized Surface Plasmon Resonance (LSPR). This phenomenon enables to strongly confine and enhance the electric field at the surface of the metal on a scale much shorter than the wavelength of the impinging light. In the far field, such resonant excitation results in both a strong absorption and a scattering of light. The study of these phenomena and their applications is goal of Plasmonics. The frequency of the plasmonic resonance strongly depends on particle size, shape and dielectric function of the surrounding medium and an active control of the LSPR of nanoparticles represents a crucial step toward the realization of nanodevices with this aim, many approaches have been studied, which

include optical, magnetic, thermal and mechanical methodologies. In this thesis, the possibility to control the LSPR by exploiting the properties of a particular class of soft materials as Liquid Crystals (LCs) is discussed, which can be easily modified by using electrical, magnetic, thermal and mechanical stimuli. For this reason, the peculiar properties of liquid crystals foster new possibilities in plasmonics: The combination of the intrinsic tunability of soft matter with the plasmonic properties of metal nanostructures provides novel and intriguing features of systems, commonly referred to active plasmonics characteristics.

The thesis is organized as follow:

- Chapter 1 deals with the physics behind the LSPR. The major differences between massive (bulk) and nanostructured gold are showed. The interaction of metals with electromagnetic wave is described by using the Drude model. However, this model presents limitations when applied at the nanoscale; for this reason the Mie and the quasi-static approximation result to be more suitable for the plasmonic studies.

- Chapter 2 focuses on the physics of soft matter in order to give a quick background of concepts used in the next chapters. Two examples of applications are reported: the first one shows that Cholesteric Liquid Crystal can be exploited as key-element in a pressure sensitive device; in the second one, the recent advances in the LC alignment for display applications are reported.

- In chapter 3 Plasmonics meets soft matter. A preliminary study on systems made of gold nanospheres and gold nanorods immobilized on a substrate and layered with Nematic LC is presented.

- Chapter 4 shows that it is possible to use a particular kind of LC, the DNA, to transfer organization to GNRs, by exploiting a self-assembly process.

- Chapter 5 deals with the physics of plasmonic heating. First the energy conversion from electromagnetic wave to heat is investigated; then, the dynamics of photo-induced heating is discussed. Finally, an experimental-theoretical approach to investigate the heat generated from a huge number of random distributed gold nanoparticles is presented.

- In chapter 6 and 7, it is described how LCs can be used to detect the temperature variation around nanoparticle by exploiting in one case the birifrengence of Nematic LC and in the second case the tunability of the selective reflection band of Cholesteric LC.

- In chapter 8 a survey on the possible application of the heat generated by the nanoparticles in the treatment of cancer disease is reported.

Chapter 1

Introduction to the Optical Properties of Gold Nanoparticles

1.1 Introduction

In this chapter the most important phenomena that form the basis for a study of *surface plasmon resonance* are summarized. In the first part, a brief review of the major difference between massive (bulk) and nano-structured gold is presented, followed by a description of Drude model, which describes the optical response of metals. The limit of this model is presented for the case of nano-objects like gold nanoparticles. The chapter closes with the theoretical description of the Localized Plasmon Resonance by means of two exhaustive approaches: quasi-static approximation and Mie theory.

1.2 Differences between massive (bulk) and nanostructured gold

Gold possesses a unique combination of physical and chemical properties at both the macroscopic and the microscopic scales. At the macroscopic scale, gold is known for its unique yellow colour, for its chemical stability and high redox potential. The chemistry of gold $(5d^{10}6s^{1})$ is determined by the easy activation of the $5d$ electrons and its propension to acquire a further electron to complete the $6s^2$ level (and not to lose the one it has [7, 8]). The optical absorption

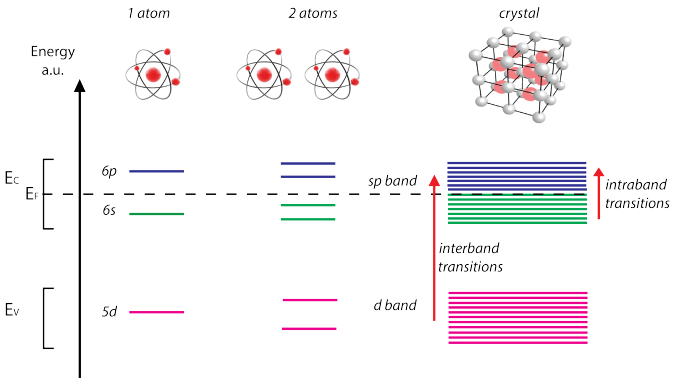

FIGURE 1.1: Sketch of the electronic structure of gold: for a single atom, the electronic levels are discrete, as shown above. For a gold dimer Au–Au, the levels tend to split. For a crystal, this lifting of degeneracy widens and forms a continuum of levels: the d band emerges from the d electrons of all the gold atoms and is completely filled with electrons. The conduction band is formed from the 6s and 6p orbitals and is partially filled (conduction band).With this structure, light can excite two kinds of transitions: intraband transitions and interband transitions.

of gold in the visible region of the spectrum is due to the relativistic lowering of the gap between the centre of the $5d$ band and the Fermi level (see Fig. 1.1). A good indication of this relativistic effect is the very low value of the interband transition energy for gold if compared to silver. The interband threshold represents the energy required to excite electrons from the top of the $5d$ band into the $6sp$ conduction band. In the case of gold, its value is $1.84\,eV$, which means that red light is able to excite this transition. In the case of silver, the interband transition is in the UV range so that the visible light is almost not affected after reflecting on a silver surface [9]. Gold crystallises in the face-centred cubic (fcc) structure; the bond between atoms is a metallic one, with electrons free to move throughout the crystal structure; the nuclei can be considered as fixed and surrounded by a sort of ”fluid” of free electrons. This model explains some properties of the metal, as its high electrical and thermal conductivity; in fact, since these electrons are not linked to any particular atom, they are highly mobile [10].

When the size of the gold sample is progressively decreased, significant changes in physical properties and chemical reactivity are observed; they become especially noticeable when the size falls below about 100 nm. Such particles, often named *nanoparticles* (NPs), present a high the surface/volume ratio, which is responsible for some changes in the structural character. In fact, changes in the electronic structure affect the optical response of NPs and the metallic behaviour of them [11]. Among the remarkable properties of gold nanoparticles (GNPs), the collective behaviour of their conduction electrons, which gives rise to the plasmon resonance, is a dramatic one.

1.3 Electromagnetism of metals

For a long time the most know properties of metals were the high electrical and thermal conductivity. After three years from Thompson's discovery of the electron, scientists became more interested in studying the mechanisms of interaction between metals and electromagnetic fields. Around 1900, Paul Drude, a German physicist, used new concepts to postulate a classical model that well explained several phenomena related to the interaction between radiation and metals. This model links optical and electric properties of a metal through the behavior of electrons. The assumptions of Drude's model are:

- Metals are made of heavy, static, positively charged ions immersed in a cloud of light, negatively charged, easily mobile electrons; they form an *electron gas* that follows the Maxwell-Boltzmann statistics;
- The electron-electron interactions can be neglected.
- The only considered interaction are the electron-ion collisions.

By following the kinetic theory of gases, electrons in the gas move in straight lines and make collisions only with the ion cores. The probability for an electron to make a collision in a short time dt is dt/τ, where τ is the mean time between collisions, called *relaxation time*. This quantity, which is typically of the order of 10^{-14} s at room temperature, is related to an other important quantity, $\gamma = 1/\tau$ that represents the collision frequency and have, thus, values of the order of $100\,THz$.

Drude's model successfully determined the form of Ohm's law in terms of free electrons and the relation between electrical and thermal conduction [12], but failed to explain electron heat capacity and the magnetic susceptibility of conduction electrons. Failures of the model are the result of the limitations of the classical model (and Maxwell-Boltzmann statistics in particular) [13].

In fact, in microscopic physics, it is common to express Ohm's law in terms of conductivity that is intrinsic to the substance that the wire is made of. In this framework, Ohm's law writes as:

$$\mathbf{J} = \sigma \mathbf{E} \tag{1.1}$$

where $\mathbf{E}$ represents the Electric Field, $\mathbf{J}$ the Current Density, and σ the conductivity of the material. We consider a wire of cross sectional area A, where an electrical current flows, which consists of N electrons per volume unit, all moving in the same direction with velocity v. The number of electrons flowing through the area A in time dt is given by $dN = NAvdt$, while the charge crossing A in dt is $dQ = -edN = -NevAdt$, so that $\mathbf{J} = -Ne\mathbf{v}$. In the absence of electric fields, electrons move randomly inside the conductor due to their thermal energy, but when an electric field is applied, electrons are affected by the force $\mathbf{F} = -e\mathbf{E}$ that pushes them to move all in the same direction, with an average speed that is given by:

$$\mathbf{v} = -\frac{e\tau}{m}\mathbf{E} \tag{1.2}$$

Thus, substituting in $\mathbf{J} = -Ne\mathbf{v}$, relation (1.2) yields

$$\mathbf{J} = -\frac{Ne^2\tau}{m}\mathbf{E} \tag{1.3}$$

Comparison with (1.1) gives the DC-Drude conductivity:

$$\sigma_0 = -\frac{Ne^2\tau}{m} \tag{1.4}$$

The Drude model can also predict a current as a response to an oscillating electric field with angular frequency ω. This can be achieved by considering that the equation of motion for an electron of the electron gas subjected to an external electric field $\mathbf{E}$, is obtained by solving the equation:

$$m\ddot{\mathbf{x}} + m\gamma\dot{\mathbf{x}} = -e\mathbf{E} \tag{1.5}$$

where m is the effective mass, and γ is the already mentioned collision frequency that produces the damping. This expression can be rewritten as:

$$\dot{\mathbf{p}} = -\frac{\mathbf{p}}{\tau} - e\mathbf{E} \tag{1.6}$$

where $\mathbf{p} = m\dot{\mathbf{x}}$ is the momentum of an individual free electron. If $\mathbf{E}$ assumes the form $\mathbf{E} = \mathbf{E}_0 e^{-i\omega t}$, we consider as a solution of (1.6) the expression: $\mathbf{p}(t) = \mathbf{p}_0 e^{-i\omega t}$; by substituing we

obtain:

$$-i\omega \mathbf{p}_0 = -\frac{\mathbf{p}_0}{\tau} - e\mathbf{E_0} \tag{1.7}$$

$$\mathbf{J} = -\frac{Ne\mathbf{p}}{m} = \frac{\sigma_0}{1-i\omega\tau}\mathbf{E} = \sigma(\omega)\mathbf{E} \tag{1.8}$$

Thus the AC-Drude conductivity is given by:

$$\sigma(\omega) = \frac{\sigma_0}{1-i\omega\tau} \tag{1.9}$$

A useful application of the Drude model is the description of the propagation of electromagnetic waves in metals by considering a complex dielectric function $\varepsilon(\omega)$ that shows the dispersive properties of the substance. In order to derive the expression of $\varepsilon(\omega)$ we consider the expression

$$m\ddot{\mathbf{x}} + m\gamma\dot{\mathbf{x}} = -e\mathbf{E} \tag{1.10}$$

that takes into account the oscillations of the free electron gas induced by the electric field $\mathbf{E}(t)$. A solution of (1.5) is given by $\mathbf{x}(t) = \mathbf{x}_0 e^{-i\omega t}$ which, replaced in (1.5), yields:

$$\mathbf{x}(t) = \frac{e}{m(\omega^2 + i\gamma\omega)}\mathbf{E}(t). \tag{1.11}$$

The electric displacement $\mathbf{D}$ and the macroscopic polarization $\mathbf{P}$ are given by:

$$\mathbf{D} = \varepsilon_0\mathbf{E} + \mathbf{P} = \varepsilon_0\varepsilon\mathbf{E} \tag{1.12}$$

$$\mathbf{P} = -Ne\mathbf{x} \tag{1.13}$$

respectively, where N is the number of electrons per unit volum. Thus,

$$\mathbf{D} = \varepsilon_0\mathbf{E} - \frac{Ne^2}{m(\omega^2 + i\gamma\omega)}\mathbf{E} \tag{1.14}$$

and

$$\varepsilon(\omega) = 1 - \frac{\omega_p^2}{\omega^2 + i\gamma\omega} \tag{1.15}$$

that represents the dielectric function in the Drude model, where ω_p is the plasma frequency of the free electron gas and is defined by:

$$\omega_p = \left(\frac{Ne^2}{\varepsilon_0 m}\right)^{1/2} \tag{1.16}$$

From (1.15) it can be easily derived that the real and imaginary components of this complex dielectric function, written as $\varepsilon(\omega) = \varepsilon_1(\omega) + \varepsilon_2(\omega)$, are given by:

$$\varepsilon_1(\omega) = 1 - \frac{\omega_p^2 \tau^2}{1 + \omega^2 \tau^2} \tag{1.17}$$

$$\varepsilon_2(\omega) = \frac{\omega_p^2 \tau}{\omega(1 + \omega^2 \tau^2)} \tag{1.18}$$

The complex dielectric function $\varepsilon(\omega)$ is related to the complex refractive index of the medium $\tilde{n} = n(\omega) + i\kappa(\omega)$ through the relation: $\tilde{n} = \sqrt{\varepsilon_r}$. Explicitly this yields:

$$\varepsilon_1 = n^2 - \kappa^2 \tag{1.19}$$

$$\varepsilon_2 = 2n\kappa \tag{1.20}$$

$$n^2 = \frac{\varepsilon_1}{2} + \frac{1}{2}\sqrt{\varepsilon_1^2 + \varepsilon_2^2} \tag{1.21}$$

$$\kappa = \frac{\varepsilon_2}{2n} \tag{1.22}$$

κ is called *extinction coefficient* and determines the absorption of optical electromagnetic waves propagating through the medium; it is linked to the absorption coefficient α of Beer's law, which describes the exponential attenuation of a beam intensity $I(x)$ propagating through the medium via $I(x) = I_0 e^{-\alpha x}$. Indeed, since $E \propto \exp(i\frac{\omega}{c}\tilde{n}x)$ and then $I \propto E^2 \propto \exp(2i\frac{\omega}{c}(n + i\kappa)x)$ we have:

$$\alpha(\omega) = \frac{2\kappa(\omega)\omega}{c} \tag{1.23}$$

Relations (1.17) and (1.18) enable to study the electromagnetic response of metals (related to the plasma frequency ω_p) by distinguishing the three cases $\omega > \omega_p$, $\omega < \omega_p$, $\omega = \omega_p$).

► In the case $\omega > \omega_p$, $\tilde{n}$ is positive because $\varepsilon(\omega)$ is real and positive, $\varepsilon(\omega) \to 1$, this implies that the electromagnetic wave propagates through the metal that appears transparent. For noble metals, it is necessary to take into account that the response of the material in this region is

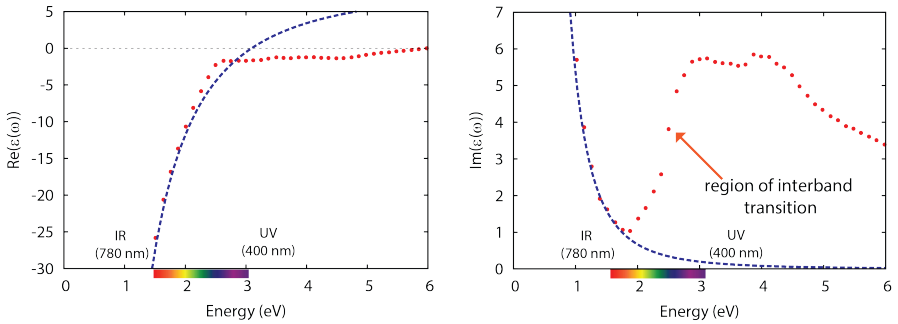

FIGURE 1.2: Real and imaginary components of the dielectric function for a free electron gas (dash) fitted to experimental data of the dielectric function of gold (dot).

dominated by free s electrons, since the filled d band close to the Fermi surface causes a highly polarized environment [14]. This contribution to the polarization related to the ion cores can be considered by adding the term $\mathbf{P}_\infty = \varepsilon_0(\varepsilon_\infty - 1)\mathbf{E}$ to (1.12). This effect is therefore described by a dielectric constant ε_∞ (usually $1 \leq \varepsilon_\infty \leq 10$), and we can write:

$$\varepsilon(\omega) = \varepsilon_\infty - \frac{\omega_p^2}{\omega^2 + i\gamma\omega} \tag{1.24}$$

The validity limits of the free-electron description (1.24) are illustrated, for the case of gold, in Figure (1.2). It shows the real and imaginary components ε_1 and ε_2 of the dielectric function of a free electron gas, fitted with experimental data of the dielectric function of gold [15].

In the visible frequency range the applicability of the free-electron model clearly breaks down, due to the occurrence of interband transitions, leading to an increase in ε_2.

▶ For frequencies $\omega < \omega_p$, we distinguish two subcase: $\omega\tau \gg 1$ and $\omega\tau \ll 1$.
In the case $\omega\tau \gg 1$, we are in the condition of frequency very close to ω_p and, as we have seen at the beginning of this discussion, metals totally reflect the electromagnetic waves; in this range the real and imaginary parts of the dielectric function become:

$$\varepsilon_1(\omega) = 1 - \frac{\omega_p^2}{\omega^2} \tag{1.25}$$

$$\varepsilon_2(\omega) \approx 0 \tag{1.26}$$

respectively. As we can see from these equations the permittivity is real, which implies that there is no absorption; metals retain their metallic character, of *perfect conductor*. This behavior is common among different metals but not for noble metals, in which the response is again affected

by the interband transitions.

In the case $\omega\tau \ll 1$, we are in the condition of frequency very far from ω_p and the real and imaginary parts of the dielectric function become:

$$\varepsilon_1(\omega) = 1 - \omega_p^2\tau^2 \tag{1.27}$$

$$\varepsilon_2(\omega) \approx \frac{\omega_p^2}{\omega} \tag{1.28}$$

respectively. In this case, $\varepsilon_2 \gg \varepsilon_1$, and the real and imaginary parts of the refractive index have a comparable magnitude:

$$n \approx \kappa = \sqrt{\frac{\varepsilon_2}{2}} = \sqrt{\frac{\tau\omega_p^2}{2\omega}} \tag{1.29}$$

In this region, metals are mainly absorbing, with an absorption coefficient given by

$$\alpha(\omega) = \frac{2\kappa(\omega)\omega}{c} = \left(\frac{2\omega_p^2\tau\omega}{c^2}\right)^{1/2}. \tag{1.30}$$

Remembering the DC-Drude conductivity (1.4) and the expression for the plasma frequency ω_p the expression of σ becames $\sigma_0 = \omega_p^2\tau\varepsilon_0$ and then

$$\alpha = \sqrt{2\sigma_0\omega\mu_0} \tag{1.31}$$

This coefficient is closely related to the skin depth, which represents the depth of penetration of the wave in the metal:

$$\delta = \frac{2}{\alpha} = \frac{c}{\kappa\omega} = \sqrt{\frac{2}{\sigma_0\omega\mu_0}} \tag{1.32}$$

► In order to complete the study of the response of metals to an electromagnetic field, it is necessary to consider the particular case $\omega = \omega_p$. To understand what happens in this case, it is necessary to introduce the fundamental relation that links conductivity and dielectric function in the Fourier domain. The relation can be derived by starting from Maxwell's equations (details of calculations in [14]) and writes:

$$\varepsilon(\mathbf{K},\omega) = 1 + \frac{i\sigma(\mathbf{K},\omega)}{\varepsilon_0\omega} \tag{1.33}$$

We consider the traveling-wave solution of Maxwell's equations in the absence of external stimuli. Combining the curl equations:

$$\nabla \times \mathbf{E} = -\frac{\partial \mathbf{B}}{\partial t} \tag{1.34}$$

$$\nabla \times \mathbf{H} = \mathbf{J}_{\mathbf{ext}} + \frac{\partial \mathbf{D}}{\partial t} \tag{1.35}$$

leads to the *wave equation*, that in the Fourier domain becomes:

$$\mathbf{K}(\mathbf{K}\cdot\mathbf{E}) - K^2\mathbf{E} = -\varepsilon(\mathbf{K},\omega)\frac{\omega^2}{c^2}\mathbf{E} \tag{1.36}$$

where $c = \frac{1}{\sqrt{\varepsilon_0\mu_0}}$ is the speed of light in vacuum. Looking at this equation, two cases have to be distinguished: the case of transverse waves, $\mathbf{K}\cdot\mathbf{E} = 0$, yielding the generic dispersion relation:

$$K^2 = \varepsilon(\mathbf{K},\omega)\frac{\omega^2}{c^2} \tag{1.37}$$

where $\varepsilon(\mathbf{K},\omega)$ is given by equation (1.33), and the case of longitudinal waves, for which (1.36) implies that

$$\varepsilon(\mathbf{K},\omega) = 0 \tag{1.38}$$

indicating that longitudinal collective oscillations can only occur at frequencies corresponding to zeros of $\varepsilon(\omega)$. The meaning of this oscillation can be elucidated by considering the dispersion relation of traveling wave obtained by using equation (1.25) in (1.37):

$$\omega^2 = \omega_p^2 + K^2c^2 \tag{1.39}$$

Figure 1.3 shows the plot of the dispersion relation for the traveling wave given by equation (1.39): there is clearly no propagation of electro-magnetic waves below the plasmon frequency ($\omega < \omega_p$), while for $\omega > \omega_p$ waves propagate with a group velocity $v_g = \frac{d\omega}{dK} < c$; the special case $\omega = \omega_p$ can be interpreted in the following way. In the small damping limit $\mathbf{K} = 0$ and $\varepsilon(\omega_p) = 0$; this implies that $\mathbf{D} = 0$ and the electric field becames a pure depolarization field ($\mathbf{E} = \frac{-\mathbf{P}}{\varepsilon_0}$). This leads to a collective longitudinal oscillation of the conduction electron gas with respect to the fixed background of positive ion cores in a plasma slab. A collective displacement u of the electron cloud leads to a surface charge density $\sigma = \pm Neu$ at the slab boundaries

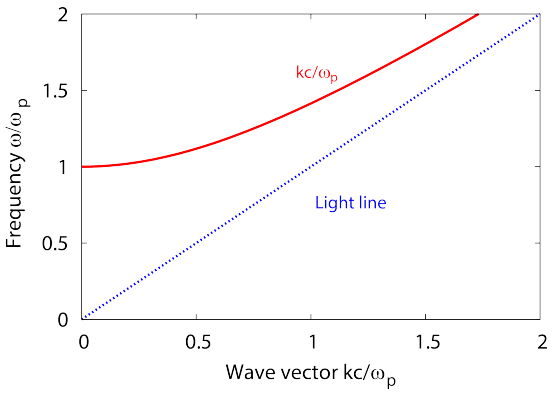

FIGURE 1.3: Dispersion relation of free electron gas.

and yields a homogeneous electric field $\mathbf{E} = \frac{Neu}{\varepsilon_0}$ inside the slab. Thus, the displaced electrons experience a restoring force, and their movement can be described by the equation of motion $Nm\ddot{u} = -Ne\mathbf{E}$. Inserting the expression for the electric field leads to

$$Nm\ddot{u} = -\frac{N^2e^2u}{\varepsilon_0} \tag{1.40}$$

$$\ddot{u} + \omega_p^2 u = 0 \tag{1.41}$$

Thus, the plasma frequency ω_p represents the natural frequency of a free oscillation of the electron sea and the quanta of these charge oscillations are called ***Plasmons or Volume Plasmons*** (VP). Due to the longitudinal nature of the excitation, VP do not couple to transverse electromagnetic waves, and can only be excited by particle impacts.

The Drude model is a good start for describing the dielectric functions of metals. However when a precise model is needed, the Drude model is by far too simplified because it only takes into account the free electrons (intraband transitions) and completely dismisses the contribution from the bound electrons (interband transitions). The latter play an important role for gold. This is illustrated in Fig. 1.2 where the complex dielectric function is plotted. The accurate measurement of this function is crucial for reasonably modelling the optical response of AuNP. One of the preferred measurements was performed by Johnson and Christy in 1972 [15].

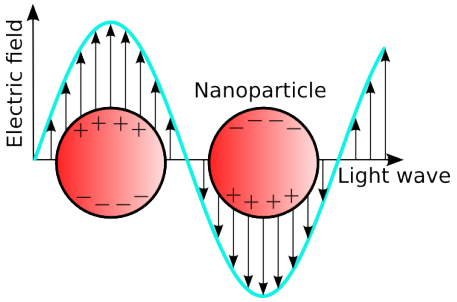

FIGURE 1.4: Sketch of the mechanism of the Surface Plasmon Resonance in a spherical gold nanoparticle.

1.4 Localized surface plasmon resonance in nanoparticles, LSPR

If particles have sizes much smaller than the wavelength of light and smaller than the penetration depth δ of the field (i.e. particle size around $20\,nm$), the electron cloud of the particle is entirely probed by the electric field. The whole assembly of electrons is polarized, and this creates surface charges that accumulate alternately on opposite ends of the particle (Fig. 1.4).

This oscillating polarization of the particles creates an electric field opposed to the excitation field and results in a restoring force. This oscillation is partially damped. The damping occurs through two channels: creation of heat and light scattering. All this can be described as a dipolar oscillator characterized by a resonance frequency called Localized Surface Plasmon Resonance (LSPR). This denomination is generally accepted although this localized plasmon oscillation is not primarily a surface effect, but a bulk effect taking place in the very small and confined volume of metallic nano-objects. The main properties of LSPR can be understood within the dipolar model and can be summarized as follows:

- The plasmon resonance appears in the uv, visible or near-infrared range of the spectrum for gold or silver nanoparticles. A light beam going through an assembly of homogeneous nanoparticles is partially absorbed at the plasmon resonance frequency so that the emerging beam displays a spectrum with a sharp absorption at ω_p. At the same time, the nanoparticles exhibit light scattering with a cross section much larger than a conventional dye [16].

- The LSPR strongly depends on the environment close to the particle surface.

- When excited at the resonance, the dipole radiates a near-field electromagnetic wave, whose amplitude can be enhanced by a factor up to 10. This plasmon amplification is widely used for enhancing the sensitivity of biosensors.

1.5 Theoretical Description of the Localized Plasmon Resonance

When a light beam impinges on a particle, the optical electric field puts into oscillation the electrical charges of matter (conduction electrons and protons). As a consequence, there is an absorption of part of the impinging radiation and an emission of a secondary radiation, a phenomenon known as scattering. In order to describe both effects, it is necessary to write down the expressions of electromagnetic fields $\mathbf{E},\mathbf{H}$ starting from Maxwell's equations. The most famous exact solution of Maxwell's equations, for the case of small particles with arbitrary radius and refractive index, has been obtained in the framework of the Mie theory [17, 18], developed by Gustav Mie in 1908 with the aim of explaining the different colors exhibited, in absorption and scattering processes, by small colloidal particles of gold suspended in water. In a linear, isotropic, homogeneous and non-radiative medium in which small particles are present, an incident plane wave, that is constituted by electric and magnetic fields $(\mathbf{E},\mathbf{H})$, has to satisfy the following wave equation:

$$\nabla^2\mathbf{E}+n^2k^2\mathbf{E}=0 \tag{1.42}$$

$$\nabla^2\mathbf{H}+n^2k^2\mathbf{H}=0 \tag{1.43}$$

where k is the wave vector and n is the refractive index. If we define the vector $\mathbf{M}=\nabla\times(\mathbf{r}\psi)$, where ψ is an arbitrary scalar function and r the position vector, that in our case indicates the radial coordinate, it is possible to show that this satisfies the equation:

$$\nabla^2\mathbf{M}+n^2k^2\mathbf{M}=\nabla\times(\nabla^2\psi+n^2k^2\psi) \tag{1.44}$$

in this case $\mathbf{M}$ satisfies the vectorial wave equation when ψ satisfies the scalar wave equation $(\nabla^2\psi+n^2k^2\psi)$. The vector $\mathbf{N}$, that is possible to define as $nk\mathbf{N}=\nabla\times\mathbf{M}$, has the same

properties. By solving the scalar wave equation with the appropriate boundary conditions, it is therefore possible to obtain two fields which satisfy the vectorial wave equations. In particular, calling u and v two independent solutions of the equation that gives rise to scalar fields $\mathbf{M}_u$, $\mathbf{N}_u$, $\mathbf{M}_v$, $\mathbf{N}_v$, one can identify the electric and magnetic fields by:

$$\mathbf{E} = \mathbf{M}_v + i\mathbf{N}_u \tag{1.45}$$

$$\mathbf{H} = m(-\mathbf{M}_u + i\mathbf{N}_v) \tag{1.46}$$

For a system that has spherical symmetry, it is possible to solve the problem in spherical coordinates. Exploiting the fact that the spherical waves constitute a complete and orthonormal set of functions, and any other function can be developed as a sum of spherical waves, the basic idea of the Mie theory is to rewrite the incident plane wave as a superposition of spherical waves (through a series expansion) inside and outside the sphere and impose boundary conditions on the surface to obtain the coefficients of the development. In particular, we can write that inside the sphere:

$$u = e^{i\omega t} cos\phi \sum_{n=1}^{\infty} -a_n(-i)^n \frac{2n+1}{n(n+1)} P_n^l(cos\theta) j_n(kr) \tag{1.47}$$

$$v = e^{i\omega t} sin\phi \sum_{n=1}^{\infty} -b_n(-i)^n \frac{2n+1}{n(n+1)} P_n^l(cos\theta) j_n(kr) \tag{1.48}$$

where P_n^l are the associated Legendre functions and j_n are the spherical Bessel functions of the first kind. In spherical coordinates the wave equation is factored and has solutions of the type:

$$\psi_{n,l} = cosl\phi P_n^l(cos\theta) z_n(mkr) \tag{1.49}$$

$$\psi_{n,l} = sinl\phi P_n^l(cos\theta) z_n(mkr) \tag{1.50}$$

where n and l are integer numbers, z_n are the spherical Bessel function.

By imposing the boundary conditions on the surface of the sphere and introducing the parameter $x = \frac{2\pi a}{\lambda}$ we obtain the scattering coefficients:

$$a_n = \frac{\psi_n'(mx)\psi_n(x) - m\psi_n(mx)\psi_n'(x)}{\psi_n'(mx)\varsigma_n(x) - m\psi_n(mx)\varsigma_n'(x)} \tag{1.51}$$

$$b_n = \frac{m\psi_n'(mx)\psi_n(x) - m\psi_n(mx)\psi_n'(x)}{m\psi_n'(mx)\varsigma_n(x) - m\psi_n(mx)\varsigma_n'(x)} \tag{1.52}$$

where ψ and ς are the Riccati-Bessel functions. The scattering cross section is related to a_n and b_n by the relation:

$$\sigma = \frac{2\pi}{k^2}\sum_{n=1}^{\infty}(\mid a_n \mid^2 + \mid b_n \mid^2) \tag{1.53}$$

For small particles ($< 60\,nm$), it is sufficient to restrain the multipole expansion to its first term, that correspond to a dipolar case. This is indicated as "dipolar approximation", also called the quasi-static or Rayleigh limit [19].

1.5.1 Optical response in the quasi-static approximation

As mentioned in the previous section, for small NPs ($D << \lambda$, where D is the diameter of the NP and λ is the wavelength of the impinging light), the optical response can be calculated by means of a simplified model using the *quasistatic approximation*. In this way is possible to derive simple analytical expressions for the response of spherical nanoparticles, easily generalized to the case of ellipsoids. If we consider a single metal NP, characterized by a dielectric function $\varepsilon(\omega) = \varepsilon_1(\omega) + i\varepsilon_2(\omega)$ surrounded by a medium characterized by a dielectric permittivity ε_m, which is acted on by an electric field $\mathbf{E}$, two different scenarios may occur: 1) If $(D \sim \lambda)$ the spatial variation of the electric field inside the NP induces a very complex surface charge distribution resulting in a multipolar configurations. 2) If $(D << \lambda)$ the field inside the sphere can be considered uniform and the charge distribution on the surface creates a singol dipole (dipole approximation)(Fig. 1.5); the same applies in the time domain: the propagation time inside the sphere nD/c becomes a much smaller than the oscillation period of the field $2\pi/\omega$.

In this case, the complexity of the problem is reduced (by leaving out the time dependence of the applied field) to a simple effect of polarization of a sphere in a uniform field, which is resolved by using the Poisson equation, with appropriate boundary conditions.

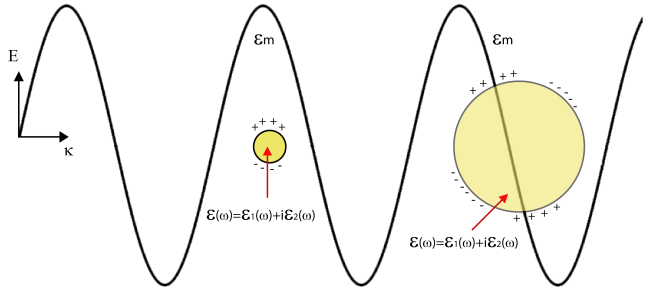

FIGURE 1.5: Sketch of the two possible cases of interaction of light with NP: for $(D << \lambda)$ the field inside the sphere can be considered uniform and the charge distribution on the surface create a singol dipole, if $(D \sim \lambda)$ multipolar configuration occurs.

In general, the interaction of the electromagnetic wave with a single sphere can be treated by considering a local field E_L that takes into account the influence of all the polarizing entities [20]:

$$E_L = E + \frac{P_s}{3\varepsilon_0\varepsilon_m} \tag{1.54}$$

with:

$$P_s = \frac{p}{V_{np}}\mathbf{p_s} \tag{1.55}$$

where $\mathbf{p_s}$ is the dipole momentum of a single sphere, P_s is the polarization of the other spheres in the system, V_{np} is the volume of the NPs, p is the volumetric ratio that takes into account the number N_{np} of NPs in the system. For small volumes, E_L can be approximate to E. It is possible to demonstrate that the field E_i inside the sphere can be related to the incident field E by the relation:

$$\vec{E_i} = \frac{3\varepsilon_m}{\varepsilon(\omega) + 2\varepsilon_m}\vec{E} = f(\omega)\vec{E} \tag{1.56}$$

Outside the sphere, the field created by the charges accumulated in the sphere is equivalent to the one created by a dipole located in the centre of the sphere, characterized by a momentum:

$$\mathbf{p_s} = 3V\varepsilon_0\varepsilon_m\frac{\varepsilon-\varepsilon_m}{\varepsilon+2\varepsilon_m}\vec{E} = 3\varepsilon_0\alpha\vec{E} \tag{1.57}$$

where V is the volume of the sphere and α its polarizability. The optical response of the NP is equivalent to the one of a dipole placed into its center. The resonance occurs when the condition $\varepsilon(\omega)+2\varepsilon_m = 0$ is verified; in this case, an enhancement of the internal electric field E_i is obtained (*dielectric confinement*).

By starting from the the induced field, is possible to calculate the scattering cross section of the NP [17]:

$$\sigma_s = \frac{24\pi^3}{\lambda^4} \mid \alpha \mid^2 = \frac{24\pi^3V^2\varepsilon_m^2}{\lambda^4}\left|\frac{\varepsilon-\varepsilon_m}{\varepsilon+2\varepsilon_m}\right|^2 \tag{1.58}$$

that is proportional to the volume square and to $1/\lambda^4$ (Rayleigh scattering). By the real and imaginary part of the dielectric function of the metal, it is possible to calculate the absorption cross section [17] as:

$$\sigma_{abs} = \frac{6\pi}{\lambda}Im(\alpha) = \frac{18\pi V\varepsilon_m^{3/2}}{\lambda}\frac{\varepsilon_2}{|\varepsilon+2\varepsilon_m|^2} \tag{1.59}$$

that is proportional to the volume of the nanosphere. For a metal NP characterized by a diameter D, in a homogeneous medium, the ratio between the scattering and absorption cross sections is proportional to the sphere volume, normalized by a factor λ^3:

$$\sigma_s/\sigma_{abs} \propto (D/\lambda)^3 \tag{1.60}$$

in the quasi-static approximation $(D << \lambda)$, the scattering is negligible compared to the absorption; this implies that, for small NPs the extinction cross section is related only to the absorption one:

$$\sigma_s \ll \sigma_{abs} \approx \sigma_{ext} \tag{1.61}$$

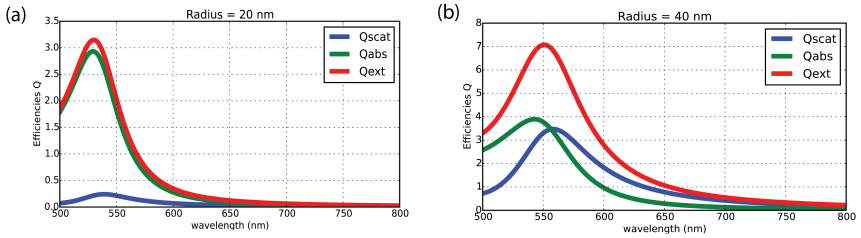

FIGURE 1.6: Extinction, scattering and absorption cross sections of a NP with radius equal to 20 nm (a) and 40 nm(b).

As mentioned in the beginning of this section, this model is valid only for small NPs. By increasing the size of the NPs the scattering becames predominant with respect to the absorption (Fig. 1.6).

1.6 Conclusions

In this chapter, a short survey of the optical properties of metal nano-objects has been reported by focalizing the attention on the LSPR. The validity of Drude's model to describe the electrical and optical response of gold has been illustrated, along with the description of its limit in the visible frequency region, due to the occurence of interband transitions. The Mie theory and the quasi-static approximation have been introduced to describe the optical response of gold nanoparticles. Many of the concepts discussed in this chapter will be used later in this thesis.

Chapter 2

Physics and applications of soft matter

2.1 Introduction

This chapter presents a short survey of the different liquid crystal (LC) phases. Main attention is paid to thermotropic liquid crystals, which show rich polymorphism upon variation of temperature, electric fields, magnetic fields, pressure or a content of various compounds in a mixture. These characteristics have been largely exploited in the past for optoelectronics devices, sensors and LC displays. Only in recent years the property of LCs to modulate the refractive index by means of external stimuli has been related to the possibility to control the plasmonic properties of gold nano-structures *(see chapter 6 and 7)*.

2.2 Structure and main properties of Liquid Crystals

LCs have found an important place in modern life. It is possible to find them in our laptoop displays, clocks, telephones, TV screens, photo-cameras, etc. Other applications include slide projection systems, spatial light modulators, temperature sensors and even liquid crystal lasers. In all these technical fields LCs occupy a key position. This is because they consume just appreciable amounts of energy when they change their state under external influences such as temperature variations, electric field, mechanical stress or whatever. In addition, there are very important biological aspects of LCs. In fact, proteins, lipids, cells membranes, virus, nucleic acid

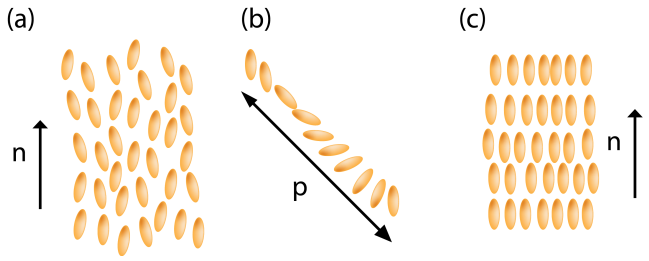

FIGURE 2.1: Sketch of the structure of nematic (a), cholesteric (b) and smectic (c) liquid crystals.

(*see chapter 4*) posses a high percentage of liquid crystalline compounds. The liquid-crystalline phase possesses many of the mechanical properties of liquids, e.g., high fluidity, formation and coalescence of droplets; at the same time, it is similar to crystals in that it exhibit anisotropy in its optical, mechanical, electrical, and magnetic properties. The anisotropy of LCs is related to the presence of a long-range orientational order in the arrangement of constituent molecules, and sometimes to one - or two - dimensional quasi long-range translational or positional order. By changing the LC molecule orientation, it is possible to change optical and mechanical properties of the medium. It is possible to classify LCs in accordance with the physical parameters controlling the existence of the liquid crystalline phase. There are two distinct types of liquid crystals: lyotropic and thermotropic. These materials exhibit liquid crystalline properties as a function of different physical parameters and environments.

- Lyotropic LCs are obtained when an appropriate concentration of a given material is dissolved in a suitable solvent. The most common systems are those formed by water and amphiphilic molecules (molecules that possess a hydrophilic part that interacts strongly with water and a hydrophobic part that is water insoluble) such as soaps, detergents, and lipids. In this case the variable controlling the existence of the liquid crystalline phase is the amount of solvent (or concentration).

- Thermotropic LCs exhibit various liquid crystalline phases as a function of temperature. Although their molecular structures are, in general, quite complicated, they are often represented as *rigid rods*. These rigid rods interact with one another and form distinctive ordered structures. There are three main classes of thermotropic liquid crystals: nematic, cholesteric, and smectic (Fig. 2.1). There are several subclassifications of smectic liquid crystals in accordance with the positional and directional arrangements of the molecules.

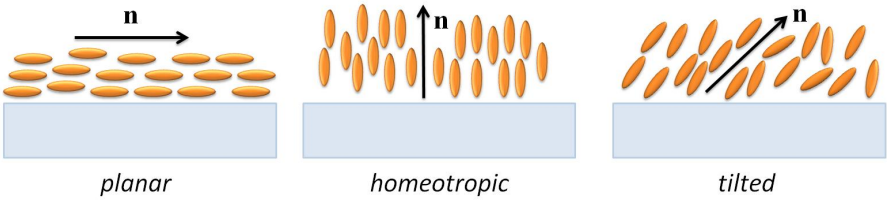

FIGURE 2.2: Types of liquid crystals alignment near the surface: planar, homeotropic and tilted.

The key parameter in the study of LCs is the director **n** that represents the average direction of the molecular long axes in the LC phase; in most LCs both directions of the vector **n**, $+\mathbf{n}$ and $-\mathbf{n}$ are equivalent. The uniaxial symmetry around the director in the LC phase leads to an anisotropy in many physical properties. For example, the refractive index, the dielectric permittivity, the magnetic susceptibility, viscosity and conductivity have a different value, depending on the reciprocal orientation between the external field and the LC director [21, 22].

2.3 Surface Anchoring

In general, the Nematic LC (NLC) alignment originates from a symmetry breaking at the surface of the functionalized glasses that form the cell containing the LC. All kinds of surface cause a different orientation of the molecular director **n** close to it: the alignment present at the surface propagates in the material over macroscopic distances, due to the elastic properties of LCs. There are three main configuration for **n** nearby the surface of the substrate: planar, homeotropic and tilted (Figure 2.2).

The surface in contact with the NLC is usually considered flat at the microscale, and the orientation of **n** close to it is determined by the polar (θ) and azimuthal (φ) angles (Figure 2.2),where θ is the angle between **n** and the plane of the surface, while φ is the angle between the projection of **n** on the plane of the surface and the *easy axis* (red arrow in Figure 2.3), which represents the direction induced by the alignment treatment of the surface.

The pre-tilt angle is a very important parameter in the realization of NLC based devices and can allow a defect-free alignment and an improvement of electro-optical characteristics such as driving voltage, response time, color performance and viewing angle. It also represents a control parameter for estimating the alignment quality. In the case of homeotropic alignment the polar

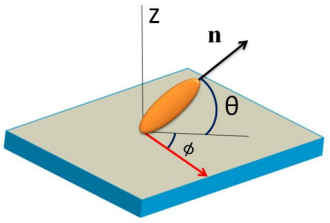

FIGURE 2.3: Orientation of n nearby the surface.

angle is equal to 90° and **n** is orthogonal to the surface. When **n** lies in the plane of the surface ($\theta = 0°$), two possible orientation cases exist: - homogeneous planar orientation, in which **n** is oriented uniformly over the surface and φ remains fixed; - heterogeneous planar orientation, in which the orientation of **n** is not uniform over the surface and φ assumes different values in different points of the surface. In the case of tilted orientation, θ is fixed while φ is arbitrary. To date, the two main techniques used to align LCs are: mechanical treatment and surface chemical functionalization.

2.3.1 Rubbing

A well known method to promote a given alignment of the NLCs director in contact with a surface is the mechanical rubbing (Figure 2.4) [23]. The surface of the glass substrate is covered with a thin organic film, such as polymide (PI), nylon, polyvinyl alcohol, etc. by means of spin coating or spray coating techniques. The most used polymer for the rubbing process is the PI due to its high curing temperature ($\sim 350°C$), good chemical resistance and excellent mechanical properties [24].

Spin coating allows to deposit a uniform layer on a flat substrate: a small amount of coating material is usually deposited on the center of the substrate which is then rotated at a given speed (rounds per minute, rpm) in order to spread out the coating material. The thickness of the film will depend on the number of rpm and on the viscosity and concentration of the coating material. After the deposition of the coating film, a cloth (velvet) with short fibers is moved over the surface in order to create microgrooves (Figure 2.4). The rubbing process induces a certain orientation of the polymer molecules, which is transmitted to the LC molecules anchored on the substrates; moreover, this kind of orientational order propagates in the bulk of the LC molecules via intermolecular forces [25].

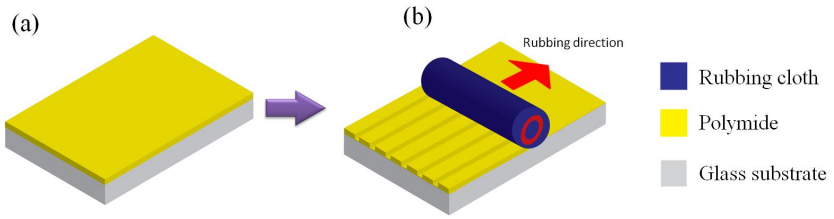

FIGURE 2.4: Rubbing method: (a) glass substrate covered with a polymide layer (a); process of rubbing by means of cloth rotation (b)

The rubbing technique enables to obtain both planar and tilted alignments, with a strong anchoring energy (defined as the energy needed to fix the NLC molecules to their easy axis). Although this technique is quite simple and can be easily scaled up (to large area devices), it intrinsically exhibits several drawbacks, such as contaminations, static charge accumulation and mechanical damages. These drawbacks have important consequences in the realization of displays, where the presence of even very small amounts of dust particles or static surface charges can lead to a deterioration of the display performances [26]. Furthermore, this technique is not applicable for achieving patterned alignment layers, necessary in some kinds of LC based devices.

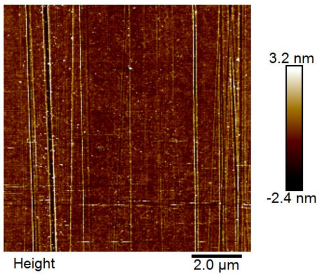

FIGURE 2.5: Atomic force microscopic image of the microgrooves morphology on a rubbed polymide surface.

2.3.2 Evaporation of SiOx

An alternative, non contact, method to align LCs consists in functionalizing the surface of the glass substrate with an amorphous film of SiOx. This method exploits a vacuum deposition technique that deposits thin films onto various surfaces by condensation of a vaporized form of the selected material, at a specific incident angle [27]. Characteristics of the deposited film strongly depend on the value of the incident evaporation angle and on other evaporation parameters such as pressure, temperature, etc. For silicon oxide films deposited at an incidence angle of of 60°, the LC director **n** lies parallel to the surface and is perpendicular to the plane

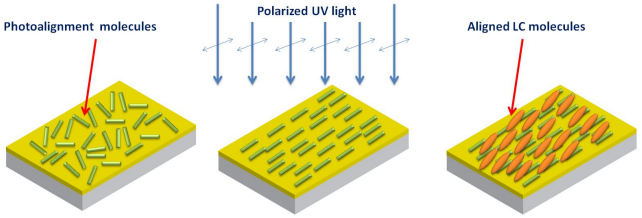

FIGURE 2.6: Photoalignment method.

of incidence. With a deposition angle of about 30° with the substrate normal, a uniform planar alignment is achieved with a 0° tilt. Finally, evaporating at an angle of 80° results in a tilted alignment [28]. However, this method turns out to be quite expensive, due to the cost of the used equipment (vacuum systems, evaporator, etc.).

2.3.3 Photoalignment

Another important, non contact, method used to align LCs is photoalignment. A photosensitive film of polymer is deposited on the surface of the glass substrate by means of spin coating or spray coating. Then the substrate is exposed to linearly polarized UV light (Fig. 2.6). Due to the dependence of the absorption of light by the molecules of the photosensitive film on the polarization direction, an anisotropic distribution of the orientation of the molecules of the alignment materials occurs; in this way the induced degree of surface ordering on the layer is further transferred to the LC molecules, that become oriented. Although the creation of orientational anisotropy by means of polarized light has been known since 1920 (Weigert effect) [29], the photoalignment mechanism in some materials is not yet fully understood, because the involved photochemical reactions are different in different photoalignment materials [26].

2.4 Optical Anisotropy of Liquid Crystals

The uniaxial symmetry around the director in the NLC phase leads to an anisotropy in many physical properties. For example, the refractive index, the dielectric permittivity, the magnetic susceptibility, viscosity and conductivity have a different values, depending on the fact that the external field is parallel to the director **n** or perpendicular to it.

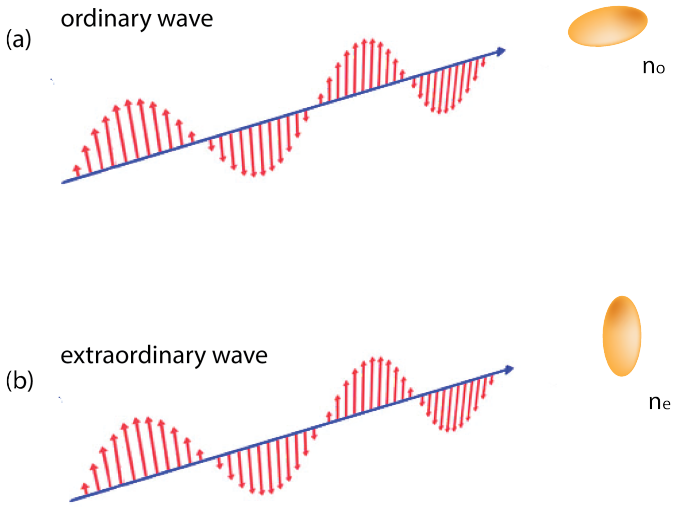

FIGURE 2.7: Light propagation in LCs along and normal to optical axis: (a) ordinary beam; (b) extraordinary beam; n_e - extraordinary refractive index; n_o - ordinary refractive index.

The anisotropy of NLCs causes light polarized along the director **n** to propagate at a different velocity than light polarized perpendicular to it; therefore, LCs are birefringent. A uniaxial NLC has two principal refractive indices: the ordinary refractive index n_o and the extraordinary refractive index n_e. The first one, n_o, is seen by the light wave whose electric vector is perpendicular to the optical axis (ordinary wave) (Fig. 5a). The index n_e is seen by the light wave whose electric vector is along the optical axis (extraordinary wave) (Fig.5b). The birefringence is given by:

$$\Delta n = n_e - n_o \tag{2.1}$$

In the case of uniaxial NLCs the optical axis coincides with the direction of **n** and the indices n_o and n_e are measured for light propagating along or normal to the optical axis. If the direction of light propagation is tilted with respect to the optical axis (Fig.6), the refractive index for the ordinary wave is equal to n_o, while the refractive index for the extraordinary wave is given by an effective value calculated as [21, 30]:

$$n_{eff}^2 = \frac{n_e^2 n_o^2}{n_e^2 cos^2\theta + n_o^2 sin^2\theta} \tag{2.2}$$

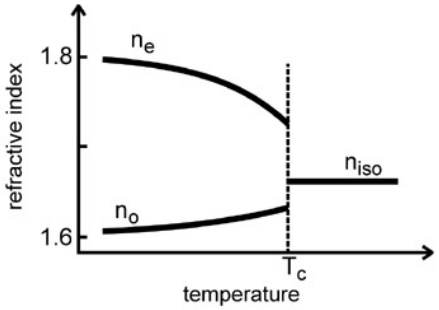

FIGURE 2.8: Temperature dependence of refractive index: T_c - clearing temperature (when the liquid crystal transforms into an isotropic liquid); n_{iso} - refractive index of isotropic liquid.

where θ is an angle between the optical axis and the light propagation direction. In this case the effective birefringence is $\Delta n = n_{eff} - n_o$. In general, birefringence Δn of LCs decreases as the wavelength of the incident light or the temperature increases (2.8).

Unpolarized light incident upon a NLC is splitted into an ordinary and an extraordinary wave, which travel with different velocities through the material [21, 30]. They emerge from the LC with some phase difference that depends on the thickness of material d

$$\Delta\varphi = 2\pi\Delta n d/\lambda \tag{2.3}$$

2.5 Dielectric Anisotropy in Liquid Crystals

Dielectric properties of LCs are related to the response of LC molecules to the application of an electric field. Permittivity is a physical quantity that describes how an electric field affects and is affected by a dielectric medium and is determined by the ability of a material to polarize in response to an applied electric field, and thereby to partially cancel the field inside the material. In LC materials consisting of non-polar molecules, there is only an induced polarization, which consists of two parts: the electronic polarization (which is also present at optical frequencies) and the ionic polarization. In LCs with polar molecules, there is in addition to the total induced polarization, the orientation polarization, due to the tendency of the permanent dipole moments to orient themselves parallel to the field. Considering the uniaxial NLC phase in a macroscopic coordinate system x, y, z, with the z axis parallel to the director $\mathbf{n}$, it is possible to distinguish two principal permittivities, parallel to the director $\varepsilon_{||} = \varepsilon_{zz}$, and perpendicular to the director

$\varepsilon_\perp = (1/2)(\varepsilon_{xx} + \varepsilon_{yy})$. Then the dielectric anisotropy $\Delta\varepsilon = \varepsilon_{||} - \varepsilon_\perp$ can assume positive and negative values. The graph of temperature dependence of dielectric permittivities for a typical NLC (Fig.2.9) shows that magnitude of $\Delta\varepsilon$ usually depends on temperature [21, 30]:

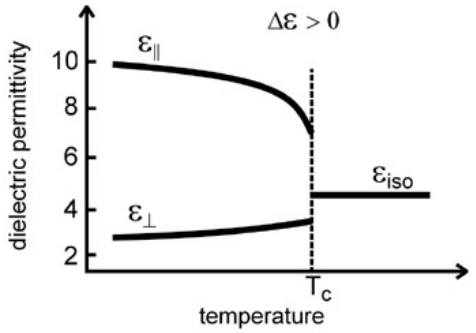

FIGURE 2.9: Temperature dependence of dielectric permittivity in liquid crystals with $\Delta\varepsilon > 0$: T_c - clearing temperature; ε_{iso}- permittivity of isotropic liquid.

2.6 Electro and pressure tunable Cholesteric Liquid Crystal devices

In this section we report an application based on the use of Cholesteric Liquid Crystal (CLC) as key-element in the realization of a pressure sensitive device.

It is well known that CLCs aligned in a planar configuration, (the refractive index varies periodically in the cell normal direction), exhibit a selective reflection band, as a 1D photonic structure: for wavelengths falling within this band, circularly polarized incident light, with the same handness as the CLC, is reflected, while the opposite handness is transmitted. Relationships between the reflected Bragg wavelength (λ_B), the bandwidth ($\Delta\lambda_B$) and the pitch (P) of a CLC reflection band are shown in eqn (2.4) – (2.6):

$$\lambda_B = \bar{n}P \tag{2.4}$$

$$\Delta\lambda_B = \Delta nP \tag{2.5}$$

$$P = 1/HTP[C] \tag{2.6}$$

where $\bar{n}$ is the average refractive index of the mixture, Δn is its birefringence, HTP is the helical twisting power [31] of the chiral dopant and $[C]$ is its concentration.

The device shown in Fig.2.10 has been made by starting from a flexible substrate of PDMS (Polydimethylsiloxane) where a gold electrode is directly integrated into its surface by using a low energy ($5\,keV$), high dose, ion implantation technique, called Filtered Cathodic Vacuum Arc (FCVA). This method leads to the formation of small gold clusters (2–20 nm in diameter) in the first $50\,nm$ below the PDMS surface.

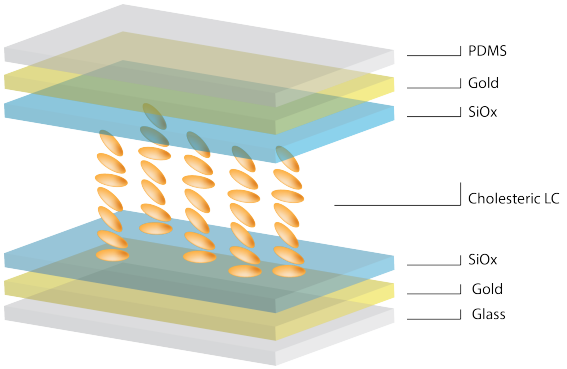

FIGURE 2.10: Sketch of the CLC configuration in the aligning cell.

The resulting PDMS conductive surface has been functionalized by evaporating on it a thin layer (approximately $30\,nm$) of SiOx, which induces a planar alignment of LC molecules deposited on it (see section 2.3.2). Then, the BL095 CLC by Merck (helix pitch $\lambda \approx 500\,nm$) is "sandwiched" between the treated PDMS microstructure and an ITO (Indium Tin Oxide) covered glass, which has been treated with a SiOx layer according to the same method. The two slabs are spaced by $4\,\mu m$ glass microspheres, while the CLC is introduced by capillary flow at room temperature; the CLC director **n** orients parallel to the substrates, while the helical axis goes normal to them.

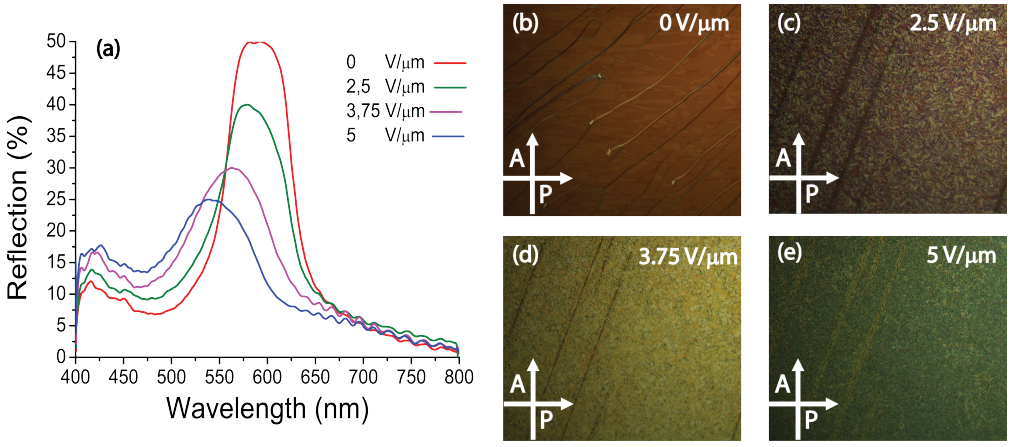

FIGURE 2.11: Spectral response (a) and POM view (b–e) of the sample under the influence of an external electric field.

The electro-optical response of the sample is tested by probing it with unpolarized white light (wavelengths in the range 400–800 nm) at normal incidence and by monitoring its back-reflected components by means of a reflection fiber. Fig. 2.11a shows the spectral response of the sample (structure sketched in Fig. 2.10, CLC aligned in planar configuration) for different values of an applied electric field (AC square voltage,1 kHz). The latter induces a deformation of the helix geometry, with a consequent blue shift of the CLC reflection band, due to a decreasing value of the effective CLC refractive index; in our case, this decrease can be roughly estimated as going from the value of 1.56 to the value of the ordinary index (1.50). The reflection band is also gradually suppressed: this is likely to be due to distortion of the CLC helix, which depends on the amplitude of the applied electric field [32].

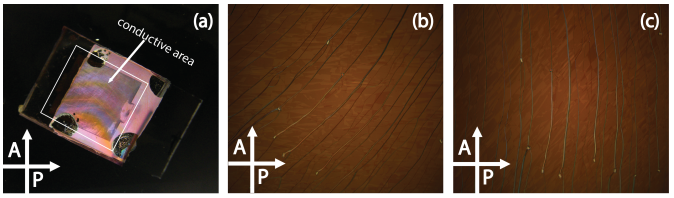

FIGURE 2.12: POM view of the sample infiltrated with CLC (a); high magnification POM picture of the sample oriented at 45° (b) and 0° (c) with respect to one of the polarizers.

It is worth stressing out that, in general, the presence of a very well defined reflection band (Fig. 2.11a, red curve) is a proof of CLC planar alignment. The behaviour of the sample is confirmed by the POM view reported in Fig. 2.11b–e; in fact, it is evident that the sample morphology is affected and a presence of conic textures (marker of a random aligned CLC phase) becomes quite clear while increasing the amplitude of the applied electric field. We also note that the reflection peaks (Fig. 2.11a) at non-zero applied electric fields are not symmetric but rather have a tail extending to shorter wavelengths. This asymmetry can be ascribable to the imperfect planar alignment in the sample, since the helical axis is tilted in a different direction with respect to the cell normal. Such asymmetry is not observed in the static condition ($0 Vm^{-1}$) due to the uniform and homogeneous alignment imposed by the functionalized surfaces of the cell. Usually, CLCs are aligned on ITO glass substrates, which can be functionalized with different alignment materials such as polyimide, PVA, SiOx, etc.; then by applying an external perturbation, it is possible to control some CLC properties. However, in these conditions, a mechanical stress applied to the glass substrates does not affect so much the CLC elastic properties, since glass is a rigid substrate and, therefore, it is quite difficult to propagate the perturbation to the bulk of the cell, in order to affect, e.g., the photonic band-gap.

In our case, on the contrary, the elastic performances of the soft PDMS substrate have been investigated by monitoring the behaviour of the sample reflection band under the influence of an external mechanical pressure.

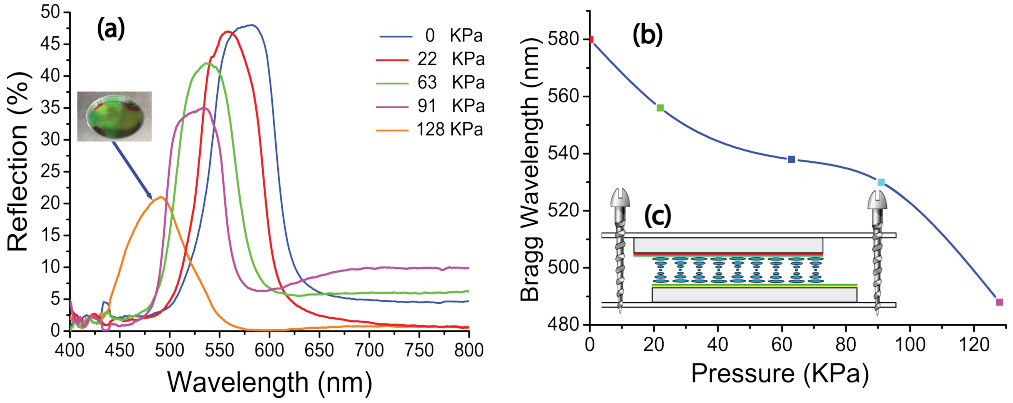

FIGURE 2.13: Spectral response (a) and band depth (b) of the sample for different values of the applied pressure (c).

A compression of the PDMS substrate has been induced by applying a uniform pressure on the glass substrate of the cell by means of a micro-stage with micrometer screws, according to the sketch reported in the inset of Fig. 2.13c. By doing so, the CLC pitch is compressed and consequently, according to eqn 2.4, the reflection band is blue-shifted of about $90\,nm$ (Fig. 2.13a). The observed reflection band shift induces a colour change of the sample area, similar to the one reported in ref. [33], which is evident from the inset of Fig. 2.13a. It is worth noting that in this particular experiment a measurement of the response time cannot be performed, since each determination of the new Bragg wavelength has been made after 1–2 minutes of waiting time, an interval that is necessary in order to minimize the influence of the hydrodynamic flow of the CLC under compression. the mechanical pressure has been evaluated by inserting a digital balance (sensitivity 1 g) between the compressing substrates and measuring the weight force (the angle between the applied force and the surface is 90°) for the same values of the translation distance used during the experiments reported in Fig. 2.13a. A force range spanning from $0\,N$ up to $0.012\,N$ has been found with a consequent whole pressure range applied to the sample, which is about $128\,kPa$ (the pressure range has been calculated by dividing each force value for the working area ($1\,cm^2$)). By plotting the Bragg wavelength versus the applied pressure (Fig.2.13b), a significant maximum blue shift can be observed, which is due to the CLC helix distortion that takes place during the compression of the sample. This mechanical modulation of the CLC reflection band has proved to be well reversible and repeatable.

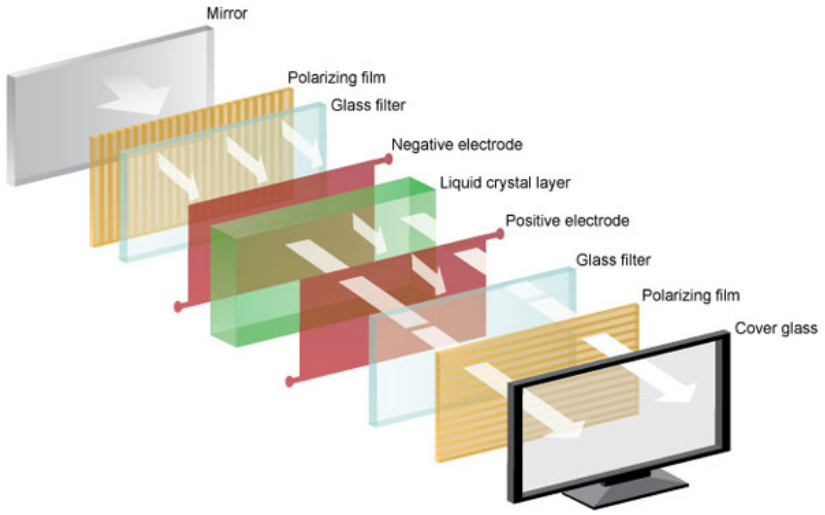

FIGURE 2.14: Sketch of the LCD active matrix.

2.7 Developing novel liquid crystal technologies for display and photonic applications

The most common application of liquid crystal technology is liquid crystal displays (LCDs). This field has grown into a multi-billion dollar industry, and many significant scientific and engineering discoveries have been made. A modern LCD requires novel technologies, such as new alignment methods to eliminate alignment layers, fast response, long operation time and so on. In this section we present an overview of recent advances on the liquid crystals (LCs) alignment for display applications, which includes superfine nanostructures, polymeric microchannels and polymer stabilized LCs. Furthermore, the main optical and electro-optical properties of new generation LCDs displays are analyzed by paying a particular attention to LCs blue phase hosting gold nanoparticles.

2.7.1 Advances in Liquid Crystal Alignment for Displays

LCDs have become important and indispensable in our everyday life due to their compact size, low power consumption and high-resolution density. LCs are a key component of the displays used in most laptop computers and the increasingly-popular flat panel televisions. Controlled by a network of transistors, LCs change their optical characteristics in response to electrical signals to create text and images.

The manufacture of panels is quite complex (Fig. 2.14), requiring multiple steps that can introduce defects. Among the steps there is the application of a polymer film (e.g. rubbed polyimide (PI), the so-called alignment layer) to the two pieces of conductive glass between which the LCs operate. The film, which must be rubbed after being coated on the glass, anchors the LCs with a fixed alignment (see section 2.3). The process of rubbing to create the necessary alignment can damage some of the transistors and introduce dust, producing defects that can reduce the manufacturing yield of the panels (see section 2.3.1). To overcome these issues, various LC alignment techniques have been investigated as alternatives to the PI rubbing approach (see section 2.3). The possibility of realizing a "surfactant free method" to align any kind of LC and self-organizing material is still an argument of ongoing research. In this section, recent advances on the LC alignment tchniques based on nanoimprint lithography (NIL) and an optical active polymeric template realized in soft-composite materials are discussed.

2.7.2 LC alignment by means of NIL technique

Surface grooves with a suitable pitch and depth are effective in aligning LCs [34, 35]. NIL can generate these grooves with a stable and precise pitch so as to lead to good LC alignment. Thus, NIL enables us to precisely control the direction of surface anisotropy and the surface anchoring strength through control of the pitch and depth on a mold, which is hardly possible in the conventional rubbing process.

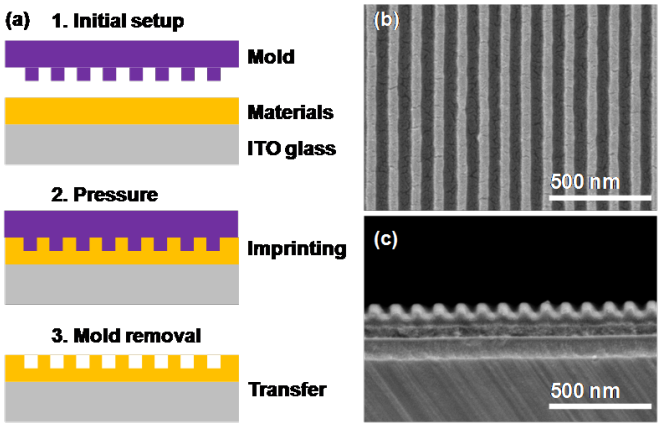

FIGURE 2.15: Typical nanoimprinting process (a); SEM images of top (b) and cross-sectional (c) views of an imprinted nanograting.

Figure 2.15a shows a typical nanoimprinting process. A hard mold that contains the designed features is pressed into a polymeric layer on a substrate at a controlled temperature and pressure, thereby creating a thickness contrast in the polymeric material. A thin residual layer of polymeric material is inevitably left underneath the mold protrusions, and serves as a soft buffer layer that prevents damages of the hard mold on the substrate and effectively protects the delicate nanoscale features on the mold surface. After imprinting, the mold patterns are clearly imprinted into the film having the correspondence as the mirror image each other. This imprint process can be repeated across the substrate areas to obtain multiple imprint fields on the substrate. Figure 2.15b and 2.15c show top and cross-sectional scanning electron microscopy (SEM) images of an imprinted nanograting in polymethylmethacrylate (PMMA) [36]. The high-throughput, ultrahigh resolution, and low-cost fabrication makes NIL an attractive and widely researched technology for many applications, such as Integrated Circuit (IC) semiconductor device, nanophotonics and displays. Most imprinting processes can be classified in two main categories: themo-printing and flash-printing, which require the imprinted materials to be thermo-curable and photocurable, respectively. NIL can enable periodic 1D, 2D and 3D structures [37–42], hence having the potential to align LCs in different ways. Various choice of imprinting materials will also affect the LC alignment. For that purpose, materials such as PMMA, poly(dimethylsiloxane) (PDMS), polyimide, SU-8 and polyurethane, have been widely tested. Among them, PMMA, a common material for the NIL, is used as a resist material because it has favorable thermal-mechanical properties like the low glass transition temperature $(T_g) \sim 90 \div 100^{\circ}C$, which is a favorable condition to avoid the damage of patterns on a mold surface. Depending on the imprinted material properties, both homogenous and homeotropic alignment can be achieved. The LC alignment on the imprinted surfaces can be examined under the polarized optical microscope (POM): If the POM images show very uniform darkness and brightness, this indicates that the imprinted surface successfully aligns the LC molecules.

Figure 2.16 shows an example of the POM view of the sample under the off and on states of a LC cell acted on by an external electric field [1]. In the off state, LC molecules remain perpendicular to the nanopatterned surface and the light transmission is prohibited, resulting in a dark image (Figure 2.16a). When the external electrical field is applied to the cell (on state), LC molecules shift to a horizontal position, parallel to the nanopatterned surface, and the LC cell clearly transmits visible light generated from backlight units, resulting in a white image (Figure

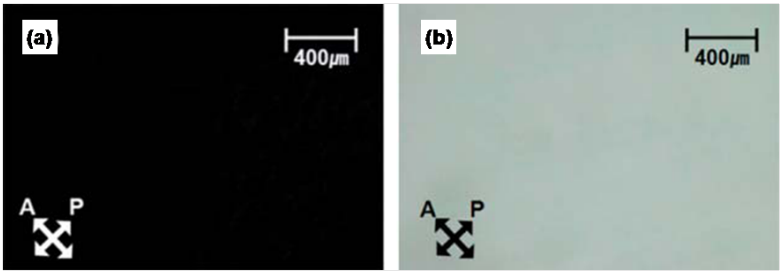

FIGURE 2.16: Optical microscopic images of the homeotropic LC alignment under crossed Nicols: (a) off-state with no applied voltage and (b) on-state with applied voltage of 5 V. This figure is adapted from reference [1].

2.16b). This indicates that a uniform LC alignment has been achieved in the nanopatterned cell. Investigation of the electro-optical properties of the fabricated cell is a direct way to examine the potential of a given nanoimprint technique for LCD applications. Using the imprinted pattern as the alignment layer, a LC cell working in different modes can be assembled and assessed in terms of various parameters (threshold, response times, contrast, etc.), which indicate the performance of display devices. For example, Takahashi et al. have successfully demonstrated homogenous LC alignment using 50 nm ultrafine line and space nanogratings [2]. A twisted nematic (TN) LC cell using the nanogratings as alignment layers showed excellent electro-optical characteristics, as depicted in Figure 2.17, where the measured contrast ratio of the TN cell is 44:1. In general, NIL presents great opportunities for LC alignment. Despite their advantages over the conventional rubbing method, current NIL and platforms are in the infancy stage and require further improvements in various aspects for practical applications. In particular, it is still very challenging to achieve large-area and uniform imprinted pattern for LC alignment. With increasing demand for nano/micro-patterns on large substrates, the establishment of large-scale fabrication technology for such patterns has become a priority. With the rapid development of the roller imprinting, it is therefore anticipated that over the coming years, fabrication of micro- and nano-scale structures over larger areas at a low cost will become industrially possible, hence making the large-area and uniform LC alignment feasible in developing novel LCDs.

2.7.3 LCs order in polymeric template

Some years ago Umeton and his coworkers [3] have realized a new kind of switchable diffraction grating named POLICRYPS (acronym of *POLymer LIquid CRYstal Polymer Slices*) , which

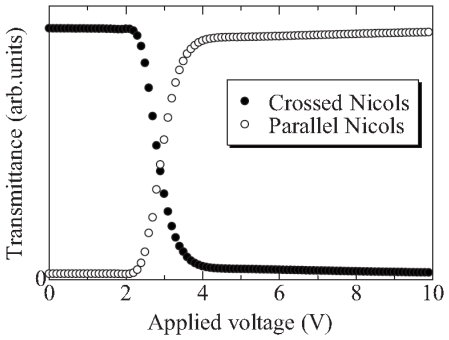

FIGURE 2.17: Transmittance vs voltage characteristics of the nanogrooved LC cell. This figure is adopted from reference [2].

is made of slices of almost pure polymer, alternated to films of well aligned NLCs. This composite structure is obtained by irradiating a homogeneous syrup of NLC BL-001 and prepolymer (NOA-61 by Norland, containing a UV sensitive photoinitiator), 28% and 72% in weight respectively, with an interference pattern of UV light, under suitable experimental and geometrical conditions. The curing process is carried out at a $100nm$ precision level, by utilizing an optical holographic setup that enables the spatial periodicity of the structure to be easily varied from the almost nanometric to the micrometric range [4]. Later on, it has been demonstrated that the POLICRYPS represents an excellent candidate to be used as a passive matrix for applications, due its unique morphological properties; in fact, the pure NLC confined between the polymeric slices can be easily removed in a selective way by exploiting a microfluidic etching process without opening the glass cell and the sample appears as made of sharp polymer slices separated by empty channels. Subsequently, the empty polymeric template (Figure 2.18a) can be filled with different materials including NLCs [5] cholesteric LCs (CLCs) [43], ferroelectric LCs (FLCs) [44], or liquid crystalline DNA [45] while importing long-range macroscopic alignment.

In order to show the extraordinary capability of the empty polymeric template to induce long range order in LCs compounds without any surface treatments, the empty POLICRYPS template (Figure 2.18a) has been back filled with the same NLC used during the curing process. The sample was infiltrated with NLC BL-001 at elevated temperature ($70^{\circ}C$) during the filling process to ensure that a complete transition to the isotropic state ($T_{N-I} = 67^{\circ}C$) had occurred. The self-organization process giving rise to uniform and stable alignment of the NLC within the micro-channels is induced after the filling process by slowly ($0.5deg/min$) cooling down the sample to room temperature. The excellent optical quality of the sample is evident in the

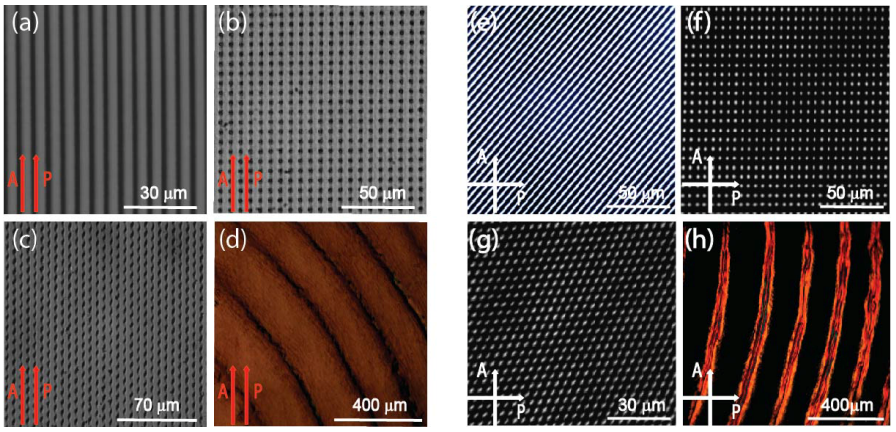

FIGURE 2.18: POM view of the polymeric template (a, e), 2D polymeric grid (b, f), lozenge hole geometry (c, g) and curved polymeric walls (d, h) between parallel and crossed polarizers respectively. The Figure is adapted from references [30, 31, 33]. [3–5].

POM image of Figure 2.18e and reflects the good NLC alignment. One more interesting aspect is represented by the possibility of realizing 2D composite photonic devices. First, the "empty POLICRYPS" structure has been infiltrated with the same curing mixture used for the fabrication of 1D POLICRYPS. A 2D grid is then obtained by simply rotating the sample and following again the standard two-beam interference procedure utilized for the POLICRYPS fabrication, without the need of any multiple beam interference pattern. The versatility of this technique allows choosing the geometry of the unit cell of the grid such as square hole geometry obtained with a 90° rotation before operating of the second curing step (Figure 2.18b) and a "lozenge" hole geometry obtained by a 45° rotation utilized for the second curing step (Figure 2.18c). Both geometries enable realization of microdomains with a strong asymmetry of the NLC director orientation as verified by POM analysis reported in Figures 2.18f-g. The self-organization of LC components on curved geometries represents also a very important key point for the realization of novel flexible displays. To this end, very recently De Sio et al. [46] have exploited the possibility to utilize the POLICRYPS technique for fabricating curved NLC geometries making use of a simplified (single beam curing process) holographic setup without the need for holographic mixing of two input beams. The gratings are photochemically formed using a single beam imaged through a commercially available Fresnel mask onto a glass cell which contains a slight modified curing mixture with respect to the one used for the fabrication of conventional POLICRYPS structures. The regular mixture composed by NLC BL-001 and NOA-61 was modified by adding a small amount (1% in weight) of the visible photoinitiator (Irgacure 784) in order to reduce the attenuation of the glass substrates as they absorb in the UV range. Figure

2.18d is a polarized image of a curved POLICRYPS structure, which exhibits concentric rings with a varying inter-distance made of curved polymeric slices which alternates with channels of well aligned NLC, whose molecular director is radially aligned to the polymeric slices, as evident in the high magnification POM images reported in Figure 2.18h. Technologies proposed here include not only absence of an alignment layer but also absence of haze, robust structure and inexpensive manufacturing. This is a unique opportunity and a big advantage compared to conventional liquid crystal devices. To date one of the main drawback of the standard two-beam interference procedure utilized for the POLICRYPS fabrication is represented by the difficulty to realize large area (more than 3 inches in diameter) structures. This technological limitation can be oversome by patterning different POLICRYPS structures on the same substrate while minimizing the edge effect by means of a high precision level motor stage. However, it is worth pointing out that the actual POLICRYPS size (up to 3 inches) is a "ready to go" technology for application such as smart-phones, digital watches and camera lenses.

2.7.4 LCs blue phase hosting gold nanoparticles for fast switching display

Cholesteric blue phase liquid crystals (BPLC) are highly chiral materials that self-organize into an arrangement characterized by strong helical twisting along a radial direction around a central director that is perpendicular to all twist axes, which are the so-called double twisted cylinders [47]. Blue phases (BP) exist within a very narrow temperature range between the isotropic and cholesteric phases. A total of three types of blue phases, Blue phase (BP)I BP II, and BP III, were discovered. Two (BP I and BP II) of the three types of blue phases pack into a cubic lattice on a scale ranging from one to two hundreds of nanometers, while the third type (BP III) is amorphous. The field-induced birefringence, the so-called Kerr effect, has been reported in a BPLC without the alignment layers. Recently, the polymerization of a small amount of reactive monomer in a BPLC became another breakthrough. The phase separated polymer tends to nucleate at the defect regions and is capable of stabilizing the cubic lattice against temperature variations [6]. With the discovery of new BPLC mixtures and polymer composites, fast switching displays have been explored [48]; however, the issues of high switching voltage, hysteresis, light scattering and long-term stability are still challenges for practical applications. Here, a study on the dispersion of gold nanorods (AuNR) in liquid crystal blue phase has been reported

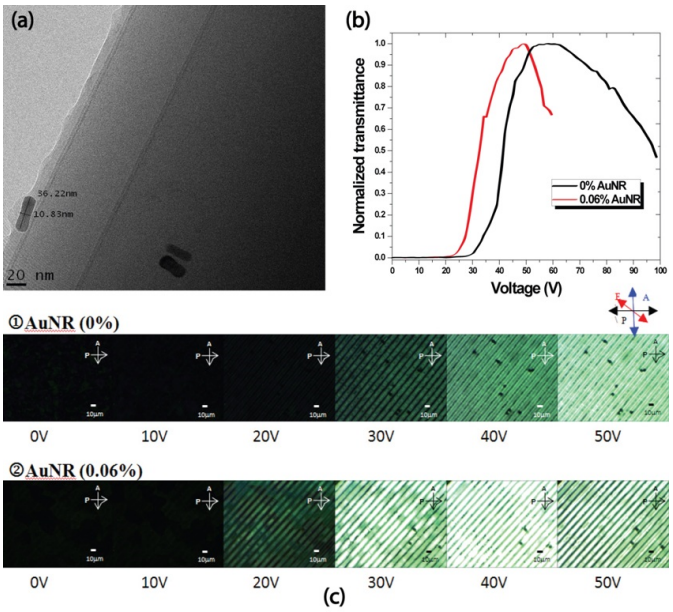

FIGURE 2.19: (a) TEM images of organo-thio monolayer protected AuNRs in 0.0006% AuNRs in blue phase liquid crystal at $50^{\circ}C$, (b) The transmittance-voltage (TV) curve of pure BP and 0.06% AuNR BP device, and (c) the POM images of (b) pure BP samples (c) 0.06% AuNR BP. The Figure is reproduced from reference [6].

by investigating the basis that may lead to an extended BP temperature range and enhanced electro-optical performances.

A BPLC mixture was prepared using a nematic LC (55.0 % of BL006, by Merck) and chiral dopant (45.0% of R811,by Merck) to give a helical pitch around 160 nm. Lab-synthesized with organo thiomodified AuNR dispersed in dichloromethane (DCM) with size of $10nm$ in diameter and $25 \sim 30nm$ in length (according to the information obtained from TEM study (Figure 2.19a)), was used as a nanoparticle additive. The doped BP LC mixtures were prepared by adding 0.6% of AuNR in the BP mixture, while keeping the nematic and chiral dopant at a constant $1 : 0.8$ ratio. A computer-controlled hot stage and a polarization microscope were used to determine the BP phase range. All samples were heated to the isotropic phase and cooled at a rate of $0.2^{\circ}C/min$ to room temperature. The reflection spectra were acquired with an Ocean Optics spectrometer as the temperature was varied. Electro-optical measurements of field induced birefringence required the use of in-plane-switching (IPS) cells with patterned indium tin oxide (ITO) of $5\mu m$ electrode line and $5\mu m$ electrode space on one glass substrate. The IPS cells were assembled with a second glass substrate, without ITO electrode, using ball spacers to separate the glass substrates with a cell gap of $5\mu m$ $(5/5/5)$. Through the use of capillary action the BP LC samples were filled at an isotropic state and allowed to slowly cool to the cholesteric

phase. Electro-optical measurements were carried out by aligning the stripes of electrode of the IPS cell at a 45° angle between the 90° crossed polarizers. Measurements of light transmittance as a function of applied voltage and response times were carried out at a constant BP state at $50°C$. The BP temperature range was increased up to $3.2°C$, and decreased with increasing concentration of AuNR in the BP mixture. We observe a shift to longer wavelengths in the doped BP samples with respect to the pure BP, which is independent of the temperature; the pure BP was range from $485\,nm$ to $500\,nm$, while 0.06% AuNR BP was shifted from $483\,nm$ to $580\,nm$. This longest shift supports the reported POM image (Figure 2.19). The electro-optical properties of the samples were investigated using IPS cells with $5/5/5$ of electrode space, line width and cell gap, respectively. An applied voltage to the cells at a constant temperature of $50°C$ shows the contrast between field-on (bright) and field-off (dark) states as seen in Figure 2.19b. The POM images reflect the behavior of the transmittance versus applied voltage curves both for pure and doped BPs (Figure 2.19c). With AuNR doping, the BP is switched to a stripe domain at a low voltage where the field is applied in the direction normal to the stripes. The discontinued stripes arise from imperfect electrode patterning during the substrate preparation. By contrast, the disappearance of the stripe domain for pure BP occurs at a higher voltage. The electro-optical study shows a reduction in the threshold voltage (V_{th}) of the doped 0.06% AuNR BP ($V_{th} = 27.3V$) with respect to the pure BP ($V_{th} = 34.6V$). The AuNRs doped BPLC exhibits the same light transmission as that of the BPLC at the field-on state at a low voltage. One of the features of BPLC is its fast response time. In the measured response time of the pure BPLC, the rise time was $2.1ms$ and the fall time was $1.7ms$. Conversely, in the response time studies of the 0.06% AuNR doped BPLC, the rise time was $15.3ms$ and the fall time was $5.9ms$. The response time of 0.06% AuNR doped BPLC is slightly higher than that of the pure BPLC. This is because the rise time for the AuNRs doped sample is slower if the applied voltage is close to the critical voltage to unwind the cholesteric pitches (V_c) [49]. To speed up the turn on time, one should apply an overdrive voltage to the device. The analysis shows that the fall time of AuNRs doped sample is about twice slower than that of the pure BPLC; this could be due to the increase in rotational viscosity arising from the inclusion of AuNRs at the disclinations, which requires extra energy for local double twists to overcome the extra exclusive volume of the AuNRs [50]. This study has demonstrated that BP is stabilized as a result of doping with AuNR. The BP temperature range was increased up to $3.2°C$, and decreased with increasing

concentration of AuNR in the BP mixture. The appearance of orange and red domains in POM images is supported by reflection spectra data showing a shift to longer wavelengths with respect to non-doped BP liquid crystals. It is seen that the greatest shift in the maximum wavelength occurs with 0.06% AuNR BP. This suggests that AuNRs successfully stabilize the BP medium and optimize thermal stability at low concentrations. In the electro-optical induced Kerr effect, the optimization in the doped AuNR BP LC device also led to a reduction in threshold voltage (V_{th}); V_{th} (34.6V) for pure BP, and (V_{th}) (27.3V) for the doped BP mixture.

Chapter 3

Liquid Crystals as active medium in Plasmonics

3.1 Introduction

The distinctive properties of Liquid Crystals (LCs) foster new possibilities in plasmonics. The combination of the intrinsic tunability of LCs with the plasmonic properties of metallic nanoparticles (NPs) provides novel and intriguing features of systems, commonly identified as *active plasmonics*. Being LCs media whose refractive index can be controlled through the application of external stimuli, they represent a convenient host for enabling plasmonic tunability. On the other hand, the localized surface plasmonic resonance (LSPR), typical of NPs, can strongly influence and control the behaviour of LCs. In this chapter, an overview of several systems of NPs combined with NLCs arranged in different configurations is presented. The properties of the resulting systems suggest novel, intriguing outcomes in both fundamental and applied research.

3.2 Gold nanospheres immobilized on a substrate and layered with nematic liquid crystals

An active plasmonic system can be obtained by assembling random arrays of gold NPs (GNPs) immobilized on a conductive substrate and layered with nematic LCs (NLCs). This system

offers a two-fold advantage because large area samples can be easily fabricated as the result of a bottom-up and self-assembly procedure, whereas the randomness of particle distribution assures that optical properties are independent of the polarization of the probing light.

In the experiments GNPs have been prepared according to the Turkevich method, described in details elsewhere [51]. NPs fabricated by using this technique show a characteristic negative surface charge, which arises from the mono-layer of citrate capping molecules. The simple dipping of a substrate, suitably functionalized to possess a positive surface charge, in a solution of GNPs can result in a single layer of GNPs deposited at the substrate surface. Indeed, the negatively charged particles stick on the positively charged surface while their electrostatic repulsion induces their self-organization in a mono-layer. The ITO-coated glass substrates were functionalized by first exposing them to a solution of H_2O_2 (30%) for 30 minutes before washing with copious amounts of Milli-Q water $(18.2M\Omega \cdot cm)$. After drying in a stream of compressed air, the substrates were immersed in a $5\%(v/v)$ solution of N-[3-(Trimethoxysilyl)propyl]ethylenediamine in ethanol for 30 minutes and were again rinsed with water; then, dried and set in an oven at $120°C$ for a further 30 minutes. In order to deposit a second GNP array at a well-defined distance from the first one [51], a series of charged polymer layers were assembled by exploiting, once more, electrostatic interactions [52]. In the actual case, seven polymer layers, consisting of the positively and negatively charged poly-(allylamine hydrochloride) and poly(sodium 4-styrenesulfonate) respectively, were assembled in between the two GNP arrays. Polymers had a concentration of $5mg/mL$ in $0.1M$ NaCl and were deposited for one minute before rinsing with water and drying under a stream of compressed air. All measurements, excluding the SEM image, which was taken on a single GNP array, were made on two GNP arrays separated by seven polyelectrolyte (PE) layers. This choice is due to the fact that, by means of PE layers, it is possible to carefully adjust the distance between adjacent GNP arrays and hence control the spectral position of the LPR. This multi-step process is known as *layer-by-layer assembly* and allows the realization of suitable layered arrays of GNPs.

Figure 3.1a,b is a Scanning Electron Microscopy (SEM) image of the GNPs distribution; they are well dispersed and approximately equally spaced (with an average radius of about $10nm$) even if no discernible long-range organization can be observed. The Atomic Force Microscopy (AFM) topography reported in Figure 3.1c,d confirms this result: the analysis shows an average radius of about $15nm$ with a modulation depth of $22nm$ (see color scale, Figure 3.1). The

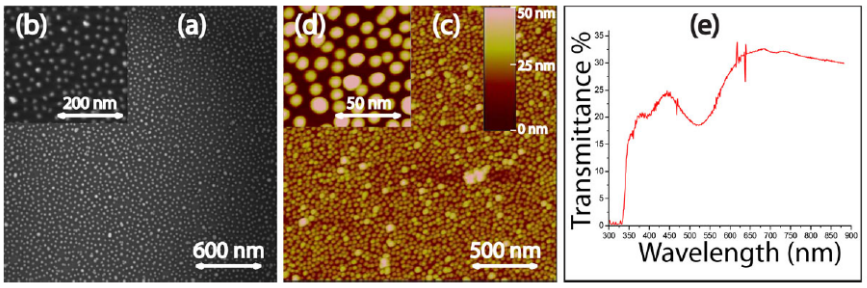

FIGURE 3.1: SEM view (a) and its high magnification (b), AFM topography (c) and its high magnification (d) of the GNPs distribution. Spectral response of the sample (e).

discrepancy in the measured radius between the SEM and the AFM characterization is attributed to the convolution between the AFM tip ($\sim$ tens of nm) and the average size of the GNPs, that is of the same order of magnitude; conversely, due to the high vertical resolution (up to 0.1 *nm*) the modulation depth represents an accurate measurement of the GNP diameter, in agreement with the diameter inferred from SEM measurements. The spectral response of the GNP arrays has been investigated by probing the sample with unpolarized white light (wavelengths in the range $300-900\,nm$) impinging at normal incidence. In Figure 3.1e, a pronounced absorption peak at $\lambda = 522\,nm$ with a measured extinction coefficient of $\approx 10\%$ is observed. Both the spectral position and the narrow width of the peak confirm the existence of a LSPR due to the presence of well-dispersed GNPs [53]. Of course, given that the exciting light propagates through the afore mentioned multilayer system, the obtained spectral response is to be considered as an average information and no distinction of the contributions of the single layers can be made.

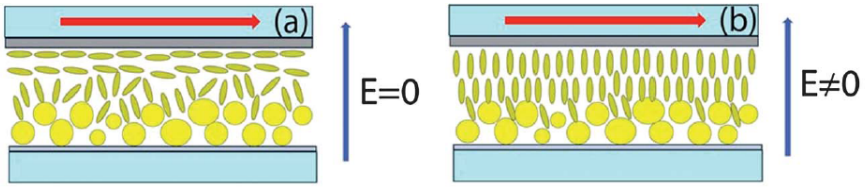

FIGURE 3.2: Sketch of the NLC configuration inside the sample without (a) and with (b) application of an external electric field.

In order to exploit the reconfigurability properties of the NLC, used as a surrounding medium for the GNPs, and achieve an active control of their LSPR, a glass cell has been realized by combining a conductive cover glass, treated with a thin polyimide layer for inducing a planar alignment of the NLC, with a substrate containing GNP layers. Glass and GNP-coated substrates were kept at a controlled distance by $4\,\mu m$ glass microspheres and the NLC (E7, by Merck) in isotropic phase ($65^{\circ}C$), has been introduced by capillary action. The NLC possesses a hydrophobic alkyl

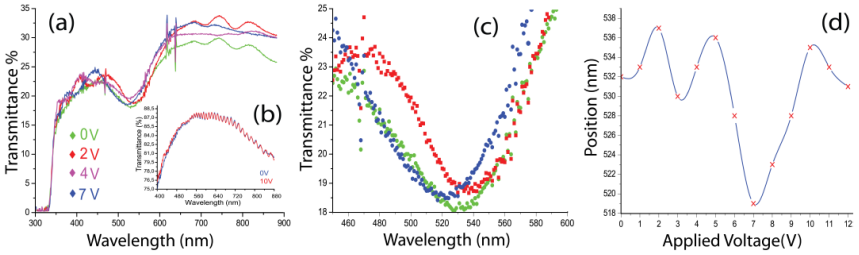

FIGURE 3.3: Spectral response of the sample for different applied voltages (a) and its higher magnification detail (c). Position of the center of the plasmonic resonance versus the external voltage (d). In (b), the spectral response of an identical cell, filled in with the same LC material and without any GNPs, under the effect of an externally applied electric field.

chain and a hydrophilic cyano head group [53] and, in the bulk of the cell, its director exhibits a hybrid configuration due to a competition between the almost homeotropic alignment, induced by the electrostatic interaction with GNPs on one side of the cell, and the planar alignment due to the functionalized top cover glass on the other side (Figure 3.2a).

This hybrid configuration provides an intriguingly interesting environment for the realization of electro-optic effects. Under the influence of an electric field applied to the planar cell, the NLC director is reoriented (along the field direction, Figure 3.2b), thus changing the effective birefringence Δn of the device and modulating the transmitted light intensity. In order to check the influence of the birefringence variation on the LSPR of the GNP array, the spectral response of the sample has been characterized by probing it with unpolarized white light at normal incidence for different values of the applied voltage; obtained results are reported in Figure 3.3.

By increasing the applied voltage, the plasmonic absorption peak exhibits a *dancing behavior* with a continuous blue-red shift of its spectral position (Figure 3.3a). In order to exclude that closed-cell multiple reflections could be responsible of this peculiar behaviour, the same experiment has been repeated with an identical cell filled in with the same liquid crystals but without any GNPs on the substrates. Even if multiple reflection oscillations are observed in transmission, upon applying an external electric field to the cell, no wavelength shifts are present in the range of interest (Figure 3.3b). The *dancing behavior*, which is very well evident in the high magnification of Figure 3.3c, is in contrast with the optical behavior predicted by the Mie theory [18] for a dispersion of isolated spherical particles. In fact, this theory predicts a linear dependence of the resonance wavelength (assumed to correspond to the local minimum of the transmission) on the value of the refractive index of the surrounding medium (a monotonic red or blue shift

for increasing or decreasing values of the refractive index, respectively), when considered in a specific small range. In the case under test, a decrease, roughly estimated from 1.60 to 1.50, of the NLC refractive index value, obtained under the influence of the external electric field, should yield a blue-shift of the plasmon resonance wavelength. Moreover, the real refractive index change, experienced by the LC molecules in proximity of the GNPs, will be even less because, upon application of the external electric field, they undergo a small reorientation from almost homeotropic to fully homeotropic. In these conditions, theoretical predictions suggest that the influence of the refractive index variation on the plasmon resonance spectral position should be limited [16-19]. The experimental observation is instead a quite surprising non-linear modulation of the resonance wavelength (Figure 3.3d). This unusual behavior might be explained by taking into account the influence of the ITO layer underlying the GNP array. Indeed, Feigenbaum et al. [54] have recently demonstrated that, by shifting the plasma frequency of free carrier accumulation layers, it is possible to observe unity order refractive index variations. This effect takes place when an external electric field is applied to a system where an ITO layer is separated from a gold one by a dielectric layer (SiO_2, in their case). Under this condition, a $5\,nm$ thick accumulation layer appears at the dielectric/ITO interface, and the field increases the carrier concentration from 1021 to $1022\,cm^{-3}$. It is worth noting that no refractive index modulation is observed unless the SiO_2 layer is present. This remarkable result has been exploited to obtain an electro-optical and all-optical control of plasmon modes of individual nano-antennas using the nonlinear response of nanoantenna-ITO hybrids [54, 55]. In our case, because of the organosilane layer used to functionalize the glass/ITO substrate (according to the method described above), the system under test is similar to the one described by Feigenbaum. As such, it is reasonable to expect the formation of an accumulation layer at the organosilane/ITO interface and then a refractive index variation on field application; as a result, due to the refractive index variation, the accumulation layer behaves as an additional *active* medium. In order to verify this hypothesis concerning an effect of the free carrier accumulation layer on the plasmonic resonance, electro-optical experiments have been performed by using an empty glass cell (similar to the previously described one, but having air instead of NLC). Obtained results are reported in Figure 3.4a.

By increasing the applied voltage, from $0V$ to $10V$, a monotonic red-shift of about $9\,nm$ is observed, as reported in Figure 3.4b, where the variation of the plasmonic resonance wavelength

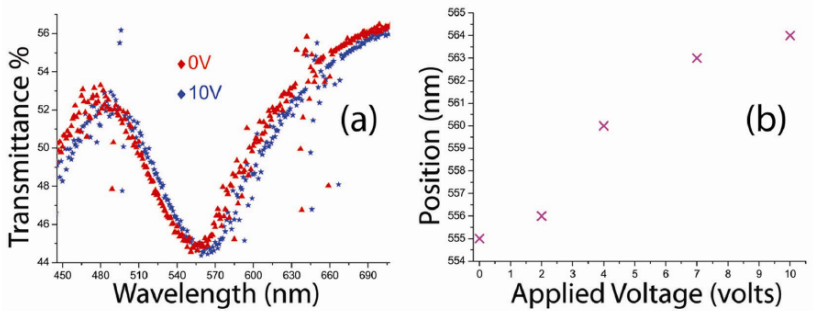

FIGURE 3.4: Spectral response of the empty sample (a) and plasmonic resonance wavelength (b) versus the external voltage.

(local minimum of the transmission) versus the external voltage for the empty glass cell has been reported. This result suggests that, under the influence of the external electric field, the carrier accumulation and the NLC layers enter somehow in competition as *active* media surrounding the GNPs layer. The exact way they contribute to the position of the plasmonic resonance wavelength is not yet clear and will be further investigated; most probably, depending on the value of the applied voltage, they combine their effects causing either an increase or a decrease of the value of the effective refractive index of the medium surrounding the GNPs layer. Most probably, by combining their effects, ITO and LCs together play a larger role (Figure 3.3c) than the one LCs could play alone. In more detail, the accumulation layer at the $organosilane/ITO$ interface is expected to play on the first gold layer mainly, whereas the liquid crystal is expected to play more on the second one.

3.3 Gold nanorods immobilized on a substrate and layered with nematic liquid crystals

Gold nanorods (GNRs) represent an interesting class of NPs. Their peculiarity is to show two (transverse and longitudinal) LSPRs located at different wavelengths (from visible to NIR) that depend on the particle size and aspect ratio [57]. The longitudinal resonance exhibits very high sensitivity to refractive index variations of particles surrounding medium [58]. Following the strategy described in the previous paragraph, the realization and characterization of large scale ($\sim cm^2$) GNRs arrays immobilized on an ITO coated glass substrate and layered with an NLC film that is used as an *active* surrounding medium has been carried out. GNRs have been

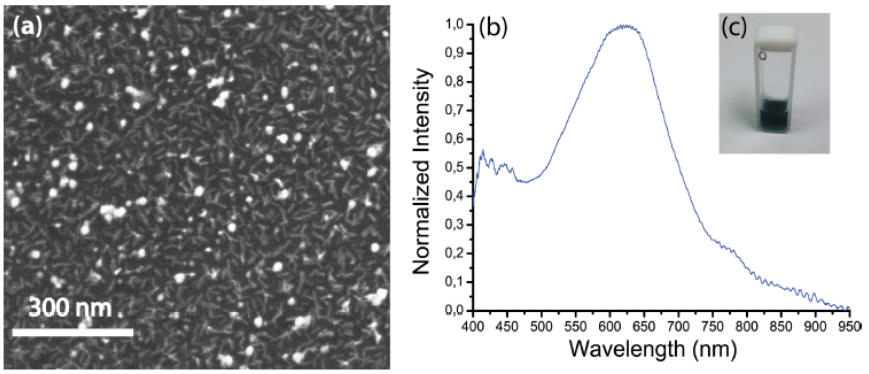

FIGURE 3.5: SEM view (a) and spectral response (b) of the GNRs distribution. Picture of the quartz cuvette containing the water based GNRs dispersion (c).

prepared according to the seed-mediated growth method described in detail elsewhere [59]. GNRs are positively charged due to the surrounding bilayer of cetyltrimethylammonium bromide (CTAB); a layer of negatively charged Poly(sodium 4-styrenesulfonate) (PSS) has to be deposited on the first positively charged layer. The ITO-coated substrates were prepared as reported above for the GNPs deposition but, in this case, they were immersed for 2 minutes into a solution of PSS ($5mg/mL$ in 0.1 M NaCl) and were again rinsed with water and dried in a stream of compressed air. The substrates were then left in a 200 mM NaCl solution of GNRs overnight, and again rinsed with water and dried in a stream of compressed air. Figure 3.5a is a Scanning Electron Microscopy (SEM) image of the obtained GNRs distribution; it shows well dispersed and approximately equally spaced rods with ~ 2.6 aspect ratio (AR). The GNRs are randomly distributed and oriented and exhibit no discernible organization on the surface. The GNRs distribution exhibits a quite broad longitudinal band at $619\,nm$ (Figure 3.5b), which overlays the transverse one at $525\,nm$. This overlap can be avoided by red-shifting the longitudinal band to the near infrared (NIR) by slightly increasing the AR (small changes in AR lead to drastic changes in the position of the longitudinal band).

To depict the sample fabrication and characterization procedure, a sketch of the step by step processes has been reported in Figures 3.6a,b, where with TP and LP are indicated the transversal and longitudinal polarization direction with respect to the long axis of the GNRs substrate respectively. Figure 3.6a sketches a GNRs substrate while Figure 3.6b shows planar aligned NLC. In the above described fabrication process, both GNRs and ITO coated glass substrates have been functionalized with polyimide layer, rubbed by a soft tissue in order to induce a planar alignment of the NLC molecules; then, the NLC (MDA-00-1444, by Licristal) is *sandwiched*

between the treated GNRs substrate and the top cover glass. The two substrates are spaced by $10\,\mu m$ glass microspheres and the NLC is introduced by capillary flow at room temperature; the NLC director **n** orients parallel to the substrates (along the TP direction). In a second step, we have performed a spectral analysis of the sample by considering two different polarizations of the probe light (LP and TP) as depicted in Figure 3.6b. Figure 3.6c compares the absorption spectra of the GNRs substrate, with and without the NLC overlayer. Without the NLC overlayer (Figure 3.6c, blue curve) sample exhibits a longitudinal band at $619\,nm$. In order to take into account the NLC birefringence, we have performed a polarized spectral analysis of the sample. The influence of light polarization on the optical response of the sample is shown in Figure 3.6c (red and magenta curves), which reports the spectral analysis for impinging LP (red curve) and TP (magenta curve) radiation. The two peaks are red-shifted of about 3 and $6\,nm$ respectively with respect to the GNRs substrate (Figure 3.6c, blue curve). This effect can be explained by taking into account the fact that the optical properties of ellipsoidal particles are predicted by Gans theory [60] and in this framework, the spectral position of the LSPR peak depends on the refractive index of the dielectric material surrounding the GNRs. In our particular case, the presence of the NLC layer increases the local refractive index near the GNR layer. The refractive index of the GNRs substrate is ~ 1 (we consider air as surrounding medium) while the LC ordinary (n_o) and extraordinary (n_e) indices at $\lambda = 630\,nm$ are 1.54 and 1.67 respectively. Specifically, LP light will experience a refractive index variation from 1 to 1.54 while for TP light, the refractive index varies from 1 to 1.67.

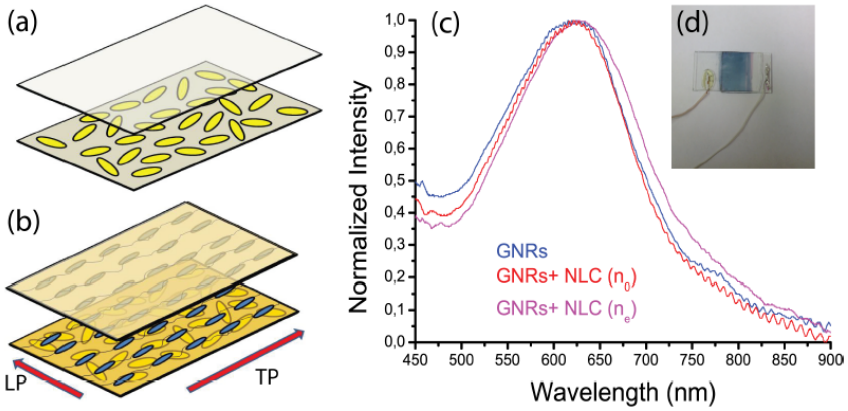

FIGURE 3.6: Sketch of the GNRs distribution without (a) and with (b) NLC layer along with their spectral response (c). Picture of the large area ($1\,cm^2$) sample (d).

Surprisingly, despite the longitudinal resonance exhibits a very high sensitivity to variations in the refractive index of the surrounding medium, in the actual case, we have observed only $9\,nm$

shift. This behavior can be explained by considering that the LSPR oscillation is confined onto a $30-40\,nm$ thick layer at the surface; in this case, in order to induce the planar alignment of the NLC layer, a quite thick ($\approx 100\,nm$) polyimide layer has been deposited (this expedient was necessary to protect the GNRs substrate during the rubbing process); thus, being GNRs encapsulated in the alignment layer, they are closer than $100\,nm$ to NLC molecules and evidently close enough for the NLC to influence the LSPR spectral position, even if in a very limited way. However, in a similar approach, it has been already demonstrated an efficient way to overcome this suppression at the surface, through the use of a Photo-Alignment Layer (PAL) whose local orientation can be modulated using polarized light [61]. This few nanometer ultra-thin film, acts as a command layer for controlling the LC order directly on the surface and localizing a change of the LC refractive index around the GNRs.

In order to verify the active plasmonics properties of the system, the sample has been placed at 45° between crossed polarizers and the transmission spectrum of the system (polarizer+sample+analyzer) has been acquired with a spectrometer. During the experiment, the refractive index value of the nematic liquid crystal has been modified through the use of an a.c. voltage (square wave, 1 KHz) externally applied to the cell. Figure 3.7a shows the transmission spectra of the sample while increasing the amplitude of the electric field.

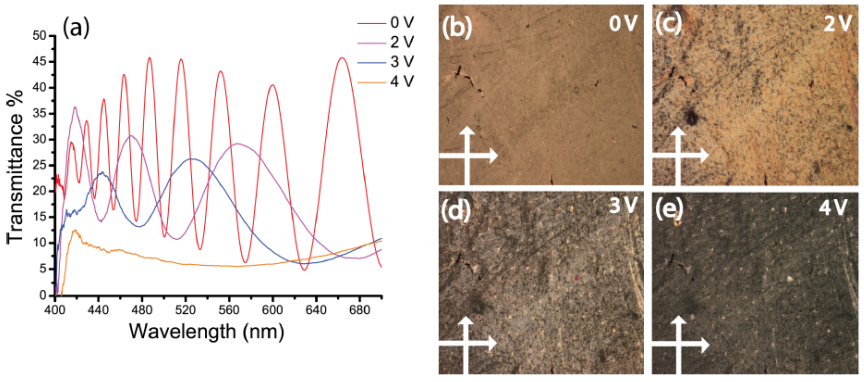

FIGURE 3.7: Spectral response of the sample placed at 45° between crossed polarizers while increasing the externally applied electric field (a) and related POM view (b-e).

The sinusoidal like behavior reported in Figure 3.7a can be explained by considering that the transmission ($T_\perp$) of light through a birefringent medium placed at 45° with respect the polarizers-analyzer axes is given by:

$$T_\perp \propto sin^2 \frac{\pi \delta n d}{\lambda} \tag{3.1}$$

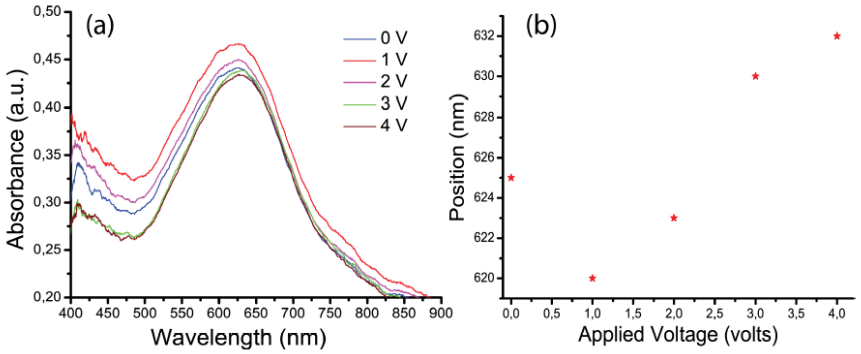

FIGURE 3.8: Spectral response of the sample (a) and position of the center of the plasmonic resonance (b) for different applied voltages.

where λ is the wavelength in vacuum, δn the sample birefringence and d its thickness. Keeping fixed the values of d and δn and varying λ, $T_{\perp}$ undergoes through maxima and minima (red curve, Figure 3.7a) inducing a suppression of different parts of the visible spectrum, and, therefore, in general, a non-white colour response as evidenced by the Polarized Optical Microscope (POM) view reported in Figure 3.7b. It is worth noting that, due to the NLC molecular director reorientation (along the electric field direction),δn is gradually reduced with a consequent blue shifted spectral response (see magenta, blue and orange curves in Figure 3.7a) and color change (Figures 3.7c-e). Indeed, according to equation 3.3, by gradually decreasing δn, it is possible to maximize $T_{\perp}$ for smaller values of λ (blue shift range). Moreover, the spectral analysis reported in Figure 3.7a has been used for evaluating the absolute value of δn and its variation under the influence of the external electric field. Indeed, the argument of equation 3.3 can be maximized by fulfilling the following relationship:

$$\frac{\pi \delta n d}{\lambda} = m\pi \tag{3.2}$$

As a result, a δn variation of about 0.095 has been measured; this value is lower than the one measured in presence of the same material planarly aligned in a conventional glass cell ($\delta n \approx 0.2$). This difference can be explained by considering that the effect of the GNRs substrate, despite the presence of the quite thick alignment layer, affects the NLC average orientation as well. Most probably, the electrostatic interactions, induced by the presence of the NRs, result in a lowering of δn. In order to check the influence of the birefringence variation on the plasmonic resonance of the GNRs array, the LSPR of the sample has been analyzed by probing it with polarized (TP) white light at normal incidence for different values of the applied voltage;

obtained results are reported in Figure 3.8. By increasing the applied voltage, the LSPR peak exhibits a *dancing behavior* with a blue-red shift of its position (Figure 3.8b). This behavior is in contrast with the optical properties of ellipsoidal particles predicted by Gans theory [60] but it can be considered as a further confirmation of the similar behavior reported in the previous paragraph. In that case, it has been supposed the presence of a carrier accumulation layer that, together with the NLC layer, competitively contributed to the effective refractive index value of the medium surrounding the nanospheres, which results in the non-monotonic shift of the LSPR wavelength position. This time, being the sample realized with a similar technique, except for the shape of the nanoparticles, it is also reasonable to hypotesize the presence of the accumulation layer and hence understand the behaviour reported in Figure 3.8.

Chapter 4

Templating gold nanorods with liquid crystalline DNA

4.1 Introduction

A liquid crystalline, negatively charged, whole-genome DNA is exploited to organize positively charged gold nanorods (GNRs) by means of electrostatic interaction. A mesoscopic alignment of the composite system along a preferred direction is obtained by casting a droplet of the DNA nanorods solution onto an untreated glass substrate. Gel electrophoresis analysis enables evaluating the effective electric charge of the system, thus minimizing the DNA fragmentation. Polarized optical microscopy, combined with transmission and scanning electron microscopy, shows that, up to 20% in weight of GNR solution, the system exhibits both a long range order, induced by the liquid crystalline phase of the DNA, and a nanoscale organization, due to the DNA self-assembly. These evidences are confirmed by a polarized spectral analysis, which also points out that the optical properties of GNRs strongly depend on the polarization of the impinging probe light. The capability to organize plasmonic nanoparticles by means of DNA material represents a significant advance towards the realization of life science inspired optical materials.

4.2 DNA based nanostructures

Self-assembly indicates a process whereby a large quantity of molecules and subunits undergo spontaneous organization to form larger ordered structures driven by internal interactions or external constraints. A careful control of the basic mechanisms of self-assembly, involving material properties, electrostatic interaction and surface chemistry, has been widely used to design and fabricate devices based on nanomaterials with original, suitably designed, optical properties. Metamaterials are a particularly exciting example of such a kind of materials; they are formed by an arrangement of artificial structural elements designed to achieve unique electromagnetic properties, which open the way towards innovative applications, such as high-resolution imaging [62], cloaking devices [63], data storage [64], sensors [65], solar collectors [66]. The modeling and manufacturing of such particular materials has been possible thanks to recent advances in the field of nanotechnology (with a top-down approach) and material science (exploiting self-assembly, or bottom-up approach). The top-down strategies take advantage of lithographic tools to pattern nanoscale structures on a substrate, while the bottom-up approaches exploit interactions among basic constituents (molecules) to realize self-assembling in nano-ordered structures. In this framework, metallic nanoparticles (MNPs) represent a unique class of building blocks for realizing optical metamaterials that can exhibit, for instance, a negative refractive index [67]. MNPs have the capability to localize light down to the nanoscale through the excitation of the Localized Surface Plasmon Resonance (LSPR). Such a phenomenon, due to the oscillation of the free electrons localized at the metal (MNPs)/dielectric (surrounding medium) interface, can be induced by visible radiation; moreover, the LSPR frequency can be tuned by varying both size and shape of the MNPs and/or the dielectric constant of the surrounding medium [68]. A particular class of MNPs is represented by gold nanorods (GNRs), that are characterized by two LSPRs, the transverse and the longitudinal one, respectively, whereby the frequency of the last one can be tunable from visible to NIR, as it is a function of the particle aspect ratio (defined by nanorod length/diameter ratio) [57]. Moreover, for ordered systems, the optical properties of GNRs depend on the polarization direction of the incident light since, for light polarized along the average orientation of the long axis of GNRs, the LSPR is dominated by the response of the longitudinal resonance. Bottom-up techniques based on self-assembly of MNPs have been widely explored in the last few years; in particular, DNA-based nanostructures have received great attention, since DNA is a flexible polymer that exhibits, besides its specific structural

properties, both self-organization and molecular scale recognition. In one of the earlier experiments in the area of DNA based assembly, Alivisatos et al. [69] originally demonstrated that a discrete numbers of gold nanocrystals were organized in periodic structures by the interaction with molecular DNA. More recently, artificially designed self-assembled DNA nanostructures have been reported in various topological systems and with different functionalities: 1D and 2D periodically patterned structures [70], nanomechanical devices [71], and molecular computers [72]. From a different point of view, an interesting phenomenon is represented by the tendency of flexible polymers in concentrated aqueous solutions to form liquid crystalline phases. Indeed, the ability of both long [73, 74] and ultrashort, hydrated [75], double-stranded DNA molecules to form liquid crystal (LC) phases has been known for more than 50 years and played a key role in the initial deciphering of the molecular DNA. In the following it is reported the realization and characterization of a self-assembly method applied to an aqueous solution of GNRs dispersed in liquid crystalline DNA.

4.3 Organization of GNRs in a self-assembly process driven by the DNA

In the considered systems, the electrostatic interaction between GNRs and DNA has proven to be able to organize GNRs in a self-assembly process driven by the DNA mesophase. A whole-genome DNA extracted from human blood, containing approximately $10k$ base pairs (1 bp length $\approx 0.34\,nm$) and with a contour length of about $3.4\mu m$ has been used.

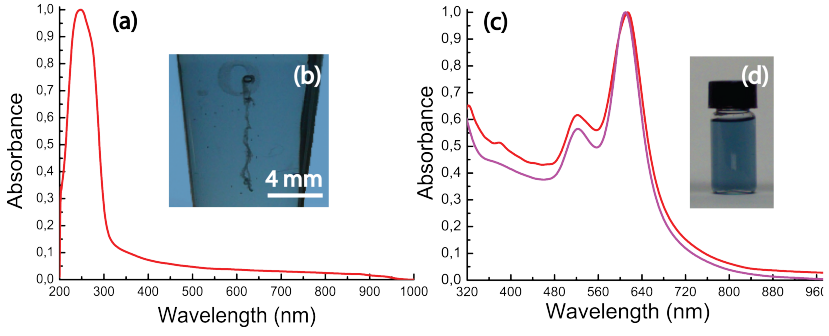

FIGURE 4.1: Normalized UV–vis absorption spectrum of the DNA solution (a), along with the polarized spectrum (c) of the GNRs aqueous dispersion (d), acquired for two orthogonal polarizations. (b) is a view of the double helix *visible mass*.

Figure 4.1a shows the normalized UV–vis absorption spectrum of the DNA sample suspended in a rehydration solution (tris-EDTA buffer); the solution appears transparent, showing an absorption signal only close to the 270nm wavelength. This spectral feature can be accounted for by considering that DNA is formed by simple units (called nucleotides), each composed of a sugar group, a phosphate group, and a nucleobase (i.e., guanine, adenine, thymine, and cytosine [76]) with slightly different, characteristic, absorption spectra in the UV range (from 250–290nm). Moreover, since, the DNA has been thoroughly purified during the extraction process, the residual presence of proteins (which usually show an absorption peak between 275 and 280nm) is negligible, so that the contribution of proteins to the absorption peak can be disregarded. Therefore, the absorption peak reported in figure 4.1a and centered at 270nm just corresponds to the convolution of the absorption bands of the nucleobase. Figure 4.1b is a view of the double helix visible mass observed during the DNA extraction process. Water dispersible, cetyltrimethylammonium bromide (CTAB) capped GNRs have been synthesized by suitably modifying an already reported, seed mediated protocol, described in detail by Placido et al. [77]. The dispersion of GNRs, with aspect ratio 2.5 ± 0.4, exhibits two typical plasmon bands: a transverse one at wavelength $\lambda = 520\,nm$ and a longitudinal one at $\lambda = 635\,nm$.

4.4 Characterization of GNRs DNA composites

The optical response of GNRs has been analyzed for two orthogonal polarizations of the impinging probe light. As shown in figure 4.1c, the spectroscopic features exhibit no significant dependence on the polarization direction; such experimental evidence confirms that GNRs are randomly distributed, resulting in an isotropic solution where no macroscopic order can be recognized. Homogeneous mixtures of DNA and GNRs have been prepared by adding an aliquot of the GNRs solution $(2 \times 10^{-9} M)$ in the dispersion of DNA, the GNRs concentration ranging from 2% to 50% in weight. A preliminary investigation of the interaction between GNRs and DNA has been carried out by performing a gel electrophoresis analysis, a technique particularly suited to accomplish both separation and analysis of macromolecules (e.g., DNA, RNA, proteins) and their fragments, based on their length and charge [78]. Charged molecules of the solution to be tested are forced to move through an agarose matrix under the influence of an electric field that is created by applying an external DC voltage. The DNA molecules, being

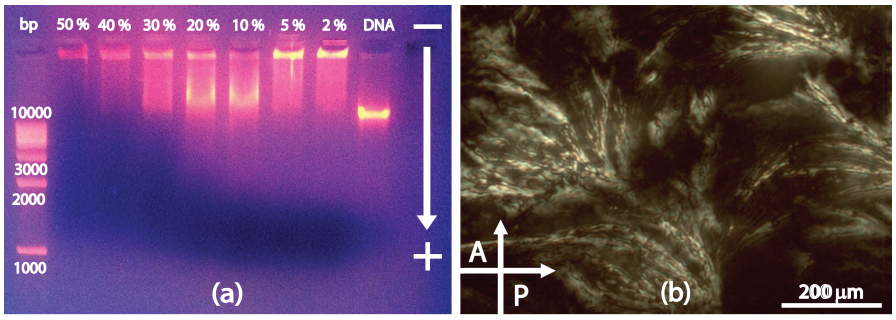

FIGURE 4.2: Gel electrophoresis analysis for different GNRs concentrations (a), along with the POM view of the DNA-GNR mixture deposited on a glass substrate by drop casting (b).

negatively charged along their length, migrate toward the positive electrode. In this way, during their electrophoretic run, they are separated according to their length, since pores in the agarose matrix allow short DNA molecules to snake through more easily than long ones. The mixture of DNA and GNRs has been then added of a small amount (1% in weight) of a negatively charged blue dye (ethidium bromide, EtBr), which is an intercalating agent commonly used to act as a fluorescent tag; when EtBr is exposed to UV light, its orange fluorescence increases of about 20-fold upon binding to DNA. At a later stage, the obtained solution has been pipetted in the agarose matrix molded with wells (figure 4.2a), also containing DNA filaments of known size (in the first well on the left of figure 4.2a), which are used as markers. The agarose matrix is then placed on a UV lamp and covered with a UV glass filter. When the system power supply is turned on, the DC voltage ($120\,V$, $0.78\,mA$) induces a migration of the pure DNA (figure 4.2a, second well on the right) towards the positive electrode. Observation of a single fluorescent band indicates that DNA molecules have almost the same length, which includes approximately 10000 base pairs. By increasing the GNRs concentration up to 5%, the solution shows a remarkable fluorescence very close to the well, pointing out an inhibited migration toward the positive electrode. Such evidence can be accounted for by considering the presence of the CTAB bilayer, which makes GNRs positively charged, and thus able to electrostatically interact with the DNA molecules without affecting their average length, but varying the effective charge of the whole system. By increasing the GNRs concentration up to 20%, the fluorescence light appears as split and coming from two main sites: a first one, closer to the well, reasonably ascribable to the electrostatic conjugation between GNRs and DNA, and a second one, at about a 10k base pairs distance, which is due to the excess of DNA, not electrostatically conjugated to GNRs, and hence more mobile. For concentrations of GNRs exceeding 20%, the heavy GNRs damage the DNA strands (when the value is about 30–40%), also affecting its mobility (for values

$\approx 50\%$). For a further characterization, a polarized optical microscope (POM) analysis has been also performed. Preliminary observations confirm that a liquid crystalline phase of the DNA molecules exists and is maintained up to 20% of GNR concentration; by exceeding this value, the large quantity of GNRs strongly affects the liquid crystalline structure of the DNA and the entire solution becomes isotropic. Therefore, in the following experiments, a solution with 20% of GNR has been used to both maximize the presence of GNRs and keep the DNA in a liquid crystalline phase, avoiding to damage it. A droplet of this solution has been drop-cast onto an untreated glass substrate and allowed to dry under controlled temperature ($45°C$); meanwhile, a stretching of the droplet on the surface, along a preferred direction, has been induced by means of an airflow, thus obtaining a quite thin and uniform film of large area ($\approx 1mm^2$). Figure 4.2b shows a POM view of this film, acquired at room temperature, after evaporating all the solvent. At this level of magnification, details on the local organization of the GNRs around the filaments of DNA cannot be seen and they appear oriented, in average, along the shearing direction. The bright strips, clearly visible in figure 4.2b, confirm that the DNA exhibits a LC phase, with a local birefringence of about 0.01 (measured by the optical compensator method). This value of birefringence, lower than typical values (~ 0.2) obtained in very well ordered LC phases, can be attributed to the low initial concentration of DNA in the aqueous solution; indeed, it has been already shown that, in the investigated concentration range, the hydrated DNA exhibits a pre-cholesteric phase, whose typical birefringence is of the order of 10^{-2} [79]. It is also worth pointing out that the DNA birefringence has been experimentally demonstrated to be only weakly perturbed by GNR concentrations up to 20%. A transmission electron microscopy

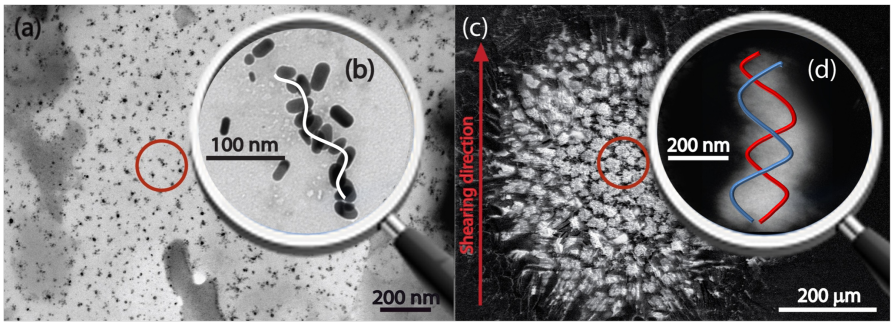

FIGURE 4.3: TEM (a) and ESEM (c) images of the sample along with their high magnification (b), (d), highlighting the 'helix like' organization (tracked with continue arrows) of GNRs wrapping the liquid crystalline DNA.

(TEM, by Jeol JEM microscope, operating at $100kV$) analysis has been performed by depositing a droplet of the same solution onto a carbon-coated copper grid, and allowing then the solvent to

evaporate. Figure 4.3a is a low magnification TEM image of the sample, whereas a high magnification of the area marked with the red circle in figure 4.3a is reported in figure 4.3b. Here, the GNRs seem to be organized in a helical geometry (tracked with continue arrows), while there is no relevant information about the DNA component. Both features can be accounted for by considering that: i) gold atoms have a high atomic number ($Z \approx 79$), hence they give rise to a high signal contrast, due to a higher scattering power if compared to the DNA components (nitrogen, carbon and phosphorus based system with an average $Z \approx 12$); and ii) due to the high energy of the impinging electron beam (100 KeV), the DNA can easily evaporate. For these reasons, the DNA presence can be hardly observed in figures 4.3a,b, apart from some residual white spots that are visible close to the GNRs. It is worth noting that, while different information on the DNA GNRs composite, useful for other application-oriented investigations (e.g., gene therapy), have been already obtained by using different techniques (such as negative staining [80] and cryo-electron microscopy [81]), the helical geometry, recognizable in figure 4.3b, which indicates a nanoscale organization of the GNRs, represents the most important aspect of our findings. For this reason, a further investigation of this assembly geometry has been carried out by Environmental Scanning Electronic Microscopy (ESEM, Quanta 400 FEG by FEI, operating at $25\,kV$) analysis of the same sample area reported in figure 4.2b. Figure 4.3c is a low magnification ESEM image of the sample, whereas figure 4.3d shows a high magnification of the area marked with the red circle in figure 4.3c, and highlights a long-range distribution of densely packed GNRs, which, also in this case, appear to be organized in a helical geometry wrapping the liquid crystalline DNA. Furthermore, we have performed a far field, polarized, spectral analysis of the same sample area (figure 4.3b) by utilizing white light (wavelengths in the range $450 - 810\,nm$, impinging on the sample at normal incidence). Figure 4.4a shows the absorption spectra of the sample for light linearly polarized i) along the shearing direction, ii) perpendicularly to it, and iii) at 45° (indicated in figure 4.4b with red, blue, and green arrows, respectively). Since GNRs that embed the DNA filaments are, in average, oriented along the shearing direction, light polarized in this direction experiences only the longitudinal plasmon response, as it is clear from figure 4.4a (red curve), whereas the transversal band is, in this case, completely missing. In addition, this spectroscopic response shows a small bump at $\lambda \approx 800\,nm$, which is ascribable to inter-particle interaction phenomena between close-packed GNRs [82]; this represents a further evidence of the macroscopic organization of GNRs along the shearing

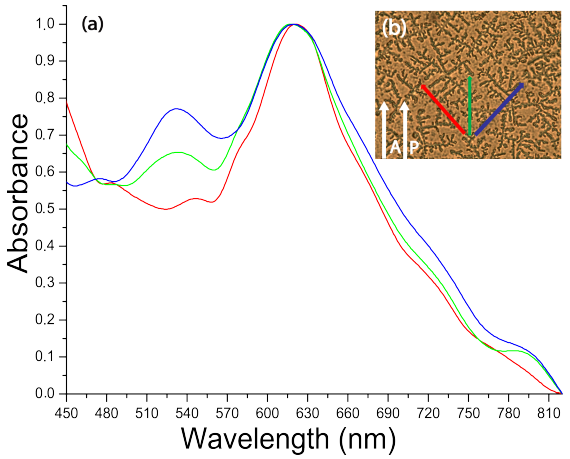

FIGURE 4.4: Polarized spectral response of the sample (a), along with an optical micrograph (b) of the analyzed area.

direction, induced by the liquid crystalline phase of the DNA. Above considerations are supported by the spectral features exhibited by the same sample when probed with light polarized perpendicularly to the shearing direction (figure 4.4a, blue curve): in this case, the transversal band is well evident, whereas the amplitude of the longitudinal band is reduced of about a factor two. In fact, in these experimental conditions, the longitudinal band cannot be suppressed completely, being evident from the ESEM analysis (figure 4.3d) that GNRs undergo a rotation along the main axis of the helical geometry. Finally, in the spectral response to light polarized at 45° with respect to the shearing direction (figure 4.4a, green curve), both plasmonic bands are observed, with amplitudes that are in between the ones of the two previously described cases, as expected on the basis of above considerations. Such spectral evidence confirms the TEM and ESEM analysis, showing that GNRs follow the rotation along the main axis of the helical geometry.

Chapter 5

Thermo-plasmonics: generation of heat from metallic nanoparticles

5.1 Introduction

In this chapter the physics of plasmonic heating is studied by starting from the mechanism energy convertion from light to heat. Then, the heat transfer from nano-particles to the surrounding medium is explained. Next, a fast and simple experimental approach to monitor temperature variations of a huge number of NPs randomly distributed is described. Finally, a model to predict temperature variations on this kind of system is presented.

5.2 Physics of plasmonic heating

Thermo-plasmonics is one of the most emerging and fastest growing research fields of the recent years [14, 85–87]. Based on the used of noble metal nanoparticles (NPs) to control temperature at the nanoscale, thermo-plasmonics exploitis the localized surface plasmon resonance (LSPR), which occurs when the conduction electrons of NPs oscillate in resonance with the electric field of an impinging light, thus producing a photo-induced heating process of the entire nanostructure. LSPR represents the way to input energy in such small nano-objects [88–90](NPs): Absorbed light induces an unavoidable damping of the LSPR and generates a non-equilibrium

electron distribution that decays via electron-electron collisions [91]. The hot electron gas equilibrates with lattice phonons which transfer the generated energy to the surrounding medium, resulting in heat generation by a Joule mechanism [17, 92, 93]. This heat generation increases the temperature inside the object and places the system out of equilibrium. The temperature of the enviroment is thus increased to reach a new equilibrium.

To explore the process of the photo-induced heating we consider a metallic nanoparticle surrounded by air and illuminated by a monochromatic light characterized by a wavelength λ. Let $\mathbf{E}(\mathbf{r},t) = Re\{\mathbf{E}(\mathbf{r})e^{-i\omega t}\}$ be the electric field and $\mathbf{E}(\mathbf{r})$ its complex amplitude. Let $\mathbf{j}(\mathbf{r})$ be the complex amplitude of the electronic current density inside the particle. The heat density source $\bar{q} \equiv < q(\mathbf{r},t) >_t$ inside the nanoparticle, arising from Joule effect, is [94]:

$$\bar{q}(\mathbf{r}) = < \mathbf{j}(\mathbf{r},t) \cdot \mathbf{E}(\mathbf{r},t) >_t \tag{5.1}$$

$$\bar{q}(\mathbf{r}) = \frac{1}{2} Re[\mathbf{j}(\mathbf{r})^* \cdot \mathbf{E}(\mathbf{r})] \tag{5.2}$$

By using the relations $\mathbf{j}(\mathbf{r}) = -i\omega\mathbf{P}(\mathbf{r})$ and $\mathbf{P}(\mathbf{r}) = (\varepsilon_m - \varepsilon_0)\mathbf{E}(\mathbf{r})$, equation 5.2 can be rewritten as:

$$\bar{q}(\mathbf{r}) = \frac{\omega}{2} Im(\varepsilon_m) |\mathbf{E}(\mathbf{r})|^2 \tag{5.3}$$

where ε_m is the metal permittivity. The heat density source $\bar{q}(\mathbf{r})$ results to be proportional to the square of the electric field inside the nanoparticle. The total heat power delivered by the metal nanoparticle is obtained by integrating the heat density source on the volume V of the nanoparticle:

$$Q = \frac{\omega}{2} Im(\varepsilon_m) \int_V |\mathbf{E}(\mathbf{r})|^2 \tag{5.4}$$

An alternative, analytical approach, to estimate the heat power Q absorbed (or delivered) by a NP, used in the case of nanoparticles with geometries like spheres and rods, is based on the use of the absorption cross section σ_{abs}, introduced in chapter 1:

$$Q = \sigma_{abs} I \tag{5.5}$$

where I is the irradiance of the incoming light (W/cm^2, in the case of a plane wave $I = n_s c_0 \varepsilon_0 |\mathbf{Er}|^2/2$).

Once the heat power density originating from the Joule effect is determined, we can introduce it into the general equations that govern heat diffusion in the surrounding environment; this two step analysis for calculating the temperature increase is justified by the circumstance that heat generation inside the NP is much faster (ps) than its release into the environment ($ns - \mu s$) (see section 5.2.1). The differential equation governing the heat diffusion is:

$$\rho(\mathbf{r}) c_p(\mathbf{r}) \partial_t T(\mathbf{r},t) - \nabla \cdot (\kappa(\mathbf{r}) \nabla T(\mathbf{r},t)) = q((\mathbf{r}),t) \tag{5.6}$$

where κ is the thermal conductivity, ρ the mass density, c_p the heat capacity and T the temperature. For these kind of systems we can consider that the thermal conductivity, the heat capacity and mass density are constant within the medium:

$$\rho c_p \partial_t T(\mathbf{r},t) - \kappa \nabla^2 T((\mathbf{r}),t)) = q((\mathbf{r}),t) \tag{5.7}$$

In the steady state regime the heat diffusion equation becomes the Poisson equation:

$$\kappa \nabla^2 T(\mathbf{r}) = -\bar{q}(\mathbf{r}) \tag{5.8}$$

The profile of the heat density generation $\bar{q}(\mathbf{r})$ can be highly non-uniform inside a plasmonic structure. However its internal temperature profile remains quasi-uniform due to the much higher thermal conductivity of metals compared with the surrounding media (air, water, glass,and so on) [95]. Since the source of heat in the system is restricted to the plasmonic structure, the equation governing heat diffusion in the surroundings becomes a Laplace equation:

$$\nabla^2 T(\mathbf{r}) = 0 \tag{5.9}$$

Solving this equation dictates that outside the plasmonic structure, the temperature features a $1/r$ decrease [95]. Interestingly, equation 5.9 does not present any length related constant, like the wavelength in Maxwell's equations for instance. The direct consequence is that the related temperature profile does not depend on the size of the structure: around a plasmonic nanoparticle of typical dimension $\tilde{L}$, the temperature expands over approximatively $\tilde{L}$, whatever the nanoparticle temperature increasis. Although the temperature profile is fixed, the absolute temperature increase can be controlled. To this end, different parameters have to be considered [95]:

- the absorption cross section of the nanoparticle;
- its morphology: the heat dissipation is favored in elongated or small particles since the surface to volume ratio is increased; this leads to lower temperatures;
- the environment: the higher its thermal conductivity, the lower the temperature values;
- the power of the impinging light (laser).

For a spherical particle, the calculation of the nanoparticle temperature increase ΔT_0 is straightforward and yields a useful analytical formula [95]:

$$\Delta T_0 = \frac{\sigma_{abs} I}{4\pi\kappa R} \tag{5.10}$$

where I is the irradiance of the incoming light and R the radius of the sphere. As an example, to obtain a temperature increase of $1°C$ in a $R = 25\,nm$ spherical nanoparticle in water illuminated at the plasmonic resonance ($530\,nm$), the required laser intensity is $3.8 \cdot 10^3 W/cm^2$. For the more general case where the nanoparticle is not spherical, a correction factor to formula 5.10 is available [95].

5.2.1 The dynamics of the photo-induced heating

In order to understand the dynamics of the photo-induced heat and its delivery in the surrounding medium we can consider the NP impulse response, as it is typical for dynamic systems in physics. Let'us image that a "very short" light pulse is sent onto a gold nanoparticle (see Fig.

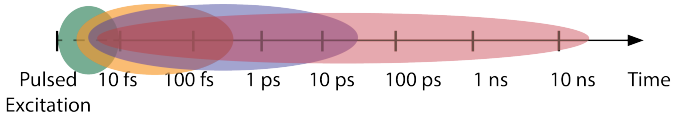

FIGURE 5.1: Schematic illustration of the series of energy exchanges involved in the optical impulse response of a gold nanoparticle on a logarithmic time scale.

5.1). Part of the incoming light is then absorbed by the induced electron transitions; *a priori* it is possible to induce any interband transitions, as well as intraband ones. In the former case, photons generate individual electron-hole pairs, while in the latter they promote electrons up to higher levels within the conduction band. We have already seen in a previous section (chapter 1) that in spherical Au-NPs both plasmon resonance and interband transitions can be excited in the same spectral range. In this latter case the SPR is damped and broadened due to Landau damping. Beyond this, for the sake of simplicity, we will disregard the possible excitation of interband transitions in the description of the dynamics mechanisms.

Provided the ultrashort wave packet spectrum matches the SPR energy, the plasmon resonance is excited, that is, a resonant coupling with the electromagnetic wave induces a coherent set of in-phase electron excitations in the conduction band. It has been shown through optical experiments (using second-harmonic generation autocorrelation, spectral hole burning or measurements of the SPR bandwidth of single NPs) that the dephasing time (T_2) of the SPR is a few femtoseconds. The NP is then left with an extra energy stored in the electron gas. As a matter of fact, a few electrons have gained photon energy by absorption, the other ones remaining in the non-excited states; this puts the electron distribution out of equilibrium. Energy is then redistributed among the whole quasi-free electron gas by electron-electron collisions, leading to the recovery of an internal thermal equilibrium within the conduction band. This process occurs on a time scale which ranges from a few tens to several hundreds of femtoseconds, depending mainly on the initial energy input (the higher the proportion of excited electrons in the gas the faster the energy redistribution by collisions). At the same time, electrons scatter with phonons. Actually, there are no real collisions with such quasiparticles; rather, a quantized vibration mode of the crystal lattice (i.e. a phonon) induces a modification of the periodic potential experienced by the electrons, and then a modification of the wave function of the latter. The typical time scale of this process is about one picosecond. As for the electron electron (e-e) scattering rate, the actual electron-phonon (e-ph) relaxation time depends on several factors such as particle

size and input energy excess. Finally, as the NP is not isolated but is embedded in a medium, there is a thermal energy exchange at the interface through phonon-phonon collisions, leading to the cooling down of the NP. The dynamics of this process may range from a few picoseconds to nanoseconds. As a consequence of this series of energy exchanges, the internal energy of the electron gas that follows the light pulse absorption undergoes (i) a sudden and strong rise, (ii) an inner redistribution within the electron gas (a thermal regime), (iii) a fast decrease (e ph scattering) and (iv) a slow return back to equilibrium (thermal transfer to the host medium). The particle temperature is ruled by the balance between the gain of energy from e-ph collisions and the heat release towards the host medium. It presents then an increase on a picosecond time scale followed by a slow decrease.

5.3 Experimental study of the heat generation from random distribution of gold nanoparticles

In this section it is presented an experimental analysis of the photo-induced heat that can be realized in a planar layer of randomly distributed GNPs, with two different values of surface density. The idea is to monitor temperature variations inside the area illuminated by a continuous laser radiation at the NPs resonance wavelength and investigate the phenomenon by considering a high density of NPs fixed on a given substrate. Measurements have been performed by means of a thermographic camera able to detect localized temperature variations with a resolution in non-contact mode. The use of this method is dictated by the macroscopic temperature variations induced by the huge number of NPs contained in the illuminated area; a statistical analysis based on scanning electron microscopy (SEM) images enabled to estimate this number to be around 10^{10}, responsible of temperature variations of tens of $^{\circ}C$. Experiments have been performed on monolayers of GNPs with two different values of surface density. GNPs are synthesized by following the Turkevich method [96]. They result to be attached on a glass substrate, that has been functionalized with a strong oxidizing agent (Piranha solution), after dipping the substrate into a gold colloidal solution at room temperature (Fig. 5.2a).

The electrostatic interaction between the negative charged NPs and the functionalized surface

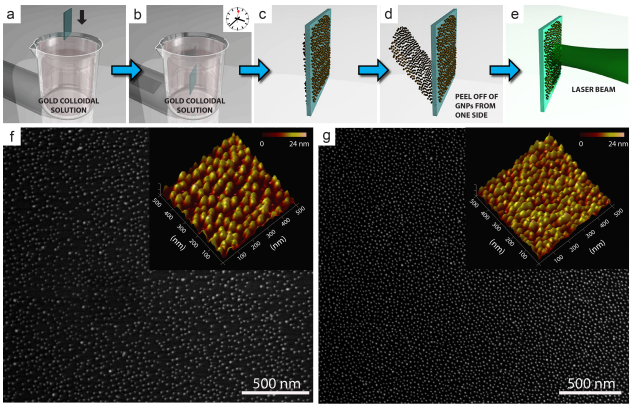

FIGURE 5.2: Sketch of the samples preparation and probing: samples were immersed in a gold colloidal solution (a), for two specific time depending on the selected surface density (b); samples were characterized by the presence of NPs on both sides (c); NPs are removed from one side (d) and then the photo-heating is induced by means of a green beam laser (e). SEM images of GNPs distributed on glass substrates with two different values of surface density: (a) sample 1, surface density of 355 μm^{-2} and (b) sample 2, with surface density of 701 μm^{-2}. Insets are the 3D view AFM images of the same samples.

enables to obtain a strong adhesion. The procedure is repeated twice by changing the functionalization time from 50 minutes to 1 hour and 45 minutes (Fig. 5.2b), in order to obtain two samples with two different values of NP surface density; it is worth noting that obtained samples are characterized by the presence of NPs on both sides of the substrate (Fig. 5.2c). A spectral analysis shows the typical LSPR absorption of spherical NPs in the green region of the spectrum, centered at 515 nm for both samples; as expected, after removing the NPs from one side of the two substrates (Fig. 5.2d), a decrease of approximately 50% in the resonance peak occurs. Scanning Electron Microscopy (SEM) and Atomic Force Microscopy (AFM) images reported in Fig. 5.2 reveal well-dispersed GNPs randomly distributed on the entire surface of both samples. Average size, polidispersivity and surface density of NPs have been evaluated by means of a statistical analysis performed by means of a Java-based software (ImageJ).

Sample 1 (S1) exhibits a polidispersivity of 18.78%, an average NP diameter of 20.4 nm and a surface density of about 355 μm^{-2}; sample 2 (S2) is characterized by a polidispersivity of 6.02%, an average diameter of 19.6 nm and a surface density of about 701 μm^{-2}, both values evaluated by performing an average of data belonging to different areas of the two substrates. AFM images (insets of Fig. 5.2) show an average height of NPs of approximately $(20 \pm 3) nm$.

S1 and S2 are illuminated by a continuous green laser at $\lambda = 532\,nm$ (Fig. 5.2e), with a spot size of 0.21 cm^2. Measurements are made at power intervals of 50 mW in the range $10 - 250\,mW$, corresponding to intensity variations from 0.05 to 1.19 W/cm^2. A thermographic analysis has

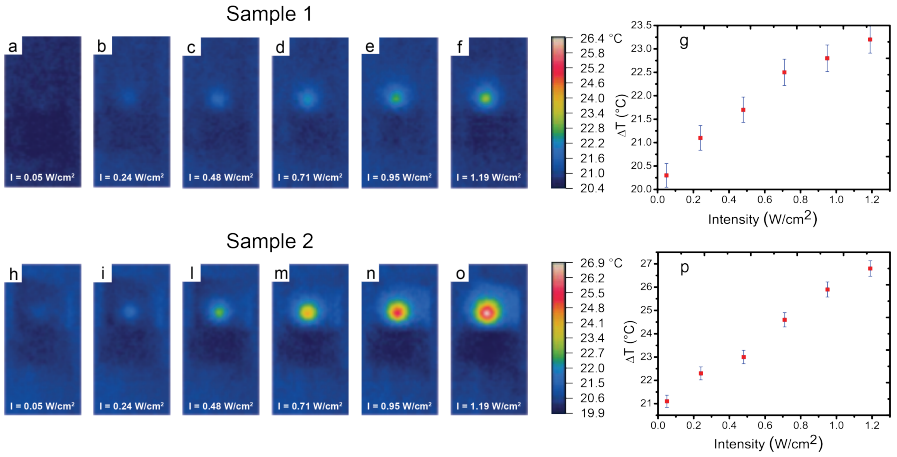

FIGURE 5.3: Thermographic images of sample 1 (a,f) and 2 (a,f), for different values of the pump beam intensity.

been performed at a small angle with the pump beam (that impinges perpendicularly to the sample) by using a thermo camera (E40 by FLIR) characterized by a sensitivity of $0.07°C$ and a spatial resolution of $2.72 mrad$. Control-parameters have been appropriately set to consider both environment and materials properties.

Thermal images for S1 and S2 are reported in Fig. 5.3. Figures 5.3a - 5.3f related to sample S1 represent the thermographic analysis for six different values of excitation intensity, whereas Fig. 5.3h - 5.3o refer to S2. Both set of images present *hot-spots*, related to the photo-induced heat generated by the GNPs, in resonance with the external laser excitation. For both samples, the scale of the thermo camera is properly set in order to appreciate temperature changes in the range of values $19.9 - 26.9°C$. By monitoring temperature values of the central pixel of each *hot - spot*, corresponding to the highest temperature value, it is possible to plot the temperature variation $\Delta T = T - T_0$ as a function of the impinging intensity (see Fig. 5.3g for S1 and Fig. 5.3p for S2); a linear increase is observed in both samples. The measured temperature variation for S1 is $3.0 \pm 0.4°C$, while for S2 it is $6.0 \pm 0.4°C$. We recall here that the surface density of S1 is about half of S2, resulting in a linear increase of ΔT as a function of the density of GNPs. Same values of ΔT were detected by monitoring different areas of the same sample. In order to verify the stability of GNPs on the substrate, samples have been tested with high incident intensity, corresponding to a ΔT of about $40°C$. Morphological analysis shows that the distribution of the NPs is not affected by this procedure.

A further investigation is related to the possibility of controlling ΔT by changing the refractive

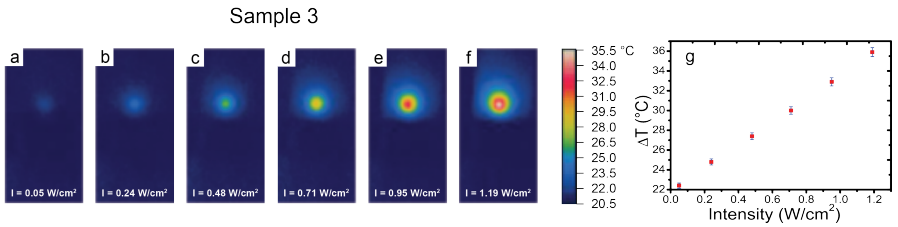

FIGURE 5.4: Thermographic images for different values of intensity of the pump beam for sample 3, with a polymer as surrounding medium.

index of the NPs surrounding medium [97, 98]. A polymer (PAAD-22 synthesized by BeamCo) is spin-coated onto sample S1 at 1000 rpm for 30s. The thickness of the deposited polymer layer is evaluated by means of an AFM analysis, resulting approximately equal to $(20 \pm 3)\,nm$. The obtained sample is labelled as S3. A UV-VIS spectrum analysis of S3 shows a red-shift of about $12\,nm$ of the peak wavelength and an increase of the overall extinction value of the LSPR of about $78\,\%$. *Thermal-images* for S3 related to the same six excitation intensities used for S1 and S2 are reported in Fig. 5.4a to 5.4f, where the scale is set in the range $20.5\,^{\circ}C - 35.5\,^{\circ}C$, in order to include also the highest temperature variation measured in this case; once again, results confirm a linear dependence of ΔT on the excitation intensity (see Fig. 5.4g), but with a different slope: The increase of the refractive index of the host material surrounding GNPs, (with the same surface density considered in S1, $355\,\mu m^{-2}$), causes a higher photo-induced heat, corresponding to ΔT values of about $15 \pm 0.4\,^{\circ}C$.

5.4 Theoretical prediction of the heat generation from random distribution of gold nanoparticles

In a growing number of recent papers on thermal plasmonics, collective effects are taken into account, since the contribution of a single GNP has been proved to be not enough to explain temperature variations observed in some experimental configurations [99, 100].

Up to now, theoretical efforts to describe this collective thermal response consist in numerical modeling of periodic and quasi-periodic arrays of metal NPs [101, 102], or in the description of a water droplet containing a colloidal suspension of a high number of GNPs [99].

Here it is presented a quite different system: on one side, NPs are randomly distributed, so that it is impossible to invoke any periodicity to reduce the study to a single lattice unit cell

investigation; on the other hand, we deal with a fixed 2 dimensional structure, which simplifies the study when compared to a suspension in a water droplet, where complex mechanisms related to convection have to be taken into account.

The sample under study is made, indeed, of a huge number of GNPs randomly distributed on a glass substrate. Both SEM and AFM analysis have shown that the distribution of GNPs is homogeneous, and it is possible to experimentally evaluate the main parameters to be used in the model, such as NPs density n_{np}, size (i.e. NPs radius R_{np}), inter-particle distance (distance between NPs centers) d, intra-particle distance (distance between NPs surface) D and polydispersivity. Moreover the AFM analysis (see Fig. 5.2) shows that the nanoparticles stick on the substrate without plunging into it, meaning that, when calculating their plasmonic response, it is possible to consider them as completely surrounded by air. It is interesting to observe that, for the denser sample (S2), the number of NPs acted on by the laser beam (spot size $0.21\,cm^2$) is approximately 1.4×10^{10}. To address the theoretical problem of the collective heating effect of GNPs randomly distributed on a given substrate, with a surrounding medium, the heating effect on a single GNP has been considered; then, the contribution of all the involved NPs at different distances from a fixed point has been calculated by simply adding the contributions of all simple GNPs.

In the absence of phase transitions of the surrounding medium, in order to predict the temperature around a single GNP it is necessary to solve the heat transfer equation (Eq.5.6), which derives from an energy balance: the net rate of thermal energy that comes out from a single GNP, plus the rate of thermal energy that accumulates inside (internal energy variation in the GNP) must equal the net rate of thermal energy generation.

At thermal equilibrium, the solution of Eq. (5.6) is obtained by taking into account a heat production Q at a constant rate per unit time and per unit volume inside the spherical NP (distance $0 \leq r \leq R_{NP}$ and conductivity K_0), while in the region $r > R_{NP}$ the conductivity of the host medium is K_H and no heat production occurs [103]. Calculations yield a temperature variation, at a fixed distance r from a NP, given by

$$\Delta T(r) = \frac{QR_{NP}^3}{3rK_H} \tag{5.11}$$

where, according to Joule effect, the thermal energy generation Q is given by:

$$Q = \frac{\varepsilon_0 \omega \, Im(\chi_{NP}) \, |\mathbf{E}_{int}|^2}{2} \tag{5.12}$$

Due to the huge number of GNPs and their homogeneous distribution, we can treat them in the way stars of the Universe are taken into account to calculate their contribution to the brightness of the sky when solving Olbers' paradox, known in astronomy [104]. If we distribute homogeneously our GNPs in concentric rings with radius r, spaced by an inter-particle distance d, we are able to place all of them (estimated to be about 1.4×10^{10}) onto the surface of interest (laser spot size of $0.21\,cm^2$) by putting in each ring a number of NPs equal to $N(r) = 2\pi r/d$. Since the temperature variation provided by relation (5.11) for a single GNP goes down as $1/r$ we find that the contribution of all NPs is proportional to $N(r) \times \Delta T(r) = 2\pi Q R_{NP}^3/3dK_H$, not depending on the distance r. Then, like in Olbers' paradox, where all stars, even the most distant, contribute equally to the sky brightness, in our case also GNPs that are very distant from the center of the laser spot give a significant contribution to the temperature variation of the sample, because the number of GNPs at a given distance r grows linearly with distance. Thus, all nanoparticles invested by the laser beam must be considered in the calculation of the final ΔT.

We note that, since the intra-particle distance D between GNPs is always greater than the nanoparticles radius, we can assume that the plasmonic field due to the photo-induced absorption is not affected by coupling effects between GNPs [105–107].

Then, we consider a high number of heat nano-sources positioned at different positions $\mathbf{r_i}$ from a point $\mathbf{r}$, each contributing to Eq. (5.6) by a quantity $Q_i(\mathbf{r_i})$. In this way the right side of Eq. (5.6) becomes $Q(\mathbf{r}) = \sum_i Q_i(\mathbf{r_i})$ and possible solutions will be of the type:

$$\Delta T(\mathbf{r}) = \sum_i \Delta T_i(\mathbf{r_i}) = \sum_i \frac{c(\lambda) \, I(\mathbf{r_i})}{|\mathbf{r} - \mathbf{r_i}|} \tag{5.13}$$

where

$$c(\lambda) = \frac{V_{NP} Im(\chi_{NP})}{2\lambda K_H \sqrt{\varepsilon_H}} \left| \frac{3\varepsilon_H}{2\varepsilon_H + \varepsilon_{NP}} \right|^2, \tag{5.14}$$

i indicates the i-th GNP placed at a position $\mathbf{r_i}$ distant $|\mathbf{r} - \mathbf{r_i}|$ to the point $\mathbf{r}$ where we are interested to calculate the temperature variation ΔT, V_{NP} is the GNP volume, ε_H, ε_{NP} are the dielectric permittivity of host medium and GNP, respectively. Relation (5.13) is a solution of

Eq. (5.6), that in a three dimensional problem is equivalent to a solution of the Poisson equation in electrostatics [99]. Furthemore, as reported in Olber's paradox solution, the huge number of NPs and their homogeneous distribution enable to treat this system in the framework of the "continuum" approximation. In the same way, we are able to obtain an equivalent expression for our bi-dimensional case by using the "continuum" approximation:

$$\Delta T(\mathbf{r}) = \iint \frac{\sigma(\mathbf{r}')d^2\mathbf{r}'}{|\mathbf{r}-\mathbf{r}'|}. \tag{5.15}$$

where we consider a cilindrical beam with intensity I_0 and transversal section of radius w to write

$$\sigma(\mathbf{r}') = \sigma = c(\lambda)I_0 n_{NP} \tag{5.16}$$

and

$$\Delta T(r=0) = 2\pi\sigma w = 2\pi w c(\lambda) n_{NP} I_0. \tag{5.17}$$

This simple linear relation enables to determine the temperature change at $r = 0$ as a function of the laser beam intensity, due to a huge number of metal NPs, distributed onto a given substrate in a random way. All parameters included in $c(\lambda)$ (Eq. (5.14)) are known from experimental analysis, whereas the only one that must be determined is the thermal conductivity K_H of the host medium, seen as a combination of the substrate with the surrounding medium. Indeed, it is reasonable to assume that the heat flow occurs not only through the surrounding medium of GNPs, but also through the glass substrate. As reported in the experimental section, our thermographic analysis allowed to measure temperature values on the entire area reached by the laser beam, demonstrating a linear dependence of ΔT on the impinging light intensity. This allows to obtain K_H from a simple inverse relation in which the angular coefficient of ΔT versus intensity I_0 is calculated.

5.4.1 Numerical simulations.

In order to validate our theoretical model, we have performed two different numerical simulations. Assuming that in a give point of the substrate the contribution of each NP can be added to the one of all the others ($\Delta T(\mathbf{r}) = \sum_i \Delta T_i(\mathbf{r_i})$), we calculate the total contribution of 1.4×10^{10} nanoparticles at the center of the system in two different ways: the first one provides ΔT values

in the center of a circular distribution of GNPs, as already introduced in Olbers'like treatment; the second one takes into account a homogeneous, random, distribution of GNPs. In both cases, predicted values turn out to be the same, and in good agreement with experimental data.

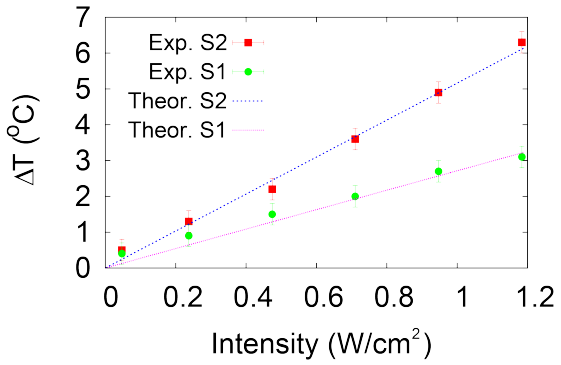

FIGURE 5.5: Red and green points represent experimental values of temperature variation ΔT for the two samples S1 and S2 obtained with thermocamera looking at the center of laser spot; magenta and blu lines represent the corresponding numerical simulations, performed by assuming $K_H = 0.12 W/(^oK\,m)$

In Fig. 5.5 experimental values of temperature variations as a function of excitation light intensity for the two samples S1 and S2 are reported, along with the corresponding numerical simulations (magenta and blue lines), performed by using a value for K_H given by $K_H = 0.12 W/(K\,m)$. We got K_H by fitting experimental values $\Delta T(I)$ for sample S2; then, we used the derived value to carry out numerical simulations for the two distributions with surface densities of both samples S1 and S2. This procedure allow to validate our theoretical model, based on the summation of all the single contributions at different distances, calculated with the same value of K_H; is worth noting that this value of thermal conductivity is in-between the well known air and glass ones.

A numerical approach has been performed also for the thermal response of sample S3, obtained by spincoating a polymer layer on the surface of S1.

The map of Fig. 5.6 represents the temperature variation ΔT as a function of impinging wavelength λ and light intensity I related to S3. In Fig. 5.6 the main results of studies on the sample S3 are reported. Inset of Fig. 5.6 contains experimental values of ΔT (red points), along with a numerical simulation (green line) carried out on the same sample, extracted as a vertical cut at $\lambda = 532\,nm$ from the map (dashed black line). Also in this case, we derived K_H by performing a best fit of experimental data, obtaining the value $K_H = 0.36 W/(K\,m)$.

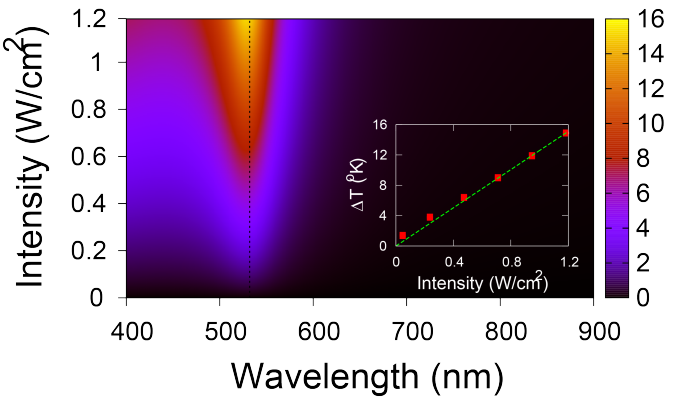

FIGURE 5.6: The map represents the temperature variation ΔT as a function of wavelength λ and intensity I of the impinging light, calculated for sample S3 by using the value $K_H = 0.36 W/(K m)$. The green line in the inset corresponds to a vertical cut at $\lambda = 532 nm$ (dashed line in the map). Red points are the corresponding experimental values of ΔT.

The good agreement is confirmed by comparing the theoretical extinction cross section $C_{ext} = kIm(\alpha)$ (where k is the wave vector) and the extinction spectrum, obtained by performing a spectrophotometer analysis on S3.

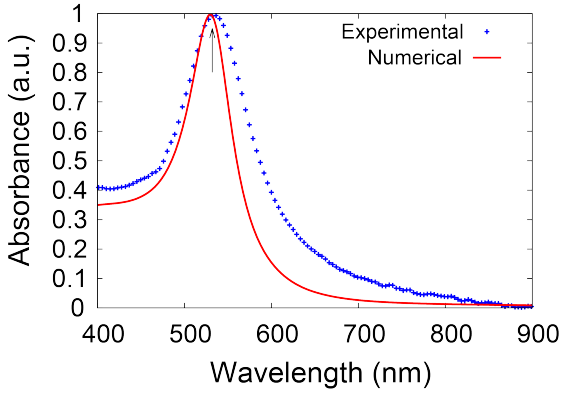

FIGURE 5.7: Comparison between the normalized imaginary part of polarizability α and extinction cross section measured on sample S3, versus light wavelength λ. The black arrow point out the wavelength $\lambda = 532 nm$, used in the experiment.

The two curves reported in Fig. 5.7 show a good overlapping between measured data (blue crosses) and numerical analysis. The black arrow indicates the position of the wavelength $\lambda = 532 nm$, which is the one used both for the experimental observation and the theoretical modelling reported in Fig. 5.5. Even if the electric permittivity of GNPs, obtained by ellipsometric measurements performed on a $20nm$ gold layer, was corrected to include the effect of confinement present in a spherical NP, a difference in the bandwidths of Fig. 5.7 is evident. In our opinion, this is a consequence of the strong damping due to the chemical bonds formed

between capping molecules and surface atoms of small colloidal metal nanoparticles [108]; this term, which is not included in our calculation, could fix the observed difference.

5.5 Conclusions

In this chapter we have reported both an experimental study and a theoretical modeling of the plasmonic heat production occurring in a huge quantity of gold nanoparticles (GNPs), homogeneously distributed on a glass substrate and acted on by a green laser light with a Gaussian beam shape. Our detailed investigation allows us to conclude that, in order to explain the observed heating effect, all the GNPs interacting with the impinging light have to be taken into account, since, owing to the homogeneity of GNPs distribution on the substrate, the phenomenon can be well described as due to a collective effect of all the involved nanoparticles. In particular, experiments show a linear dependence of the highest temperature variation (observed in the center of the spotlight) on the intensity of the impinging light; the same linear dependence is predicted by our theoretical (numerical) analysis, where the contribution of each nanoparticle to heat production is simply added to the one of all other GNPs. In fact, if their dimension and inter-particle distance are known along with the refractive index of the surrounding medium, determination (through an experimental fit) of the average thermal conductivity of the whole system (glass substrate + GNPs) allows us to predict temperature variations as a function of light intensity, in good agreement with experimental observations. Our results can be utilized in all those studies of thermal effects in which collective effects have to be taken into account, and the huge number of particles and their spatial distribution do not allow any kind of ”lattice” simplification. Furthermore, our model can be easily extended to a 3D bulk of nanoparticles, thus allowing to further widen its range of applicability.

Chapter 6

Photo-thermal effects in gold nanoparticles dispersed in nematic liquid crystals

6.1 Introduction

The last years have seen a growing interest in the ability of metallic nanoparticles (MNPs) to control temperature at the nanoscale. Under a suitable optical radiation, MNPs feature an enhanced light absorption/scattering, thus turning into an ideal nano-source of heat, remotely controllable by means of light. In this framework, the recent efforts on modeling and characterizing the photo-thermal effects observed in gold nanoparticles (GNPs) dispersed in thermotropic Liquid Crystals (LCs) have been reported. The photo-induced temperature variations in GNPs dispersed in Nematic LCs (NLCs) have been studied by implementing an "ad hoc" theoretical model based on the thermal heating equation applied to an anisotropic medium. Theoretical predictions have been verified by performing photo-heating experiments on a sample containing a small percentage of GNPs dispersed in NLC. Both theory and experiments represent an important achievement in understanding the physics of heat transfer at the nanoscale, with applications ranging from photonics to nanomedicine. In this chapter, a simplified approach to describe the combination of spherical GNPs and NLCs is presented. By exploiting the symmetry of spheres

(GNPs) and the unidirectional order of Nematic LCs (NLCs), a theoretical model and an experimental investigation has been realized to specifically study the heat generation and its transfer mechanism from the photo-heated GNPs to the surrounding medium (NLC).

6.2 Theoretical model of the photo-thermal effects observed in GNPs dispersed in NLC

As seen in the previous chapter in order to predict the temperature around a GNP it is necessary to solve the heat transfer equation (Eq. 5.7), which derives from a balance of heat energy: the net rate of thermal energy that comes out from the GNP, plus the rate of thermal energy accumulation (internal energy variation in the GNP) must equal the net rate of thermal energy generation. At the thermal equilibrium the solution of the Eq. (5.7) is obtained by taking into account a heat production Q at a constant rate per unit time and per unit volume inside the spherical NP (distance $0 \leq r \leq R_{NP}$ and conductivity K_0) while in the region $r > R_{NP}$ the conductivity of the host medium is K_H and no heat production occurs [109]. Calculations yield a temperature variation

$$\Delta T = \frac{QR_{NP}^3}{3rK_H} \tag{6.1}$$

where the thermal energy generation Q is

$$Q = < \mathbf{J}(\mathbf{r},t) \cdot \mathbf{E}(\mathbf{r},t) >_t = \frac{\varepsilon_0 \omega \Im[\chi_{NP}] |\mathbf{E}_{int}|^2}{2} \tag{6.2}$$

and depends on the electric field $\mathbf{E}_{int}$ inside the GNP and on the imaginary part of dielectric permeability $\Im[\chi_{NP}]$ (that describes energy dissipation of the GNP, or dielectric losses); ω is the angular frequency of light and ε_0 is the dielectric permittivity of vacuum.

The Mie theory [18] provides the expression for the electric field $\mathbf{E}_{int}$ inside a spherical GNP. However, in our case the average size of the considered GNPs ($r = 10\,nm$) is much smaller than the used wavelength ($\lambda = 532\,nm$), a circumstance that allows us to use the following quasi-static formula *see Chapter 1*:

$$\mathbf{E}_{int} = \frac{3\varepsilon_H}{2\varepsilon_H + \varepsilon_{NP}} \mathbf{E}_0 \tag{6.3}$$

where ε_{NP} is the dielectric permittivity of the spherical GNP, ε_H the dielectric permittivity of the host medium and $\mathbf{E}_0$ the amplitude of the applied electric field. Then, the resonance of the GNP correspond to the maximum of the thermal energy production with a temperature variation given by:

$$\Delta T = \frac{V_{NP}}{2k_H \lambda r} \frac{\Im[\chi_{NP}]}{\sqrt{\varepsilon_H}} \left| \frac{3\varepsilon_H}{2\varepsilon_H + \varepsilon_{NP}} \right|^2 I_0 \tag{6.4}$$

where V_{NP} is the GNP volume, λ the wavelength of light, r the distance from the NP and I_0 the intensity of the impinging light (gaussian beam) [110]. For instance, Equation (6.4) can be used to predict the temperature variation around GNPs in water under optical illumination, where it is possible to assume no refractive index change induced by temperature variations [111]; on the contrary, if we consider spherical GNPs dispersed in a (well known and commercially available) thermotropic NLC (E7, by Merck) [30], this last condition is not fullfilled and, in order to study such a complex system, knowledge of the optical properties of the single constituents is required.

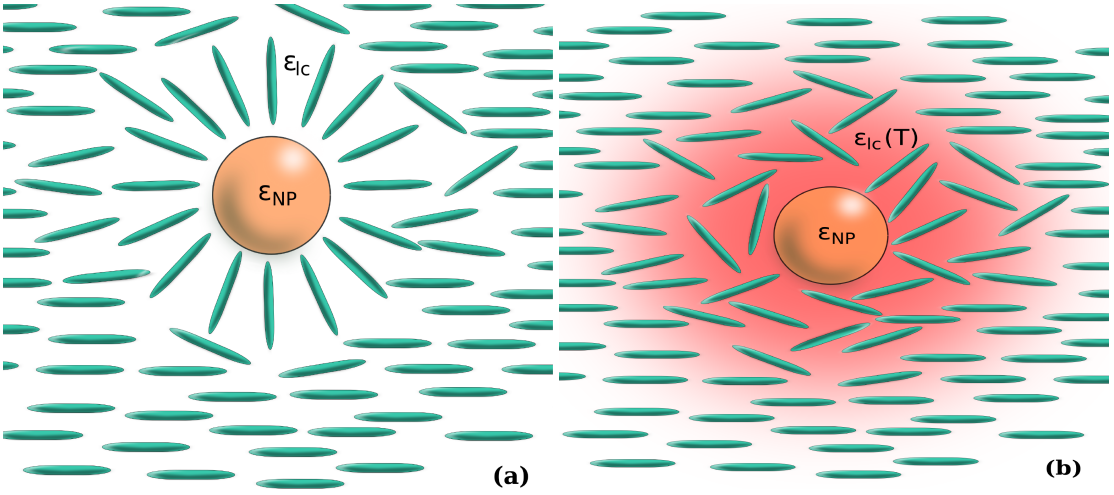

FIGURE 6.1: Sketch of the GNP dispersed in NLC: (a) without heating, (b) with heating

NLCs are elastic and anisotropic materials that possess both dielectric [112–116] and thermal conductivity [117] dispersion. Moreover, their optical properties (e.g. birefringence) depend on different external parameters, such as wavelength of the impinging radiation, external electric fields, and temperature. In particular, the wavelength and temperature dependence of their

refractive indices (both ordinary and extraordinary) are described by the extended Cauchy equations [114]:

$$n_e(\lambda,T) = n_i(\lambda) + G^{'}(\lambda)S(T) \tag{6.5}$$

$$n_o(\lambda,T) = n_i(\lambda) - \frac{G^{'}(\lambda)S(T)}{2} \tag{6.6}$$

$$\Delta n(\lambda,T) = \frac{3G^{'}(\lambda)S(T)}{2} \tag{6.7}$$

where $n_i(\lambda)$ is the refractive index of the isotropic state, n_o and n_e are the ordinary and extraordinary indices of the NLC respectively, $G^{'}(\lambda)$ is a proportionality constant (insensitive to temperature) and $S(T)$ is the order parameter of the NLC. By using typical (experimental) values of the E7 NLC in Eq.(6.7) [116], it is possible to obtain the expressions both for n_o and n_e as functions of temperature and wavelength of the impinging radiation.

As for GNPs, an impinging resonant radiation induces an electrical current due to the onset of the LSPR; then the Joule heating effect produces a temperature increase in each GNP. Consequently, this cools down by exchanging heat with the surrounding medium (NLC), which undergoes a dielectric permittivity variation, thus affecting the temperature variation of the GNP. A numerical simulation has been implemented in order to estimate both the equilibrium temperature of the system and the variation of the refractive indices of the NLC (surrounding medium).

The modeled system is made of a single spherical GNP immersed in NLC (Fig. 6.1). By fitting the experimental values [116], it is possible to obtain the Cauchy coefficients [113–116]. These coefficients provide an equation for both n_e and n_o as functions of T and λ,that can be easily implemented by using a numerical code. The equilibrium temperature of our system has been obtained by using Eq. 6.4 and realizing a do-while loop with the Eq. 6.5 (the loop is closed every time ΔT is less than 0.1^oC).

The polarizability α of the particle can be expressed as $\alpha = 3V_{NP}(\varepsilon_{NP} - \varepsilon_{LC})/(\varepsilon_{NP} + 2\varepsilon_{LC})$, where ε_{NP} is the dielectric permittivity of the GNP, V_{NP} is its volume, and ε_{LC} is the permittivity of the NLC. It is easy to show that α is directly related to the absorption cross section (C_{abs}) trough to the equation $C_{abs} = k\Im[\alpha]$ where k is the thermal conductivity of gold. Fig. 6.2 reports the calculation of the imaginary part of the polarizability as a function of the impinging radiation wavelength in two cases: the blue curve has been obtained by considering that the

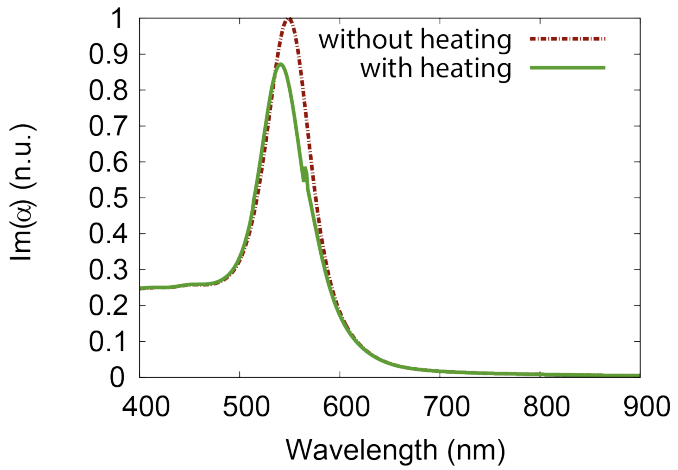

FIGURE 6.2: Imaginary part of the polarizability of the system (GNP + NLC) as a function of the wavelength of the impinging radiation.

refractive index of the surrounding medium does not change due to heating (e.g. external pump beam Off); the green curve, represents the polarizability of the system when the NLC refractive index changes because of the heating (e.g. external pump beam On). In both cases, the two curves exhibit a "quasi-Lorenzian" lineshape which is very similar to the absorption spectrum of monodispersed GNPs. The observed small blue shift can be explained by taking into account that the resonance condition is fulfilled (Fröhlich condition) if $\Re[\varepsilon_{NP}(\omega)] = -2\varepsilon_{LC}$. A modification in the value of the dielectric constant of the host material corresponds, therefore, to a tuning action on the LSPR frequency. In this case, due to a heat induced decreasing of ε_{LC}, the Fröhlich condition is fulfilled for higher (negative) values of ε_{NP}. It is well known [15] that, in the visible range, the real part of the electric permittivity of GNPs increases with frequency; therefore, fulfillment of the Fröhlich condition takes place for higher values of ω. This yields a blue shift of the plasmonic absorption peak.

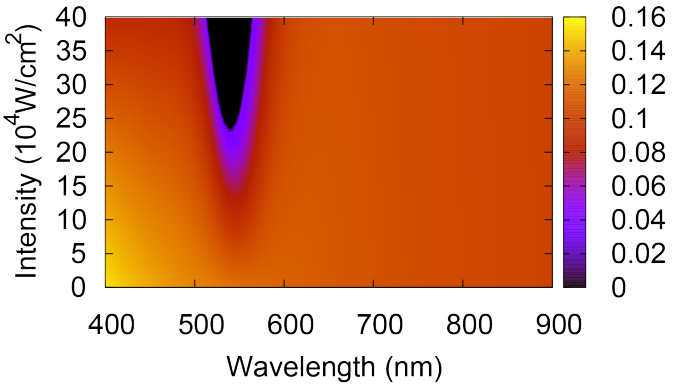

FIGURE 6.3: Map of the NLC birefringence as a function of light wavelength and intensity.

Fig. 6.3 shows a map of the dielectric anisotropy $\Delta n = n_e - n_o$ vesus the impinging light wavelength and intensity. The dark area highlights that a remarkable variation of Δn occurs only nearby the LSPR resonance frequency, where the absorption (see Fig. 6.2) and, therefore, the temperature variation of the system, exhibit their maximum. All above reported theoretical predictions have been validated by means of an experimental analysis reported in the next section.

6.3 Experimental results

Spherical cetyltrimethylammonium chloride (CTAC)-capped GNPs have been synthesized in aqueous solution and subsequently transferred in chloroform, which is a solvent (dispersing medium) also for Liquid Crystals (LCs). GNPs have been characterized by means of UV-vis absorption spectroscopy in the $400-800\,nm$ range: their absorption spectrum, after the phase transfer in organic medium is reported in Fig. 6.4 and shows the typical LSPR band centered at $526\,nm$. Transmission Electron Microscope (TEM) analysis has been performed by a Jeol JEM-1011 microscope operating at $100kV$. The specimens have been prepared by depositing a drop of the GNPs dispersion onto a carbon-coated copper grid and then allowing the solvent to evaporate. For a statistical determination of the average GNP size, at least 200 objects have been counted. The TEM image of GNPs, shown in Fig. (6.4) (inset), confirms that the particle

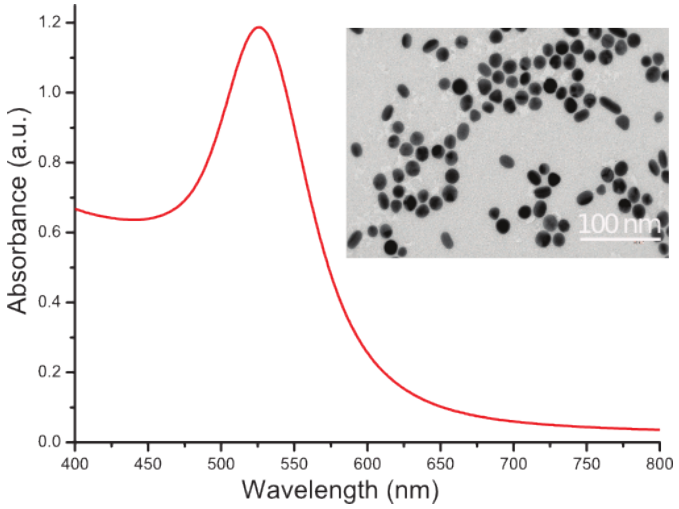

FIGURE 6.4: UV-vis absorption spectrum of GNPs dispersed in chloroform and their TEM image (inset).

population consists of GNPs with $17.4 \pm 2.2\,nm$ diameter; size and shape remain unchanged after phase transfer from the aqueous to the organic medium. Homogeneous mixtures of GNPs

up to 6% in weight in NLC (MDA-00-1444, by Licristal) have been obtained; however, above 4wt.%, the order parameter of the NLC phase is affected by the presence of GNPs as shown by a dramatic drop of the birefringence value. For this reason, we have used the mixture with the highest concentration of GNPs (3 wt.%) which does not affect the NLC phase. ITO coated glass substrates have been treated with a polyimide layer and rubbed for obtaining a planar orientation of the NLC director. A cell with a 2.7 μm cell gap has been filled with the NLC/GNPs mixture by capillary action at room temperature; the NLC director oriented parallel to the substrates along the rubbing direction. The excellent optical quality of the sample is evident in the polarizing optical photographs shown in Fig. 6.5. The optical contrast between bright (Fig. 6.5a) and dark

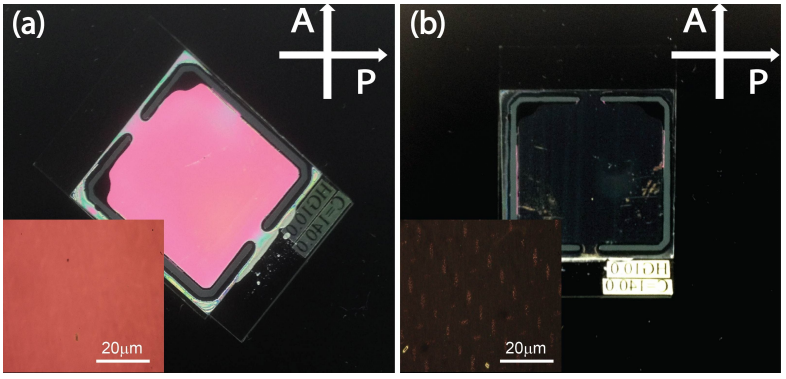

FIGURE 6.5: Pictures of the sample between crossed polarizers (a, b) along with their POM view. The director of the NLC is aligned at 45^o in (a) and at 0^o in (b). The red arrow represents the rubbing direction.

(Fig. 6.5b) states is higher than 40 : 1 for white non collimated light, and indicates an excellent NLC alignment. To check the spatial uniformity of this alignment, optical observations have been performed by means of a Polarized Optical Microscope (POM) equipped with a CCD color camera connected to a PC; results are reported in the insets of Fig. 6.5(a, b). The uniform change in contrast of the whole area (from Fig. 6.5a to Fig. 6.5b) suggests the NLC director alignment has not been macroscopically affected by the presence of GNPs, which are well dispersed in the NLC. Indeed, no NLC defects are visible in the POM view of the sample (insets of Fig. 6.5(a, b)). It is worth mentioning that, due to the low concentration (3 wt.%) of GNPs dispersed in the thin (2.7μm) NLC layer, the spectral analysis of the sample did not show any observable absorption peak (LSPR) related to the presence of the GNPs.

Experiments devoted to investigate the influence, on the NLC director alignment, of the local heating induced by a suitable optical radiation (trough the GNPs resonance) have been performed by using the all-optical setup reported in Fig. 6.6. The system used a low power density

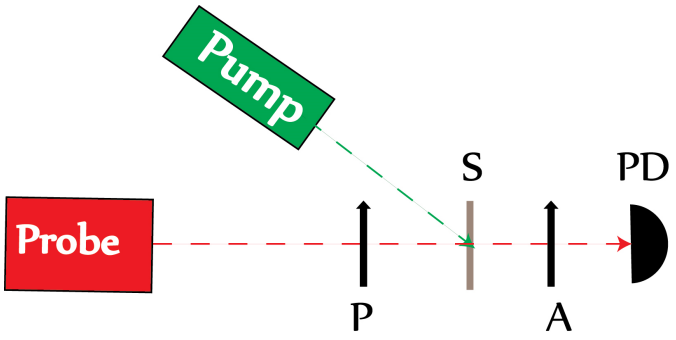

FIGURE 6.6: All-optical setup for sample characterization. P: polarizer; S: sample; A: analyzer; PD: photodetector.

($P_{probe} = 0.2\,W/cm^2$) CW probe laser, emitting at $\lambda = 633\,nm$ and a CW pump laser emitting at $\lambda = 532\,nm$, in the high absorption spectral range of GNPs (Fig. 6.4). For sake of simplicity, an unfocused pump beam, which impinges on the sample with an oval shape of about $(2 \times 3)\,mm^2$, has been used. The photo-thermal response of the sample has been observed between crossed polarizers, with the optical axis of the sample (NLC director orientation) set at 45^o with respect to the polarizer/analyzer axes. Under this condition, the sample acts as a retardation plate and the transmitted intensity can be detected by a photo-detector. Fig. 6.7a reports the probe intensity transmitted by the system, detected for different values of the pump light intensity (from $0.4W/cm^2$ to $3.1W/cm^2$, probe power kept constant). By optically pumping the same probed sample area, the photoexcitation of GNPs induces an electric-driven Joule heating, with a consequent energy exchange with the surrounding NLC. Such a local-heating induces a gradual suppression of the transmitted intensity, which is due to an induced reduction of the birefringence (Δn) of the sample. In fact, this has been calculated by using the Jones matrix formalism and exploiting the contrast between the steady state intensity transmitted by the sample with its optical axis at 45^o with the crossed polarizers, and the steady state intensity transmitted by the sample with its optical axis at $0^o/90^o$ with the crossed polarizers [118]. Fig. 6.7b shows that Δn values vary from 0.135 down to almost zero. The initial value of Δn is lower than in the pure NLC ($\Delta n \approx 0.2$); this can be explained by taking into account that the NLC order parameter is affected by the presence of GNPs, which may act as impurities, thus locally modifying (at the molecular scale) the NLC molecules order. It is worth noting that pump-probe experiments performed on a "reference" pure NLC cell of the same thickness, show that no variations in the trasmitted probe intensity are detected, neither when the sample is acted on by the highest intensity pump beam ($3.1\,W/cm^2$).

We have also performed a control experiment by detecting, as a function of the sample temperature, the transmittance of both the "reference" pure NLC cell, and our NLC/GNPs cell placed (inside a hot stage) between crossed polarizers, with the optical axis of the sample set at 45^o with the polarizer/analyzer axes. In both cases, as the sample temperature was increased, the transmitted intensity decreases towards a minimum which is almost zero. In addition, curves show that, in the reference cell, the pure NLC undergoes transition from nematic to isotropic at about 65^oC; on the other hand, in the cell containing NLC and dispersed GNPs, these ones act as a destabilizer perturbation for the NLC, lowering its transition temperature of about 10^oC, from about 65^oC to about 55^oC. Fig. 6.7c shows the Δn behavior predicted by the theoretical model:

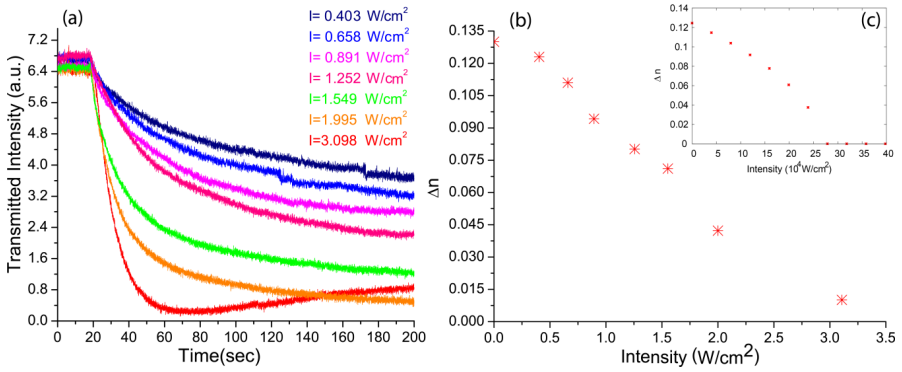

FIGURE 6.7: Transmitted intensity versus time for different intensity values of the pump radiation (a). Birefringence of the sample versus the intensity of the pump radiation ($\lambda = 532nm$) (b); calculated birefringence versus the intensity radiation for a specific wavelength ($\lambda = 532nm$) (c).

both experimental and theoretical results qualitatively exhibit the same behavior, while, from a quantitative point of view, there is a discrepancy between the experimental and the theoretical photo-heating intensity needed to induce the observed effect. From curves of Fig. 6.7 it is clear that, starting from $3.1W/cm^2$, new phenomena take place, that are related to a nonlinear response of the liquid crystal and give rise to effect that are preeminent with respect to the thermal one. At higher enough intensities, the transition of the LC to the isotropic phase takes place and the transmittance becomes zero. Those effects evolve with longer timescales and are out of the interest of the present work [119, 120].

To validate the theoretical model and verify that the NLC does not play any role in the photo-heating conversion, a control experiment has been performed by fabricating a sample made of

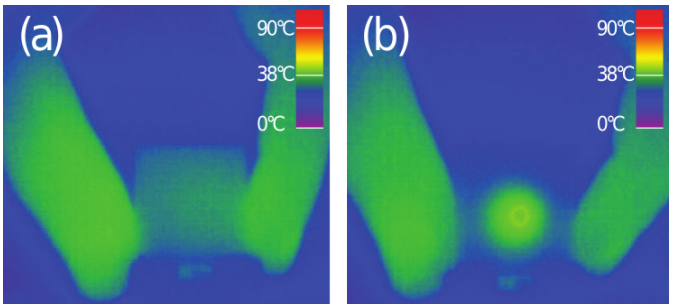

FIGURE 6.8: Thermographic analysis of the sample under optical irradiation for the pure NLC (a) and NLC/GNPs (b) cell.

pure NLC. The comparison has been performed by means of a thermographic analysis (thermocamera sensitivity $\approx 0.5^oC$) both of pure NLC and NLC/GNPs samples, under optical illumination. Experiments have been realized by keeping operator's hand fingers ($T \approx 37^oC$) close to the sample, in order to have a comparison setpoint: Fig. 6.8a shows that the thermocamera does not detect any color change (that is "temperature variation") for the pure NLC sample ($I = 3.1\,W/cm^2$; illumination time$= 300\,s$). On the contrary, in the same experimental condition, the thermographic analysis realized on the GNPs/NLC sample (Fig. 6.8b) shows that the surface of the illuminated area has been heated at a temperature of about 60^oC (close to the nematic to isotropic transition of the NLC), meanwhile the setpoint is kept at almost the same previous temperature ($T \approx 37^oC$). This result is an incontrovertible experimental evidence that the photoheating process is due to the photoexcitation of GNPs, with a consequent heat exchange with the surrounding NLC medium.

Finally, the dynamics of the system has been studied. A switching behavior which turns out to be reversible and repeatable, is observed when a sequence of pump beam pulses, obtained by utilizing an electronic shutter, is allowed to impinge onto the sample, put between crossed polarizers, with its optical axis forming an angle of 45^o both with the polarizer and the analyzer axes. Fig. 6.9 shows that, when the pump is switched on ($I = 3.1\,W/cm^2$), a photoexcitation of GNPs occurs, with a consequent phase transition of the NLC from the nematic to the isotropic state; thus between crossed polarizers the probe light experiences just the isotropic refractive index ($n_{iso} = 1.56$) of the NLC, and the transmitted intensity drops to zero ($\tau_{on-off} = 40\,s$). When the green pump beam is switched off, the NLC cools down and the Isotropic to Nematic transition occurs, thus restoring the sample birefringence, and, therefore, a transmitted light intensity ($\tau_{off-on} = 20\,s$).

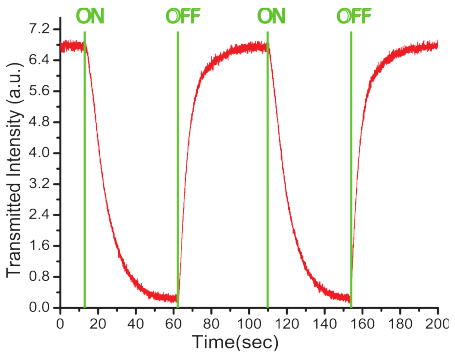

FIGURE 6.9: Switching behavior observed by using a periodic sequence of pump beam pulses. ON and OFF refer to the pump beam being allowed to impinge on the sample or not.

6.4 Conclusion

In this chapter an investigation of the nanoscale heat propagation in a system consisting of photo-excited GNPs surrounded by thermo-sensitive NLC has been reported. A theoretical model, based on the thermal heating equation, has been implemented. Experiments have been realized by dissolving a suitable amount of GNPs in NLC. The well aligned hybrid system (NLC/GNPs) exhibits a photo-thermal sensitivity, and experimental results show a strong change in the value of the refractive index of the NLC when GNPs are photo-heated by a suitable (resonant) optical radiation. A thermographic comparison between the hybrid system and the pure NLC, carried out in the same experimental conditions, shows that the photo-thermal conversion is only due to the LSPR mechanism. Theoretical predictions and experimental results exhibit a good qualitative agreement.

Chapter 7

Plasmonic thermometer based on Cholesteric Liquid Crystals

7.1 Introduction

Localized Surface Plasmon Resonance (LSPR) of noble Metal Nanoparticles (MNPs) opens up a new horizon for nanoscale materials able to convert light into heat, since the strong electric field generated around the MNPs can transform them into original heat nanosources. Thus, investigation of the heat transport mechanism, from the heated MNPs to their surrounding medium, is fundamental for realizing applications in nanotechnology and thermal-based therapies, and a challenge is definitely represented by the possibility of measuring temperature variations at the surface of the MNPs undergoing optical illumination. In this chapter, it is showed that an ingenious combination of characteristics of short pitch liquid crystalline compounds and MNPs has demonstrated effective to provide an advanced tool to monitor nanoscale temperature variations.

Metal NPs, as seen in previous chapters, are characterized by LSPR [85]. The spectroscopic properties of NPs can be described in the framework of Mie theory *see Chapter 1* and Gans (**??**) theories, implemented to explain the behavior of spherical and rod like NPs, respectively.

In this chapter it is presented an original method to monitor the heat generated at the nanoscale by using Gold Nanorods (GNRs) that, due to their asymmetric shape, possess two LPRs: a transverse and a longitudinal one. Remarkably, acting on the GNRs aspect ratio, the position of

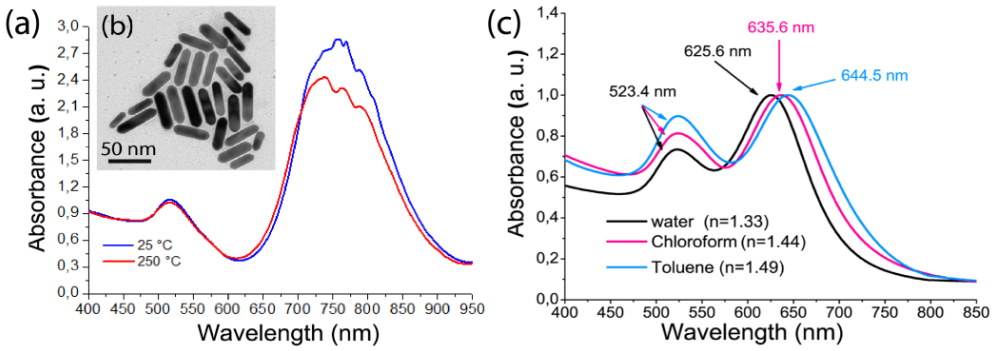

FIGURE 7.1: Thermal stability test of GNRs dispersed in chloroform (a); TEM micrograph of the GNRs dispersed in chloroform (b); normalized absorption spectra of GNRs in different dispersing media (c).

their longitudinal LPR, which shows a high sensitivity towards the surrounding medium, can be finely tuned in the visible and near infrared range [77]. Thus, a smart thermosensitive material (Cholesteric Liquid Crystal - CLC [31]), which is able to change its selective reflection band as a function of temperature, has been specifically selected to measure temperature variations around the NPs of the sample. By recording the spectrum of the mixture CLC – GNRs for different values of the temperature around the NPs, in which the longitudinal LSPR has been suitably excited, we have made a calibration of a nano-thermometer, which enables to estimate the induced temperature variations.

7.2 Gold nanorods dispersed in cholesteric liquid crystal

Water dispersible, cetyltrimethylammonium bromide $(CTAB)$ capped, GNRs have been synthesized by means of a seed mediated, protocol involving a room temperature chemical reduction of $HAuCl_4 \cdot 3H_2O$ in a CTAB micellar solution, assisted by $AgNO_3$, to promote an anisotropic growth [124]. GNRs have been subsequently transferred in chloroform by functionalization with decanoic acid, in order to become dispersible in a common medium with Liquid Crystals (LCs).

The stability of GNRs in chloroform has been tested by heating the dispersion of GNRs up to $250°C$. Remarkably, it has been observed that, up to $100°C$, GNRs do not exhibit any modification induced by the thermal treatment, thus confirming that they preserve their geometry. Moreover, by heating the solution up to $250°C$, an irreversible modification (in terms of width

and amplitude) of the longitudinal plasmon band, which is due to a change of the GNRs shape (the so called reshaping) has been observed (Fig. 7.1a) [125]. Furthermore, the Transmission Electronic Microscope (TEM) image reported in the inset of Fig. 7.1a shows that the main GNRs population presents an aspect ratio (AR) of 2.3, and no variation in the AR is detected upon the thermal treatment. The transfer of the GNRs in a different dispersing medium, chloroform and toluene, has been found to induce a shift of the longitudinal plasmon band, (Fig. 7.1c), which can be explained by taking into account the high sensitivity of the extinction coefficient of the system to the actual value of the refractive index of the surrounding medium [126]. In fact, under resonance conditions, the heat produced by the NPs, due to the Joule effect, is directly proportional to the energy of the strong electric field generated around the NPs [102]. Indeed, as described in *Chapter 5* the heat generated is proportional to the square of the electric field inside the NPs E_{int}, which is, in turn, directly proportional to the external electric field E_0 (7.1). Therefore, the heat generated around the NPs results directly proportional to the intensity of the impinging light.

$$E_{int} = \frac{3\varepsilon_m}{\varepsilon(\omega) + 2\varepsilon_m} E_0 \tag{7.1}$$

In order to exploit the NPs as nano-source of heat [61], the possibility of monitoring temperature variation in their vicinity under optical illumination is crucial. For this purpose, a clever combination of NPs with a thermosensitive materials has been studied. GNRs have been dispersed in a thermotropic liquid crystal, which is able to change its optical properties as a function of external perturbations, such as electric or magnetic fields, and temperature variations [127]. In particular, it has been selected a cholesteric liquid crystal (CLC) that behaves as a one dimensional photonic band gap, due to the periodic arrangement of its molecules; in this way, a specific wavelength can be reflected (Bragg's wavelength) once the CLC is aligned in a planar geometry inside the cell (Fig. 7.2a).

In order to detect temperature variations around GNRs, the ability of CLC to tune its reflection band as a function of these variations has been exploited. The utilized CLC is characterized by a Bragg's wavelength $\lambda_B \approx 520\,nm$ and has been obtained by twisting a nematic LC (MDA-00–1444, by Licristal) with a 20% in weight of a chiral agent of (ZLI-811, by Licristal); then, a homogeneous mixture with GNRs (up to 7 wt%) has been prepared. The presence of GNRs

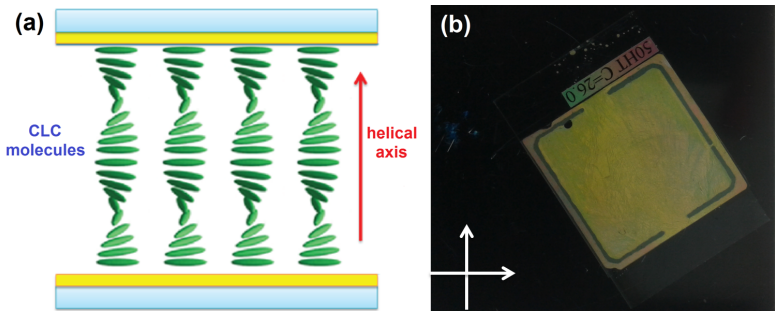

FIGURE 7.2: Sketch of a planar alignment of Cholesteric Liquid Crystal in a cell (a). Polarized optical microscope view of the CLC-GNRs sample (b).

in the system has been found to red-shift the typical reflection band of the CLC; however, this shift can be eliminated by adding a suitable amount (8%) of chiral agent to the mixture; in this way, the Bragg's wavelength of the CLC-GNRs sample turns out to return around $520\,nm$. By capillary flow, the mixture was then introduced at room temperature in a cell, whose glasses were treated to obtain a planar alignment of the CLC. In this way, the CLC director **n** orients parallel to the substrates, while its helical axis goes normal to them (Fig. 7.2a). In Fig. 7.2b it is possible to see the sample between crossed polarizers, which appears bright due to its birefringence.

7.3 Optical characterization of GNRs-CLC composites

To investigate the influence on the CLC configuration of the local heating induced by a suitable optical radiation through the GNRs resonance, we have performed all-optical experiments by means of the pump-probe setup reported in Fig. 7.3a. This utilizes a collimated white source ($350\,nm < \lambda < 950\,nm$) for monitoring the spectral properties of the sample, and a CW NIR pump laser emitting at $\lambda = 800\,nm$ (power pump $P = 0.2W/cm^2$), that match perfectly with the longitudinal band of GNRs. The reflected component of the probed light has been monitored by means of a spectrometer Ocean Optics ($USB2000+$).

Fig. 7.3b reports the behavior of the sample (CLC-GNRs) under illumination with the pump beam, for different exposure times. The CLC acts as a mirror for wavelengths of the impinging white light falling within the reflection band, which are back reflected. By optically pumping a given sample area, the photoexcitation of GNRs induces, due to the Joule effect, a generation of localized heat, which induces an elongation of the CLC pitch, with a consequent linear red-shift of the reflection band. Indeed, by keeping constant the pump power and increasing the exposure

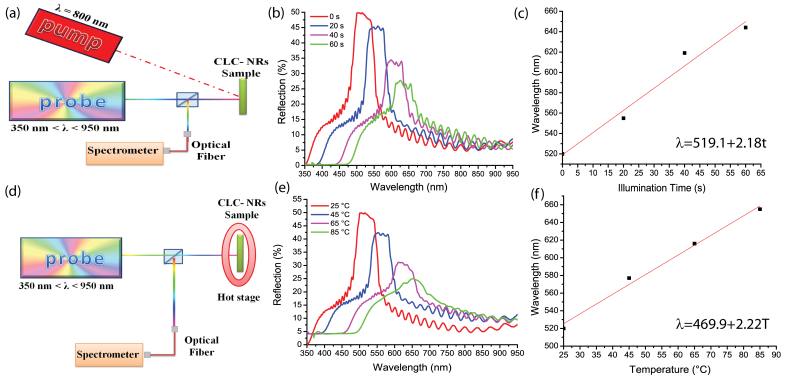

FIGURE 7.3: Pump-probe setup (a); Reflection response of the CLC-GNRs sample under optical pumping (b); Linear fit of the position of Bragg's wavelength versus illumination time (c); Thermal setup (d); Reflection response of the CLC-GNRs sample under the temperature variation effect (e); Linear fit of the position of Bragg's wavelength versus temperature (f).

time, a linear red shift and a partial suppression of the reflection band are detected, which are due to a gradual increasing of the local temperature. In addition, the elongation of the CLC pitch reduces the number of periods in the bulk of the cell, an effect that yields an attenuation and a broadening of the reflected signal amplitude. To validate the effect of the GNRs-induced local heating on the CLC optical response, a control experiment has been performed by increasing the sample temperature from 25°C up to 85°C by means of a hot stage (Fig. 7.3d) and monitoring the behavior of the reflected signal (Fig 7.3e). Also in this case, a linear red-shift has been observed, which clearly confirms the photo-thermal behavior reported in Figure 7.3b.

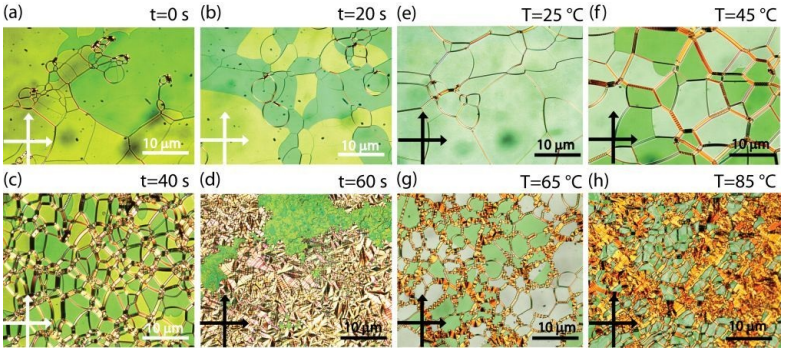

FIGURE 7.4: POM view of CLC-GNRs sample between crossed polarizers for different illumination time: 0s (a); 20s (b); 40s (c); 60s (d); and value of temperature: 25°C (e); 45°C (f); 65°C (g); 85°C (h).

The sample morphology has been investigated by means of a Polarized Optical Microscope (POM): Figures 7.4(a-d) and Figures 7.4(e-h) show that, by heating up the sample both with light and uniform heating, it is possible to induce drastic morphological changes in the sample textures (the so called oily streaks), which reflect the correlation between the position of the

reflection band and the temperature of the sample. The fact that the system can be utilized for monitoring temperature variations, occurring in the sample under optical illumination, is confirmed by the circumstance that the two functions reported in Figures 7.3c and 7.3f, which fit the position of Bragg's wavelength as a function of the illumination time and as a function of temperature, respectively, exhibit, within the experimental error, the same linear behavior. This represents a clear confirmation that the photoexcitation of the NPs in the sample produces the same spectral effects produced by temperature variations induced by the hot stage. The thermal sensitivity of the proposed method has been evaluated by means of the linear fit used to obtain the relation between temperature (T), and Bragg's wavelength (λ_B):

$$\delta T = \frac{1}{2.28}\lambda - 206.09 \tag{7.2}$$

For the measured values and precision of (λ_B) , by using the error propagation, we obtain:

$$\delta T = 0.35^{\circ}C \tag{7.3}$$

7.4 Conclusion

In this chapter a method to exploit the properties of soft matter to carry out an accurate evaluation of temperature variations is presented. Thanks to the periodic arrangement of the director in a CLC, and to its sensitivity to temperature variations, is possible to monitor the temperature around NPs in a mixture of CLC-GNRs. In this way, by simply acquiring the spectrum of the sample, it is possible to estimate temperature variations around NPs with the quite high sensitivity of about $0.35^{\circ}C$.

Chapter 8

Plasmonic Photo-Thermal Therapy (PPTT) using Gold NanoRods

8.1 Introduction

Plasmonic Photo-Thermal Therapy (PPTT) represents a minimally-invasive, drug free therapy in which light is converted into heat to kill cancer cells. Gold nanoparticles are good absorbers of light that can be efficiently converted into heat (see *Chapter 5*). This new alternative treatment of cancer diseases has attracted great interest in recent years. In this chapter a brief description of this innovative therapeutic method is reported with special enphasis on the use of gold nanorods as therapeutic agent to minimize the impact of the heat on the health tissues.

Cancer is a disease characterized by an uncontrolled growth and spread of abnormal cells. It can form tumors on tissues or grow in the body flow system. World Health Organization (WHO) estimated that 84 million people died of cancer between 2005-2015. It is caused by DNA damage which can be inherited or induced by enviromental factors. Current mainstream treatments include surgery, chemotherapy or radiation.

- Surgical extirpation is highly effective in primary tumors, but it is limited to surgically recognizable and accessible tumors and thus cancer cells may not be completely removed.

- Chemotherapy is the use of chemical drugs to fight cancer. The systemically administrated drugs circulate in the body to kill cells that divide rapidly, especially cancer cells. It commonly has significant side effects due to the drug toxicity to normal cells and is subject to the development of resistance by the cancer cells.

- As for radiation, the use of high energy ionization particles (X-rays, gamma rays or electrons) to damage cell and tissue at a molecular level, is often used as a complementary approach, to eradicate remaining cancer cells after surgery. It can cause damage to the healthy tissues close to the cancer cells or in the path of the radiation beam.

An alternative method to the ones above mentioned is the Hyperthermia where laser heating sources ranging from radio-frequency to microwaves as well as ultrasound waves are used to induce moderate heating in a specific target region. Hyperthemia is commonly defined as heating tissue to a temperature in the range $41^\circ - 47\,^\circ C$ for tens of minutes. Tumors are selectively destroyed in this temperature range because of their reduced heat tolerance compared to normal tissue, which is due to their poor blood supply. Hyperthermia causes irreversible cell damage by loosening cell membranes and denaturing proteins. But the applications of the heating sources conventionally employed for hyperthermia are limited because of their damage to surrounding healthy tissues. A revolution in cancer therapy has taken place by the emerging use of laser light to achieve controlled and confined thermal damage in the tumor tissue by exploiting the photothermal properties of metal nanoparticles. As seen in previous chapters, plasmonic nanoparticles (NPs) hold a unique photophysical phenomenon, called Localized Surface Plasmon Resonance (LSPR), which causes a strong ehnancement of the absorption and scattering efficiencies. The light absorption or scattering of gold NPs, depending on the size and shape of the latter, are at least 10^3 times stronger than the absorption or emission of any organic dye molecules. For these reasons NPs can be considered good candidates as nano-localized *concentrators* of energy.

8.2 Tuning LSPR to the NIR region

PPTT is based on the utilization of Au NPs to destroy cancer cells in a selective way, without affecting the healthy tissue. For this purpose, it is important to minimize the heat of the healthy tissue, a task that can be accomplished by exploiting the extraordinary capability of NPs to

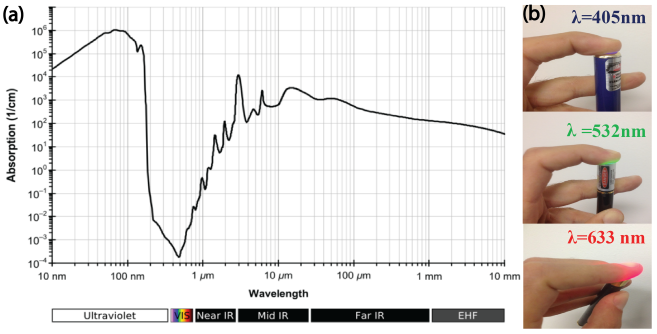

FIGURE 8.1: Liquid water absorption spectrum (a), Penetration of visible light into living tissue (b).

convert light into heat, when shed through a biological window [128]. To this aim, it is necessary to work with an infrared radiation (IR), whose wavelength perfectly falls in the so called "first water window", where the absorption of the human tissue is minimum (Fig. 8.1a).

In fact, by observing the penetration into a human finger of visible light of three different wavelengths, it is evident that, moving toward the infrared region of the spectrum, the penetration depth noticeably increases (Fig. 8.1b). In addition, in presence of NPs, light scattering is drastically reduced in the wavelength range of the plasmonic band of NPs, in favor of a higher absorption. By changing their structure and shape, the LSPR frequency of gold nanoparticles can be tuned to the near infrared (NIR) region. Currently there are three major types of NIR-absorbing gold-based nanoparticles that are useful in PPTT (Fig. 8.2): gold nanorod (Au NRs)[130], gold nanoshell (Au NS)[129] and gold nanocage (Au NCs) [131].

FIGURE 8.2: Color variations arising from changes in the composition, size, and shape of nanoparticles for gold nanorods (a)nanoshells (b) and nanocages (c) respectively.

- Au NR [132–134] shows two absorption bands: a strong absorption band in the NIR region due to the electron oscillation along the longitudinal direction and a weak band in the visible region around $520\,nm$ due to electron oscillation along the transverse direction. This optical behavior has been well explained using Gans theory [60]. The transverse band is insensitive to the aspect ratio ($length/width$) of the rod. The longitudinal band wavelength greatly red shifts from visible to NIR region in a linear relationship with increased intensity when the aspect ratio increases [135] (Fig. 8.3).

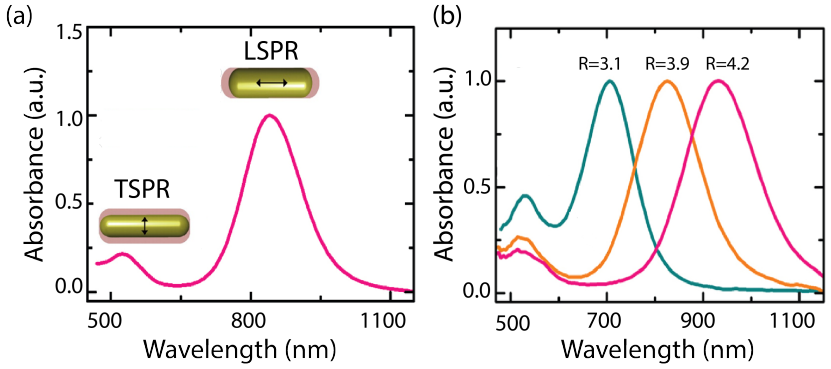

FIGURE 8.3: Sketch of the longitudinal (LSPR) and transverse localized plasmon resonance (TSPR) for gold nanorod (a), vis-NIR spectra evolution for different aspect ratio (R).

- Au NS is composed of a spherical silica core ($100-200\,nm$ in diameter) and a thin layer of gold ($5-20\,nm$).This two concentric spherical structures shows red-shifted absorption due to the coupling between the inner and outer shell surface plasmons [136]. Decreasing the ratio of shell thickness to core radius largely red shifts the LSPR wavelength from the visible to NIR region. The LSPR frequency decreases near-exponentially with decrease in the shell thickness-to-core radius ratio, with a trend that is universal and independent of the nanoshell size, core material, shell metal, or surrounding medium [137].

- Au NC is developed as a NIR-absorbing gold nanostructure by Xia group [138]. It is composed of a thin and porous gold wall with hollow interior. Changing the wall thickness, the hole size and porosity can tune the LSPR wavelength from the visible to the NIR region. This is experimentally controlled by the amount of auric acid that galvanically replaces silver cubes to obtain the nanocages. Increasing the amount of the auric acid red shifts the LSPR [138].

8.3 Morphological study of Hela cells treated with AuNRs

In this framework we have conducted a morphological study *in vitro* on a particular kind of tumors cells (Hela) by treating them with AuNRs. Hela or hela cell line, is the oldest and most commonly used human cell line [139] in scientific research. The line was derived from cervical cancer cells taken on February 8, 1951 [140], from Henrietta Lacks, a patient who died of her cancer on October 4, 1951. The cell line was found to be remarkably durable and prolific — which led to its contamination of many other cell lines used in research.

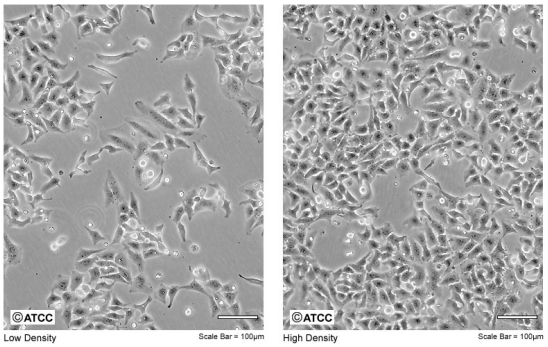

FIGURE 8.4: Optical microscopy view of Hela tumor cells.

In our test, Hela cells were left to grow in adhesion on a ITO substrate for 18 hours @ $37°C$ in 0.5% of CO_2, by utilizing the D-MEM as a culture medium. Then we compared two different fixation methods for preservation of the morphology of the cells, in order to preserve the tissue architecture, this condition being important in our analysis in order to be able to valuate only the morphological impact induced in a second step by the presence of AuNRs. In this first step we treated the cells with formaldehyde (10%) and methanol (90%) for the same grow time. For the sample fixed in formaldehyde, SEM analysis shows details of the cell surface much sharper compared to the images obtained for the cells treated with methanol (Fig. 8.5); in the latter case, in fact, the cells result to be too clumped to pick out the details.

Once established that the best method of fixation corresponds to cells treated with formaldehyde, we treated the cells directly with the GNRs. Different concentration of AuNRs have been used in order to estimate the impact of them on the cells. The AuNRs used in this work are dispersed in water and cappaed with CTAB (cetyltrimethylammonium bromide) characterized by a resonance peak at $796nm$.

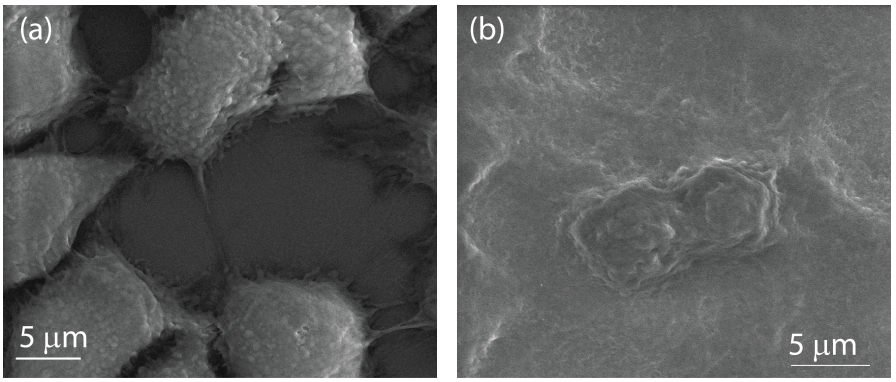

FIGURE 8.5: SEM images of Hela cells treated with formaldehyde (a) and methanol (b).

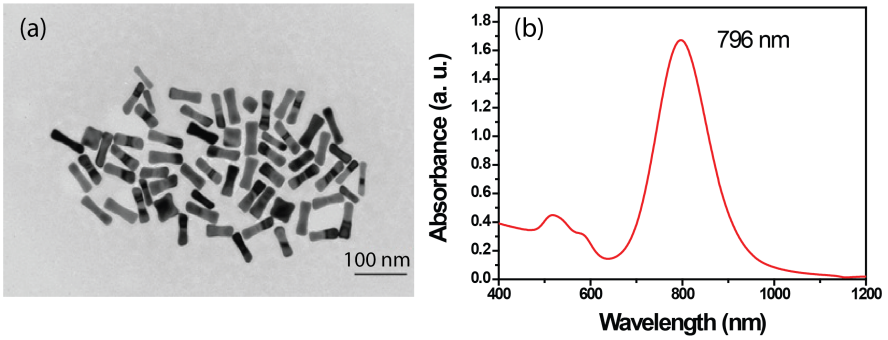

FIGURE 8.6: TEM images (a) and visible spectrum of gold nanorods (b).

By keeping the same condition of growth we had 10 % of AuNRs for 3 hours (case I) and 16 hours (case II), respectively. SEM images this time do not show any morphological difference in the cells structures in case A (Fig. 8.7), while in case B they result to be ”exploded” (Fig. 8.8).

In order to evaluate the toxicity of the AuNRs, a cell viability test has been carried out by considering different concentration of AuNRs in the range $5 \cdot 10^{-4} - 8 \cdot 10^{-2}$ for two different incubation times (1 hour and 2 hours). Results resumed in table 8.3 show that the concentration of $1 \cdot 10^{-2}$ represents the threshold-concentration for which the cell death, related to the high concentration of gold in the sample, is less than 10%. This occurs for both the incubation time.

Cell viability test: Hela cells and AuNRs

Time	**Basal conditions**	$5 \cdot 10^{-4}$	$2.5 \cdot 10^{-3}$	$5 \cdot 10^{-3}$	$1 \cdot 10^{-2}$	$2 \cdot 10^{-2}$	$3 \cdot 10^{-2}$	$4 \cdot 10^{-2}$	$8 \cdot 10^{-2}$
1h	100%	98.3%	98.5%	**97.9%**	**91.2%**	**0**	**0**	**0**	**0**
2h	100%	98.0%	98.2%	**87.3%**	**90.3%**	**0**	**0**	**0**	**0**

TEM images show that the cells mainly absorb NPs by engulfing them by means of an endocytosis process. This process is used by all cells of the human body because most substances important to them are large, polar, molecules that cannot pass through the hydrophobic plasma

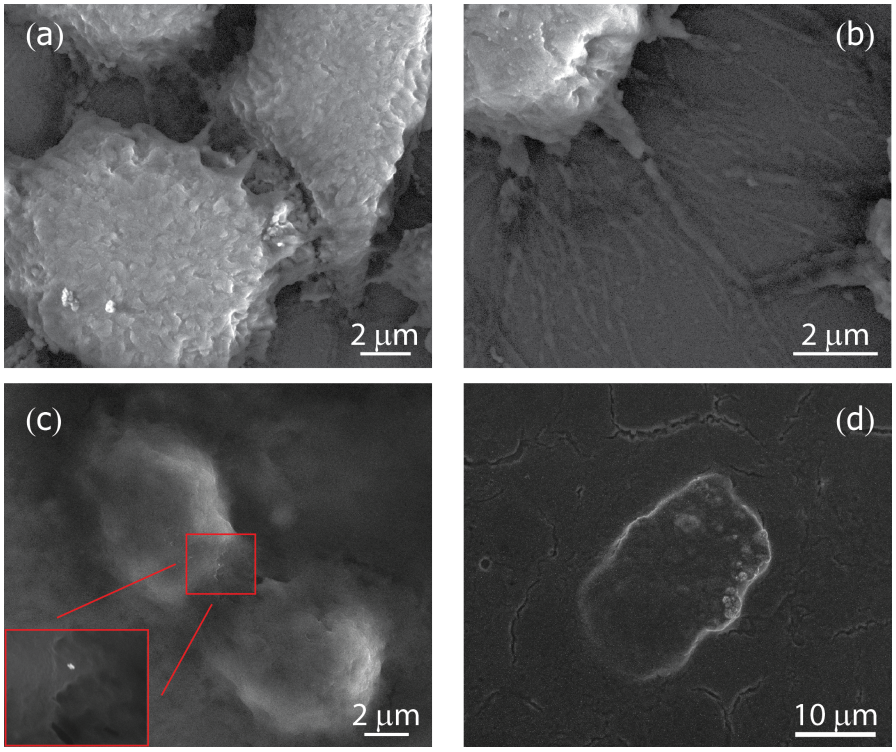

FIGURE 8.7: SEM view of tumor cells fixed with formaldehyde (treated with NPs for 3h)(a,b,c) and E-SEM view of one of them.

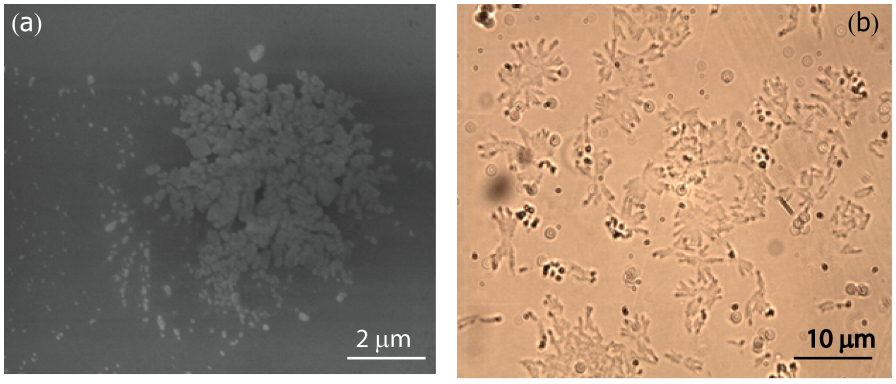

FIGURE 8.8: SEM view of tumor cells fixed with formaldehyde (treated with NPs for 16h)(a) and optical view of them (b).

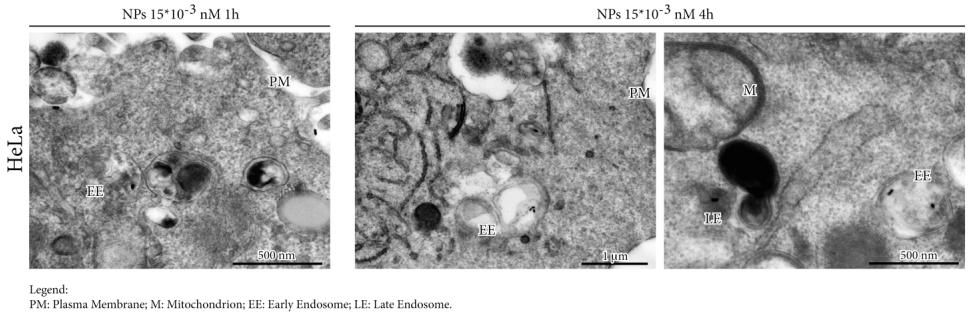

FIGURE 8.9: TEM view of the Hela cells treated with AUNRs for two different times.

or cell membrane. Further investigation can determine whether the input mechanism in the cells of NPs is also linked to other mechanisms.

8.4 Conclusions

In this chapter a very preliminary study conducted on the interaction between cancer cells and gold nanoparticles is reported. The application of nanomaterials in the fight against cancer could constitute a turning point in the treatment of these kind of diseases.

Conclusions

In this thesis the distinctive capabilities of liquid crystals to control the Localized Surface Plasmon Resonance (LSPR) of gold nanoparticles (NPs) are illustrated, along with the investigation of their potentialities to realize active plasmonic nanodevices. The interaction of visible light with the conduction electrons of metallic NPs leads to a coherent charge oscillation, which is responsible of an enhancement of the near electric field around the NPs and an increase of absorption. For spherical NPs, this phenomenon is well described by the Mie theory, and strongly depends on the size and shape of the nano-objects and on the dielectric function of the surrounding medium. Tuneability of LSPR can be obtained by means of a change in the size or shape of the nano-objects, which represents a *passive control* of the resonance property of metal NPs. In this case, to control the LSPR it is necessary to modify the nano-object during the fabrication process (e.g synthesis process in the case of bottom-up fabrication approach). By acting, instead, on the surrounding medium, the LSPR can be *actively controlled*, without any need of modifying the intrinsic properties of the NPs. A further progress in this direction is represented by the possibility to use a surrounding medium whose dielectric function can be controlled by means of external stimuli such as electric field, magnetic field, temperature variations and so on. Liquid crystals (LCs) possess such properties. We report a study of the interaction between LCs and gold NPs, which enables to control the LSPR. In the first part of this work, the self-assembly property of a biological LC, a whole-genome DNA, is used to organize gold nanorods by means of electrostatic interaction. We demonstrated that the helical arrangement of DNA is able to induce both a nanoscale organization and, simultaneously, a long-range order in GNRs. In this way artificial nano-composite structures offer a pathway to the development of engineered materials with novel macroscopic properties. The second part of this work is devoted to thermoplasmonics, and in particular to the use of LCs to investigate, monitor and control

temperature variations induced by the LSPR. The photo-induced heating delivered by gold NPs represents a powerful tool in different field such as: drug delivery, gene-therapy, solvo-thermal chemistry, plasmonic photothermal therapy and so on. The measurement and the control of the heat generated by metallic nanostructures is still an open question; until now, researchers have focused their attention on the study of systems consisting of a few elements (e.g. only one NP or a limited number of NPs organized in arrays or matrices). The main contribution reported in this thesis, related to the investigation of the photo-induced heat, is represented by a study of the heat delivered from a huge number of randomly distributed gold NPs, homogeneously distributed on a glass substrate. Experimental analysis showed that significant temperature variations, of about tens of degree, can be induced and measured by means of a thermo-camera; the observed heating effect is related to the huge number of NPs that are simultaneously excited. The phenomenon is numerically and theoretically well described as due to a collective effect of all the involved NPs: the contribution of each NP to heat production is simply added to the one of all other GNPs. This represents a very simple method to estimate temperature variations in complex systems. Experimental and theoretical results are in good agreement. In the last part of this work nematic and cholesteric LCs are used to control and detect the temperature variations induced by gold NPs. In particular we exploited the temperature dependence of the birefringence of nematic LCs (NLCs) to measure the heat delivered by gold NPs. In this way, we obtain an estimation of the effect of temperature variations by simple monitoring the transmitted intensity of a NLC-NPs cell. In the case of cholesteric LCs (CLCs) we monitor the position of Bragg's wavelength, which undergoes a red-shift due to the photo-excitation of the LSPR. In this case we obtain a precise, quantitative, estimation of the heat generated by NPs. In both cases (NLC-NPs and CLC-NPs cells), by controlling the refractive index of the LCs, we can control the LSPR and the resulting heat. Above results can be exploited in an approach devoted to use gold NPs in the fight against cancer. The thesis is closed with a preliminary analysis of the interaction between a particular kind of gold NPs, the nanorods, and tumor cells. We show that it is possible to kill cancer cells avoiding to damage healthy tissues. This is possible by exploiting a radiation wavelength at which the absorption of the human tissue is minimum, while the absorption of the NPs inside the tumor cells is maximum.

Acknowledgement

A particular thanks to prof. Umeton for this opportunity and the Air Force Office of Scientic Research (AFOSR), Air Force Research Laboratory (AFRL), U.S. Air Force, under grant FA9550-14-1-0050 (EOARD 2014/2015) for the financial support.

Bibliography

[1] Hong-Gyu Park, Jong-Jin Lee, Ki-Young Dong, Byeong-Yun Oh, Young-Hwan Kim, Hae-Yoon Jeong, Byeong-Kwon Ju, and Dae-Shik Seo. Homeotropic alignment of liquid crystals on a nano-patterned polyimide surface using nanoimprint lithography. *Soft Matter*, 7(12):5610–5614, 2011.

[2] Hayato Takahashi, Takumi Sakamoto, and Hiroyuki Okada. Liquid crystal device with 50 nm nanogroove structure fabricated by nanoimprint lithography. *Journal of Applied Physics*, 108(11):113529, 2010.

[3] Roberto Caputo, Luciano De Sio, Alessandro Veltri, Cesare Umeton, and Andrey V Sukhov. Development of a new kind of switchable holographic grating made of liquid-crystal films separated by slices of polymeric material. *Optics letters*, 29(11):1261–1263, 2004.

[4] Luciano De Sio, Alessandro Veltri, Alessandro Tedesco, Roberto Caputo, Cesare Umeton, and Andrey V Sukhov. Characterization of an active control system for holographic setup stabilization. *Applied optics*, 47(10):1363–1367, 2008.

[5] Luciano De Sio, Svetlana Serak, Nelson Tabiryan, and Cesare Umeton. Mesogenic versus non-mesogenic azo dye confined in a soft-matter template for realization of optically switchable diffraction gratings. *Journal of Materials Chemistry*, 21(19):6811–6814, 2011.

[6] Hirotsugu Kikuchi, Masayuki Yokota, Yoshiaki Hisakado, Huai Yang, and Tisato Kajiyama. Polymer-stabilized liquid crystal blue phases. *Nature materials*, 1(1):64–68, 2002.

[7] E Cattaruzza, G Battaglin, F Gonella, R Polloni, BF Scremin, G Mattei, P Mazzoldi, and C Sada. Au–cu nanoparticles in silica glass as composite material for photonic applications. *Applied Surface Science*, 254(4):1017–1021, 2007.

[8] Carlos Pecharromán, Antonio Esteban-Cubillo, Héctor Fernández, Leticia Esteban-Tejeda, Raul Pina-Zapardiel, José S Moya, Javier Solis, and Carmen N Afonso. Synthesis, conforming, linear, and non-linear optical properties of gold nanoparticles-sepiolite compacts. *Plasmonics*, 4(4):261–266, 2009.

[9] Catherine Louis and Olivier Pluchery. *Gold nanoparticles for physics, chemistry and biology*. World Scientific, 2012.

[10] John M Ziman. *The physics of metals*, volume 1. CUP Archive, 1969.

[11] Michael Quinten. *Optical properties of nanoparticle systems: Mie and beyond*. John Wiley & Sons, 2010.

[12] P. Drude. Zur elektronentheorie der metalle. *Annalen der Physik*, 306(3):566–613, 1900. ISSN 1521-3889. doi: 10.1002/andp.19003060312. URL http://dx.doi.org/10.1002/andp.19003060312.

[13] N.W. Ashcroft and N.D. Mermin. *Solid State Physics*. Saunders College, Philadelphia, 1976.

[14] S.A. Maier. *Plasmonics: Fundamentals and Applications*. Springer, 2007. ISBN 9780387378251. URL http://books.google.it/books?id=yT2ux7TmDc8C.

[15] Peter B Johnson and R-W_ Christy. Optical constants of the noble metals. *Physical Review B*, 6(12):4370, 1972.

[16] Prashant K Jain, Kyeong Seok Lee, Ivan H El-Sayed, and Mostafa A El-Sayed. Calculated absorption and scattering properties of gold nanoparticles of different size, shape, and composition: applications in biological imaging and biomedicine. *The Journal of Physical Chemistry B*, 110(14):7238–7248, 2006.

[17] Craig F. Bohren and D.R. Huffman. *Absorption and scattering of light by small particles*. Wiley science paperback series. Wiley, 1983. ISBN 9780471293408. URL http://books.google.it/books?id=S1RCZ8BjgN0C.

[18] G. Mie. Beiträge zur Optik trüber Medien, speziell kolloidaler Metallösungen. *Annalen der Physik*, 330(3):377–445, 1908. ISSN 1521-3889. doi: 10.1002/andp.19083300302. URL http://dx.doi.org/10.1002/andp.19083300302.

[19] Max Born and Emil Wolf. *Principles of optics: electromagnetic theory of propagation, interference and diffraction of light*. Cambridge university press, 1999.

[20] Fabrice Vallèe. Optical properties of metallic nanoparticles. In *Nanomaterials and nanochemistry*, pages 197–227. Springer, 2007.

[21] Iam-Choon Khoo. *Liquid crystals: physical properties and nonlinear optical phenomena*, volume 64. John Wiley & Sons, 2007.

[22] Shri Singh and David A Dunmur. *Liquid crystals: fundamentals*. World Scientific, 2002.

[23] Naoki Ito, Kenji Sakamoto, Ryuichi Arafune, and Sukekatsu Ushioda. Relation between the molecular orientations of a very thin liquid crystal layer and an underlying rubbed polyimide film. *Journal of Applied Physics*, 88(6):3235–3241, 2000.

[24] W Zheng. *Surface Wetting Characteristics of Rubbed Polyimide Thin Films, Polymer Thin Films*. Number 10.5772/8403. Abbass A Hashim (Ed.), 2010.

[25] J Stöhr, MG Samant, A Cossy-Favre, J Diaz, Y Momoi, S Odahara, and T Nagata. Microscopic origin of liquid crystal alignment on rubbed polymer surfaces. *Macromolecules*, 31(6):1942–1946, 1998.

[26] M O'Neill and SM Kelly. Photoinduced surface alignment for liquid crystal displays. *Journal of Physics D: Applied Physics*, 33(10):R67, 2000.

[27] M Monkade, M Boix, and G Durand. Order electricity and oblique nematic orientation on rough solid surfaces. *EPL (Europhysics Letters)*, 5(8):697, 1988.

[28] Lawrence Goodman, JT McGinn, Charles H Anderson, Frank Digeronimo, et al. Topography of obliquely evaporated silicon oxide films and its effect on liquid-crystal orientation. *Electron Devices, IEEE Transactions on*, 24(7):795–804, 1977.

[29] Zurab V Wardosanidze. *Holography Based on the Weigert's Effect*. INTECH Open Access Publisher, 2011.

[30] Lev M Blinov. *Structure and properties of liquid crystals*, volume 123. Springer Science & Business Media, 2010.

[31] J Prost. *The physics of liquid crystals*. Number 83. Oxford university press, 1995.

[32] CA Bailey, VP Tondiglia, LV Natarajan, MM Duning, RL Bricker, RL Sutherland, TJ White, MF Durstock, and TJ Bunning. Electromechanical tuning of cholesteric liquid crystals. *Journal of Applied Physics*, 107(1):013105, 2010.

[33] Ji Ma, Yannian Li, Timothy White, Augustine Urbas, and Quan Li. Light-driven nanoscale chiral molecular switch: reversible dynamic full range color phototuning. *Chemical Communications*, 46(20):3463–3465, 2010.

[34] Dwight W Berreman. Solid surface shape and the alignment of an adjacent nematic liquid crystal. *Physical review letters*, 28(26):1683, 1972.

[35] Dwight W Berreman. Alignment of liquid crystals by grooved surfaces. *Molecular Crystals and Liquid Crystals*, 23(3-4):215–231, 1973.

[36] Yan Jun Liu, Wei Wei Loh, Eunice Sok Ping Leong, Tanu Suryadi Kustandi, Xiao Wei Sun, and Jing Hua Teng. Nanoimprinted ultrafine line and space nanogratings for liquid crystal alignment. *Nanotechnology*, 23(46):465302, 2012.

[37] Stephen Y Chou, Peter R Krauss, and Preston J Renstrom. Nanoimprint lithography. *Journal of Vacuum Science & Technology B*, 14(6):4129–4133, 1996.

[38] Michael D Austin, Haixiong Ge, Wei Wu, Mingtao Li, Zhaoning Yu, D Wasserman, SA Lyon, and Stephen Y Chou. Fabrication of 5 nm linewidth and 14 nm pitch features by nanoimprint lithography. *Applied Physics Letters*, 84:5299, 2004.

[39] L Jay Guo. Nanoimprint lithography: methods and material requirements. *ADVANCED MATERIALS-DEERFIELD BEACH THEN WEINHEIM-*, 19(4):495, 2007.

[40] SY Yew, TS Kustandi, HY Low, JH Teng, YJ Liu, and Eunice SP Leong. Single-material-based multilayered nanostructures fabrication via reverse thermal nanoimprinting. *Microelectronic Engineering*, 88(9):2946–2950, 2011.

[41] Eunice Sok Ping Leong, Sok Yee Yew, Tanu Suryadi Kustandi, Yan Jun Liu, Hendrix Tanoto, Qing Yang Wu, Wei Wei Loh, Siew Lang Teo, and Jinghua Teng. New approach

for multilayered microstructures fabrication based on a water-soluble backing substrate. *ACS applied materials & interfaces*, 5(13):5898–5902, 2013.

[42] Eunice Sok Ping Leong, Siji Wu, Nan Zhang, Wei Wei Loh, Eng Huat Khoo, Guang Yuan Si, Hai Tao Dai, and Yan Jun Liu. Optical properties of ultrafine line and space polymeric nanogratings coated with metal and metal–dielectric–metal thin films. *Nanotechnology*, 25(5):055203, 2014.

[43] Luciano De Sio, Sameh Ferjani, Giuseppe Strangi, Cesare Umeton, and Roberto Bartolino. Soft periodic microstructures containing liquid crystals. *The Journal of Physical Chemistry B*, 117(4):1176–1185, 2013.

[44] Luciano De Sio, Sameh Ferjani, Giuseppe Strangi, Cesare Umeton, and Roberto Bartolino. Universal soft matter template for photonic applications. *Soft Matter*, 7(8):3739–3743, 2011.

[45] Luciano De Sio, Patrizia D'Aquila, Elvira Brunelli, Giuseppe Strangi, Dina Bellizzi, Giuseppe Passarino, Cesare Umeton, and Roberto Bartolino. Directed organization of dna filaments in a soft matter template. *Langmuir*, 29(10):3398–3403, 2013.

[46] Luciano De Sio, Nelson Tabiryan, and Timothy Bunning. Spontaneous radial liquid crystals alignment on curved polymeric surfaces. *Applied Physics Letters*, 104(22):221112, 2014.

[47] David C Wright and N David Mermin. Crystalline liquids: the blue phases. *Reviews of Modern physics*, 61(2):385, 1989.

[48] Jin Yan and Shin-Tson Wu. Polymer-stabilized blue phase liquid crystals: a tutorial [invited]. *Optical Materials Express*, 1(8):1527–1535, 2011.

[49] Hyunseok Choi, Hiroki Higuchi, and Hirotsugu Kikuchi. Fast electro-optic switching in liquid crystal blue phase ii. *Applied Physics Letters*, 98(13):131905, 2011.

[50] Jenny-Marie Wong, Jeoung-Yeon Hwang, and Liang-Chy Chien. Electrically reconfigurable and thermally sensitive optical properties of gold nanorods dispersed liquid crystal blue phase. *Soft Matter*, 7(18):7956–7959, 2011.

[51] Alastair Cunningham, Stefan Mühlig, Carsten Rockstuhl, and Thomas Bürgi. Coupling of plasmon resonances in tunable layered arrays of gold nanoparticles. *The Journal of Physical Chemistry C*, 115(18):8955–8960, 2011.

[52] Gero Decher. Fuzzy nanoassemblies: toward layered polymeric multicomposites. *science*, 277(5330):1232–1237, 1997.

[53] Pavel A Kossyrev, Aijun Yin, Sylvain G Cloutier, David A Cardimona, Danhong Huang, Paul M Alsing, and Jimmy M Xu. Electric field tuning of plasmonic response of nanodot array in liquid crystal matrix. *Nano letters*, 5(10):1978–1981, 2005.

[54] Eyal Feigenbaum, Kenneth Diest, and Harry A Atwater. Unity-order index change in transparent conducting oxides at visible frequencies. *Nano letters*, 10(6):2111–2116, 2010.

[55] Martina Abb, Pablo Albella, Javier Aizpurua, and Otto L Muskens. All-optical control of a single plasmonic nanoantenna–ito hybrid. *Nano letters*, 11(6):2457–2463, 2011.

[56] Yan Jun Liu, Qingzhen Hao, Joseph ST Smalley, Justin Liou, Iam Choon Khoo, and Tony Jun Huang. A frequency-addressed plasmonic switch based on dual-frequency liquid crystals. *Applied Physics Letters*, 97(9):091101, 2010.

[57] Catherine J Murphy, Tapan K Sau, Anand M Gole, Christopher J Orendorff, Jinxin Gao, Linfeng Gou, Simona E Hunyadi, and Tan Li. Anisotropic metal nanoparticles: synthesis, assembly, and optical applications. *The Journal of Physical Chemistry B*, 109(29):13857–13870, 2005.

[58] Limei Tian, Enze Chen, Naveen Gandra, Abdennour Abbas, and Srikanth Singamaneni. Gold nanorods as plasmonic nanotransducers: distance-dependent refractive index sensitivity. *Langmuir*, 28(50):17435–17442, 2012.

[59] Nikhil R Jana, Latha Gearheart, and Catherine J Murphy. Seed-mediated growth approach for shape-controlled synthesis of spheroidal and rod-like gold nanoparticles using a surfactant template. *Advanced Materials*, 13(18):1389, 2001.

[60] Richard Gans. Über die form ultramikroskopischer goldteilchen. *Ann. Phys*, 342(881), 1912.

[61] Luciano De Sio, Gérard Klein, Svetlana Serak, Nelson Tabiryan, Alastair Cunningham, Caterina Maria Tone, Federica Ciuchi, Thomas Bürgi, Cesare Umeton, and Timothy Bunning. All-optical control of localized plasmonic resonance realized by photoalignment of liquid crystals. *Journal of Materials Chemistry C*, 1(45):7483–7487, 2013.

[62] John Brian Pendry. Negative refraction makes a perfect lens. *Physical review letters*, 85 (18):3966, 2000.

[63] John B Pendry, David Schurig, and David R Smith. Controlling electromagnetic fields. *science*, 312(5781):1780–1782, 2006.

[64] Matthias Wuttig and Noboru Yamada. Phase-change materials for rewriteable data storage. *Nature materials*, 6(11):824–832, 2007.

[65] Brian Edwards, Andrea Alù, Michael E Young, Mário Silveirinha, and Nader Engheta. Experimental verification of epsilon-near-zero metamaterial coupling and energy squeezing using a microwave waveguide. *Physical Review Letters*, 100(3):033903, 2008.

[66] Stanley P Burgos, Rene de Waele, Albert Polman, and Harry A Atwater. A single-layer wide-angle negative-index metamaterial at visible frequencies. *Nature Materials*, 9(5): 407–412, 2010.

[67] Costas M Soukoulis and Martin Wegener. Optical metamaterials—more bulky and less lossy. *Science*, 330(6011):1633–1634, 2010.

[68] Luis M Liz-Marzán. Nanometals: formation and color. *Materials today*, 7(2):26–31, 2004.

[69] Qingkun Liu, Bohdan Senyuk, Jianwei Tang, Taewoo Lee, Jun Qian, Sailing He, and Ivan I Smalyukh. Plasmonic complex fluids of nematiclike and helicoidal self-assemblies of gold nanorods with a negative order parameter. *Physical review letters*, 109(8):088301, 2012.

[70] Qingkun Liu, Yanxia Cui, Dennis Gardner, Xin Li, Sailing He, and Ivan I Smalyukh. Self-alignment of plasmonic gold nanorods in reconfigurable anisotropic fluids for tunable bulk metamaterial applications. *Nano letters*, 10(4):1347–1353, 2010.

[71] Anton Kuzyk, Robert Schreiber, Zhiyuan Fan, Günther Pardatscher, Eva-Maria Roller, Alexander Högele, Friedrich C Simmel, Alexander O Govorov, and Tim Liedl. Dna-based self-assembly of chiral plasmonic nanostructures with tailored optical response. *Nature*, 483(7389):311–314, 2012.

[72] Aline Cerf, Thomas Alava, Robert A Barton, and Harold G Craighead. Transfer-printing of single dna molecule arrays on graphene for high-resolution electron imaging and analysis. *Nano letters*, 11(10):4232–4238, 2011.

[73] Baoquan Ding, Hao Wu, Wei Xu, Zhao Zhao, Yan Liu, Hongbin Yu, and Hao Yan. Interconnecting gold islands with dna origami nanotubes. *Nano letters*, 10(12):5065–5069, 2010.

[74] A Paul Alivisatos, Kai P Johnsson, Xiaogang Peng, Troy E Wilson, Colin J Loweth, Marcel P Bruchez, and Peter G Schultz. Organization of'nanocrystal molecules' using dna. 1996.

[75] Erik Winfree, Furong Liu, Lisa A Wenzler, and Nadrian C Seeman. Design and self-assembly of two-dimensional dna crystals. *Nature*, 394(6693):539–544, 1998.

[76] Luda S Shlyakhtenko, Vladimir N Potaman, Richard R Sinden, and Yuri L Lyubchenko. Structure and dynamics of supercoil-stabilized dna cruciforms. *Journal of molecular biology*, 280(1):61–72, 1998.

[77] Tiziana Placido, Roberto Comparelli, Francesco Giannici, P Davide Cozzoli, Giancarlo Capitani, Marinella Striccoli, Angela Agostiano, and M Lucia Curri. Photochemical synthesis of water-soluble gold nanorods: the role of silver in assisting anisotropic growth. *Chemistry of materials*, 21(18):4192–4202, 2009.

[78] Pei Yun Lee, John Costumbrado, Chih-Yuan Hsu, and Yong Hoon Kim. Agarose gel electrophoresis for the separation of dna fragments. *Journal of visualized experiments: JoVE*, (62):9400–9405, 2011.

[79] Michi Nakata, Giuliano Zanchetta, Brandon D Chapman, Christopher D Jones, Julie O Cross, Ronald Pindak, Tommaso Bellini, and Noel A Clark. End-to-end stacking and liquid crystal condensation of 6–to 20–base pair dna duplexes. *science*, 318(5854):1276–1279, 2007.

[80] DE Bradley. A study of the negative staining process. *Journal of general microbiology*, 29(3):503–516, 1962.

[81] Robert M Glaeser. Cryo-electron microscopy of biological nanostructures. *Physics today*, 61(1):48, 2008.

[82] Alison M Funston, Carolina Novo, Tim J Davis, and Paul Mulvaney. Plasmon coupling of gold nanorods at short distances and in different geometries. *Nano letters*, 9(4):1651–1658, 2009.

[83] Hassan ME Azzazy and Mai MH Mansour. In vitro diagnostic prospects of nanoparticles. *Clinica Chimica Acta*, 403(1):1–8, 2009.

[84] Ryan Huschka, Jorge Zuloaga, Mark W Knight, Lisa V Brown, Peter Nordlander, and Naomi J Halas. Light-induced release of dna from gold nanoparticles: nanoshells and nanorods. *Journal of the American Chemical Society*, 133(31):12247–12255, 2011.

[85] Eliza Hutter and Janos H Fendler. Exploitation of localized surface plasmon resonance. *Advanced Materials*, 16(19):1685–1706, 2004.

[86] Matthew Pelton, Javier Aizpurua, and Garnett Bryant. Metal-nanoparticle plasmonics. *Laser & Photonics Reviews*, 2(3):136–159, 2008.

[87] Dmitri K Gramotnev and Sergey I Bozhevolnyi. Plasmonics beyond the diffraction limit. *Nature photonics*, 4(2):83–91, 2010.

[88] Bergin Gjonaj, Jochen Aulbach, Patrick M Johnson, Allard P Mosk, L Kuipers, and Ad Lagendijk. Active spatial control of plasmonic fields. *Nature Photonics*, 5(6):360–363, 2011.

[89] Yeshaiahu Fainman, Kevin Tetz, Rostislav Rokitski, and Lin Pang. Surface plasmonic fields in nanophotonics. *Optics and photonics news*, 17(7):24–29, 2006.

[90] Martti Kauranen and Anatoly V Zayats. Nonlinear plasmonics. *Nature Photonics*, 6(11): 737–748, 2012.

[91] Bruno Palpant. Photothermal properties of gold nanoparticles. *Gold nanoparticles in physics, chemistry and biology. Imperial College Press, London*, 2012.

[92] Stefan A Maier and Harry A Atwater. Plasmonics: Localization and guiding of electromagnetic energy in metal/dielectric structures. *Journal of Applied Physics*, 98(1):011101, 2005.

[93] Somsubhra Maity, Lori N Downen, Jason R Bochinski, and Laura I Clarke. Embedded metal nanoparticles as localized heat sources: An alternative processing approach for complex polymeric materials. *Polymer*, 52(7):1674–1685, 2011.

[94] Guillaume Baffou, Christian Girard, and Romain Quidant. Mapping heat origin in plasmonic structures. *Physical review letters*, 104(13):136805, 2010.

[95] Guillaume Baffou, Romain Quidant, and F Javier Garci?a de Abajo. Nanoscale control of optical heating in complex plasmonic systems. *ACS nano*, 4(2):709–716, 2010.

[96] J Kimling, M Maier, B Okenve, V Kotaidis, H Ballot, and A Plech. Turkevich method for gold nanoparticle synthesis revisited. *The Journal of Physical Chemistry B*, 110(32): 15700–15707, 2006.

[97] Traci R Jensen, Michelle L Duval, K Lance Kelly, Anne A Lazarides, George C Schatz, and Richard P Van Duyne. Nanosphere lithography: effect of the external dielectric medium on the surface plasmon resonance spectrum of a periodic array of silver nanoparticles. *The Journal of Physical Chemistry B*, 103(45):9846–9853, 1999.

[98] Yugang Sun and Younan Xia. Increased sensitivity of surface plasmon resonance of gold nanoshells compared to that of gold solid colloids in response to environmental changes. *Analytical Chemistry*, 74(20):5297–5305, 2002.

[99] Hugh H Richardson, Michael T Carlson, Peter J Tandler, Pedro Hernandez, and Alexander O Govorov. Experimental and theoretical studies of light-to-heat conversion and collective heating effects in metal nanoparticle solutions. *Nano letters*, 9(3):1139–1146, 2009.

[100] Luigia Pezzi, Luciano De Sio, Alessandro Veltri, Tiziana Placido, Giovanna Palermo, Roberto Comparelli, Maria Lucia Curri, Angela Agostiano, Nelson Tabirian, and Cesare Umeton. Photo-thermal effects in gold nanoparticles dispersed in thermotropic nematic liquid crystals. *Physical Chemistry Chemical Physics*, 2015.

[101] Guillaume Baffou, Pascal Berto, Esteban Bermu?dez Uren?a, Romain Quidant, Serge Monneret, Julien Polleux, and Hervé Rigneault. Photoinduced heating of nanoparticle arrays. *Acs Nano*, 7(8):6478–6488, 2013.

[102] G. Baffou and R. Quidant. Thermo-plasmonics: using metallic nanostructures as nano-sources of heat. *Laser & Photonics Reviews*, 7(2):171–187, 2013.

[103] H. S. Carslaw and J. C. Jaeger. *Conduction of heat in solids*. Clarendon Press, 1959. URL http://books.google.it/books?id=ySRRAAAAMAAJ.

[104] Edward Harrison. *Darkness at night: A riddle of the universe*. Harvard University Press, 1989.

[105] Guillaume Baffou, Esteban Bermuudez Urenna, Pascal Berto, Serge Monneret, Romain Quidant, and Hervé Rigneault. Deterministic temperature shaping using plasmonic nanoparticle assemblies. *Nanoscale*, 6(15):8984–8989, 2014.

[106] Prashant K Jain and Mostafa A El-Sayed. Plasmonic coupling in noble metal nanostructures. *Chemical Physics Letters*, 487(4):153–164, 2010.

[107] K-H Su, Q-H Wei, X Zhang, JJ Mock, David R Smith, and S Schultz. Interparticle coupling effects on plasmon resonances of nanogold particles. *Nano Letters*, 3(8):1087–1090, 2003.

[108] Y. Sun, S. K Gray, and S. Peng. Surface chemistry: a non-negligible parameter in determining optical properties of small colloidal metal nanoparticles. *Physical Chemistry Chemical Physics*, 13(25):11814–11826, 2011.

[109] H. S. Carslaw and J. C. Jaeger. *Conduction of heat in solids*. Clarendon Press, 1959. URL http://books.google.it/books?id=ySRRAAAAMAAJ.

[110] C Umeton, A Sgrò, and F Simoni. Optically induced phase shift in nematic liquid crystals with hybrid alignment. *JOSA B*, 4(12):1938–1942, 1987.

[111] Alexander O Govorov and Hugh H Richardson. Generating heat with metal nanoparticles. *Nano Today*, 2(1):30–38, 2007.

[112] Roberto Caputo, Alessandro Veltri, Cesare Umeton, and Andrey V Sukhov. Kogelnik-like model for the diffraction efficiency of POLICRYPS gratings. *JOSA B*, 22(4):735–742, 2005.

[113] Jun Li, Sebastian Gauza, and Shin-Tson Wu. Temperature effect on liquid crystal refractive indices. *Journal of applied physics*, 96(1):19–24, 2004.

[114] Jun Li and Shin-Tson Wu. Extended cauchy equations for the refractive indices of liquid crystals. *Journal of applied physics*, 95(3):896–901, 2004.

[115] Jun Li and Shin-Tson Wu. Two-coefficient cauchy model for low birefringence liquid crystals. *Journal of applied physics*, 96(1):170–174, 2004.

[116] Jun Li, Chien-Hui Wen, Sebastian Gauza, Ruibo Lu, and Shin-Tson Wu. Refractive indices of liquid crystals for display applications. *Display Technology, Journal of*, 1(1): 51–61, 2005.

[117] Guenter Ahlers, David S Cannell, Lars Inge Berge, and Shinichi Sakurai. Thermal conductivity of the nematic liquid crystal 4-n-pentyl-4'-cyanobiphenyl. *Physical Review E*, 49(1):545, 1994.

[118] Pochi Yeh. Extended jones matrix method. *JOSA*, 72(4):507–513, 1982.

[119] NV Tabiryan, AV Sukhov, and B Ya Zel'Dovich. Orientational optical nonlinearity of liquid crystals. *Molecular Crystals and Liquid Crystals*, 136(1):1–139, 1986.

[120] M Warenghem, JF Blach, and JF Henninot. Thermo-nematicon: an unnatural coexistence of solitons in liquid crystals? *JOSA B*, 25(11):1882–1887, 2008.

[121] L. De Sio, editor. *Active Plasmonic Nanomaterials*. Pan Stanford, 2015. ISBN 9789814613002.

[122] Susie Eustis and Mostafa A El-Sayed. Why gold nanoparticles are more precious than pretty gold: noble metal surface plasmon resonance and its enhancement of the radiative and nonradiative properties of nanocrystals of different shapes. *Chemical Society Reviews*, 35(3):209–217, 2006.

[123] Emmanuel Stratakis and Emmanuel Kymakis. Nanoparticle-based plasmonic organic photovoltaic devices. *Materials Today*, 16(4):133–146, 2013.

[124] Luciano De Sio, Tiziana Placido, Svetlana Serak, Roberto Comparelli, Michela Tamborra, Nelson Tabiryan, M Lucia Curri, Roberto Bartolino, Cesare Umeton, and Timothy Bunning. Nano-localized heating source for photonics and plasmonics. *Advanced Optical Materials*, 1(12):899–904, 2013.

[125] Constantin Ungureanu, Rene Kroes, Wilma Petersen, Tom AM Groothuis, Felicia Ungureanu, Hans Janssen, Fijs WB van Leeuwen, Rob PH Kooyman, Srirang Manohar, and Ton G van Leeuwen. Light interactions with gold nanorods and cells: implications for photothermal nanotherapeutics. *Nano letters*, 11(5):1887–1894, 2011.

[126] Nikhil R Jana. Gram-scale synthesis of soluble, near-monodisperse gold nanorods and other anisotropic nanoparticles. *Small*, 1(8-9):875–882, 2005.

[127] Heino Finkelmann, Sung Tae Kim, A Munoz, Peter Palffy-Muhoray, and Bahman Taheri. Tunable mirrorless lasing in cholesteric liquid crystalline elastomers. *Advanced Materials*, 13(14):1069–1072, 2001.

[128] Xiaohua Huang and Mostafa A El-Sayed. Plasmonic photo-thermal therapy (pptt). *Alexandria Journal of Medicine*, 47(1):1–9, 2011.

[129] André M Gobin, Min Ho Lee, Naomi J Halas, William D James, Rebekah A Drezek, and Jennifer L West. Near-infrared resonant nanoshells for combined optical imaging and photothermal cancer therapy. *Nano letters*, 7(7):1929–1934, 2007.

[130] Erik C Dreaden, Alaaldin M Alkilany, Xiaohua Huang, Catherine J Murphy, and Mostafa A El-Sayed. The golden age: gold nanoparticles for biomedicine. *Chemical Society Reviews*, 41(7):2740–2779, 2012.

[131] Min Hu, Jingyi Chen, Zhi-Yuan Li, Leslie Au, Gregory V Hartland, Xingde Li, Manuel Marquez, and Younan Xia. Gold nanostructures: engineering their plasmonic properties for biomedical applications. *Chemical Society Reviews*, 35(11):1084–1094, 2006.

[132] Ser-Sing Chang, Chao-Wen Shih, Cheng-Dah Chen, Wei-Cheng Lai, and CR Chris Wang. The shape transition of gold nanorods. *Langmuir*, 15(3):701–709, 1999.

[133] Catherine J Murphy and Nikhil R Jana. Controlling the aspect ratio of inorganic nanorods and nanowires. *Advanced Materials*, 14(1):80, 2002.

[134] Babak Nikoobakht and Mostafa A El-Sayed. Preparation and growth mechanism of gold nanorods (nrs) using seed-mediated growth method. *Chemistry of Materials*, 15(10): 1957–1962, 2003.

[135] Stephan Link, MB Mohamed, and MA El-Sayed. Simulation of the optical absorption spectra of gold nanorods as a function of their aspect ratio and the effect of the medium dielectric constant. *The Journal of Physical Chemistry B*, 103(16):3073–3077, 1999.

[136] E Prodan, C Radloff, Naomi J Halas, and P Nordlander. A hybridization model for the plasmon response of complex nanostructures. *Science*, 302(5644):419–422, 2003.

[137] Prashant K Jain, Wenyu Huang, and Mostafa A El-Sayed. On the universal scaling behavior of the distance decay of plasmon coupling in metal nanoparticle pairs: a plasmon ruler equation. *Nano Letters*, 7(7):2080–2088, 2007.

[138] Yugang Sun, Brian T Mayers, and Younan Xia. Template-engaged replacement reaction: a one-step approach to the large-scale synthesis of metal nanostructures with hollow interiors. *Nano Letters*, 2(5):481–485, 2002.

[139] Raheleh Rahbari, Tom Sheahan, Vasileios Modes, Pam Collier, Catriona Macfarlane, and Richard M Badge. A novel l1 retrotransposon marker for hela cell line identification. *Biotechniques*, 46(4):277, 2009.

[140] William F Scherer, Jerome T Syverton, and George O Gey. Studies on the propagation in vitro of poliomyelitis viruses iv. viral multiplication in a stable strain of human malignant epithelial cells (strain hela) derived from an epidermoid carcinoma of the cervix. *The Journal of experimental medicine*, 97(5):695–710, 1953.